ON THE DIRECT MEASUREMENT OF INCLUSIONS IN MOLTEN METALS

by

Selçuk KUYUCAK

Department of Mining and Metallurgical Engineering
McGill University
Montreal, Quebec
Canada

A thesis submitted to the Faculty of Graduate Studies and Research
in partial fulfillment of the requirements for
the degree of Doctor of Philosophy

ABSTRACT

A method of inclusion measurement in molten metals, known as the Liquid Metal Cleanness Analysis or LiMCA, currently in use for aluminum, has been developed for high temperature and reactive industrial metals.

LiMCA probe consists of an electrically insulating sampling tube with two electrodes, in- and outside the tube. The sampling tube also incorporates a small orifice through which molten metal is aspirated. As suspended inclusions pass through the orifice, and in the presence of an electric current, voltage pulses are generated. By measuring and counting such pulses electronically, the size distribution of inclusions can be obtained. The orifice, therefore, serves as an Electric Sensing Zone (ESZ) for the probe

This work presents an analysis of LiMCA's electric circuitry, and the design and operation of LiMCA probes in steels, copper and magnesium alloys.

RÉSUMÉ

Une méthode de mesure des particules en suspension dans les métaux liquides est connue sous le nom de LiMCA (Liquid Metal Cleanness Analysis). Cette méthode, déjà couramment utilisée pour l'aluminium, a été développé pour les métaux industriels réactifs et ceux à haute température.

La sonde LiMCA consiste en un tube d'échantillonnage et de deux électrodes, une à l'intérieur du tube, la seconde à l'extérieur. Le tube comporte également un minuscule orifice à travers lequel le métal est aspiré Lorsque, en présence d'un courant électrique, les particules passent à travers l'orifice, un pulse de voltage est généré. La mesure et le comptage électronique de tels pulses permettent d'obtenir une distribution des tailles des particules. L'orifice agit alors comme une zone électrique sensible (Electric Sensing Zone, ESZ) pour la sonde.

Cet ouvrage présente une analyse des circuits électriques, du design, ainsi que de l'opération de la sonde LiMCA dans des alliages d'acier, de cuivre et de magnésium.

ACKNOWLEDGEMENTS

This work was supervised by Prof R.I L Guthrie His continued optimism created a pleasent working environment and moral support His prowess to establish timely contacts with boron - silicon steel, copper - beryllium alloy and magnesium manufacturers was instrumental in bringing this work to a worthwhile conclusion I also would like to thank him for granting me the intellectual and financial freedom to carry out my own decisions.

I would like to thank our technicians at the machine shop, Martin, Bruno, and Raymond, for building our instrument, and putting many pieces together with great skill and patience, our "magician technician" Frank Sebo, among many other things, putting an orifice into quartz the first time (deemed impossible by the glass blower), and Mrs. G. Chen, our visiting scientist, for doing much of the metallography

I also would like to thank the following people, institutions, and corporations for their contribution:

The first steel that yielded to LiMCA, the boron - silicon transformer steel, belonged to MetGlass Products of Allied Corp , Parsippanny, N J

Contact angles from sessile drop profiles were calculated using a computer program developed at the University of Toronto, with the permission of Prof A W Neumann, Dept. of Mechanical Engineering, and the valuable assistance of Mr S W Ip, Dept. of Metallurgy and Materials Science.

Experiments with copper - beryllium alloys were performed at Brush Wellman Inc , Elmore, Ohio, with the assistance of Mr. R.L. Ashbrooke and Dr S Ali, who also furnished the metallographic cleanness assessments for our samples

Experiments in magnesium alloys were carried out in cooperation with Haley Industries Ltd. of Ontario, through Mr. B. Keith, who also provided us with the mechanical testing of gravity cast test bars, and chemical analysis. Corrosion testing of magnesium alloys were made at Dow Chemical Co., Lake Jackson Research Center, Freeport, Texas, through the kind assistance of Mr. J.E. Hillis.

Financial assistance for the research was mostly provided by the Natural Science and Engineering Research Council of Canada and BHP Inc., Australia

CONTENTS

PART 3: APPLICATION OF LiMCA TO MOLTEN COPPER AND ITS ALLOYS

PART 4: APPLICATION OF LiMCA TO MOLTEN MAGNESIUM AND ITS ALLOYS

PART 5: CONCLUSIONS TO THE THESIS

LIST OF SYMBOLS

a_i	chemical activity of i w.r t. pure component standard state
C_p	heat capacity, J kg^{-1}
C_D	discharge coefficient
d	particle diameter, m, mm, µm
D	orifice diameter, m, µm
E	electromotiv force, Volts
f_i	henrian activity coefficient of component i
g_i	molar free energy of component i, J mol^{-1}
g^E	excess free energy of mixing, J mol^{-1}
ΔG°_i	standard free energy change of reaction i, J mol^{-1}
h	heat transfer coefficient, W m^{-2} °C^{-1}
h_i	chemical activity of i w r t. 1 wt % standard state on Henry's law line
h_i	molar enthalpy of component i, J mol^{-1}
i	electric current density, A m^{-2}
I	electric current, Amperes
k	thermal conductivity, W m^{-1} °C^{-1}
K_i	equilibrium constant for chemical reaction i
N_d	number of particles greater than size d, kg^{-1}, g^{-1}, mm^{-3}
N_{A_i}	number of particles per unit area in size class i, mm^{-2}
N_{V_i}	number of particles per unit volume in size class i, kg^{-1}, g^{-1}, mm^{-3}
R	electric resistance, Ω
R	radius, radius of curvature, m
ΔR	transient change in electric resistance, Ω
R	universal gas constant, 8 314 3 J °K^{-1} mol^{-1}
M	molecular weight
T	absolute temperature, °K
u	fluid velocity, m s^{-1}
v_i	molar volume of component i, m^3 mol^{-1}
v^E	excess molar volume of mixing, m^3 mol^{-1}
V	electric potential difference, Volts
ΔV	transient change in electric potential, Volts, µV
V_f	volume fraction of a component phase
W_f	weight fraction of a component phase
x_i	mole fraction of i
γ	surface or interfacial tension, J m^{-2}
γ_i	activity coefficient of i w.r.t. pure component standard state
ρ	density, kg m^{-3}
ρ, ρ_e	electric resistivity, Ω m
θ	dimensionless temperature
$[Bi]$	Biot number
$[Fo]$	Fourier number
$[Re]$	Reynolds number

PART 1: INTRODUCTION AND BACKGROUND

1. INTRODUCTION: INCLUSIONS IN METALS

1.1 Definition of Inclusion and their Presence in Metals

An inclusion in a metal may be defined as a second phase particle that has detrimental effect on metal properties Since, very often, oxide particles originating from deoxidation products or refractory erosion are detrimental to mechanical properties, the use of the term "inclusion" has become synonymous with the presence of these particles Indeed, those definitions for "inclusion" found by the author in technical dictionaries and relevant literature, follow similar concepts

> A particle of alien material retained in a solid metal Such inclusions are generally oxides, sulfides or silicates of one or the other of the component metals of the alloy, but may also be particles of refractory materials picked up from the furnaces or ladle lining. [1]
>
> An impure particle, such as sand, trapped in molten metal during solidification [2]
>
> Non-metallic impurities in a metal In wrought materials the inclusions become elongated during hot working and provide permanent evidence of its extent. [3]
>
> Particles of foreign material in a metallic matrix. The particles are usually compounds, such as oxides, sulfides or silicates, but may be any substance foreign and essentially insoluble in the matrix [4]
>
> As normally produced, steel contains considerable quantities of second phase particles which are generally referred to as inclusions While second phase particles are formed by intermetallic compounds, it is generally non-metallic particles which are intended when inclusions are mentioned [5]

The ambiguity in the above definitions leads to a dichotomy of views Current research efforts, for instance, try to produce metal matrix composites in which alumina powder is intermixed with aluminum or magnesium metal, for example, in order to enhance these metals' properties in certain applications [6, 7] In 1966, a whole conference was dedicated to oxide dispersion strengthening of metals [8]

These alloys, when compared with the base metal, would have inferior mechanical properties at ordinary temperatures, but can display a superior strength, and lower creep, at elevated temperatures This can make them useful candidates for selection in certain applications such as in the manufacture of turbine blades Evidently, it is not justifiable to classify oxide particles as inclusions in every context Similarly, metallic particles or intermetallic compounds of iron, copper and nickel, in magnesium dramatically increase its corrosion rate [9], while hard intermetallic particles such as titanium diborides in aluminum can cause failures in the production of beverage cans [10], and hence these may be considered as inclusions

Inclusions, or their component elements, enter metals during their processing. Oxygen and sulfur, for instance, dissolve in molten iron and copper alloys, and if not removed, will form oxides and sulfides with the base metal, as the metal solidifies. Deoxidation and desulfurization practices attempt to remove $\underline{S}$ and $\underline{O}$ by lowering their solubility in the molten metal This is achieved by mixing more reactive elements into the melts to form deoxidation and desulfurization products, and by physically separating these second phase particles from the molten metal Similarly, iron is removed from magnesium by treating the melt with $MnCl_2$, to form FeMn intermetallics, which are then separated from the melt by gravity settling or filtration [11] Table 1 highlights the presence of second phase particles in metals according to their sources. Designing completely inclusion- free processes for metals would be expensive if not impossible, and from a cost-benefit point, would not be desirable Instead, efforts have been concentrated in controlling inclusion numbers, size, shape and chemistry, to minimize their deleterious effects for a given application, with a minimum cost [12]

1.2 Detrimental Effects of Inclusions

Problems originating from inclusions arise because of failures during metal fabrication or failures during service, Fig 1. This topic is highly researched and documented for steels, as references can be made to a number of review articles [13-17], and to some degree for aluminum [18-20], copper [21, 22] and magnesium [23, 24] alloys

Low melting point (m.p) inclusions in a higher melting point metal, such as sulfides in steels, can lead to break-outs during the solidification process in a

Table 1. Classification of second phase particles according to their sources

Primary Particles:	form in liquid metals They are termed indigeneous if they nucleate and grow in situ, as a result of alloying with reactive elements to remove impurities, by forming insoluble compounds Exogeneous particles enter from outside sources, and may originate from refractory erosion, slag, oxide film or flux entrainment. Very often primary particles are inclusions, and their removal can be affected by physical separation, using gravity settling, flotation, stirring or filtration. Direct measurement of their amounts to monitor their level is the basis of this thesis.
Secondary Particles:	precipitate from supersaturated liquid during solidification as a result of solute enrichment. When inclusions form in this way, it is too late to manage their separation from the metal.
Tertiary Particles:	precipitate from supersaturated solid solution during cooling. These particles are intermetallic in character, and their precipitation is usually controlled by thermomechanical treatment or heat treatment, to improve mechanical properties.

continuous casting machine, and similarly, to hot shortness during thermo-mechanical treatment [25] Any large inclusions near the surface of continuously cast steel billets can cause streaks; therefore, it is common for slabs, blooms, and billets to be cooled, inspected, cleaned (scarfed), and then reheated, prior to thermo-mechanical processing. Elimination of surface defects in steel processing is one major goal towards achieving direct rolling, i.e. utilizing the sensible heat of the continuously cast billets [26-27].

Hard, non-deformable inclusions, such as oxides in steels and TiB_2's in aluminum, can cause failures in the form of breakages and tear-offs in the manufacture of thin gauge products. Examples of this would be steel cord wires for automobile tires, drawn to 0.15-0 20 mm fine cord [28], and drawn and ironed beverage cans that can be as thin as 0.05 mm for aluminum and 0.1 mm for steels in their middle section [29-30]. In general, a reduction in hot and room temperature ductility will make most forming operations difficult. New methods have been developed to study and quantify the damage caused by the presence of inclusions via void formation and coalescence that lead to a reduction in ductility and toughness [31]

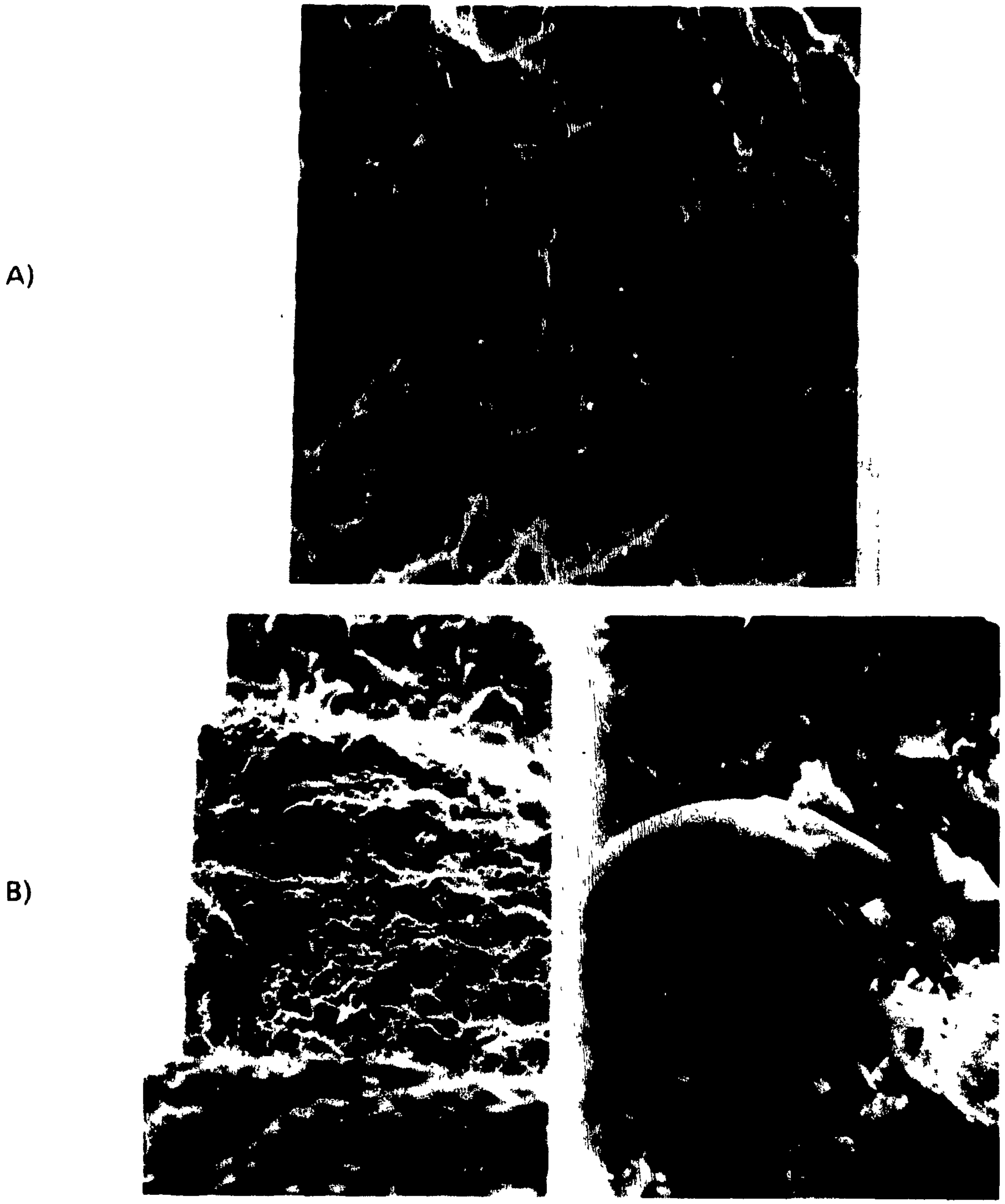

Fig. 1: Detrimental effects of inclusions. (A) Loss in ductility caused by void formation and coalescence. This is the major cause of filure in plastic forming operations. (B) Reduction in fatigue strength aided by crack nucleation at a preferred site. On the left micrograph, 3 fatigue cracks, separated by two ratchet markings, propagate in 3 different planes, and at the root of each crack an inclusion was found. From [89].

The most noted effect of inclusions on metals in service is a reduction in the fatigue strength, since inclusions can act as crack nucleation sites Again, this is well documented for steels [32-34], and important in all metal / alloy systems selected for structural applications and subject to cyclic loads, such as springs, bearings, and parts used in mechanical energy transmission.

Other effects of inclusions include an increase in ductile to brittle transition temperatures in steels and a reduction in the ductile impact shelf energy in the transverse direction. These properties are important in pipeline grade steels, and degradation is generally caused by sulfide inclusions [35] Impaired surface quality resulting from the presence of inclusions promotes corrosion in low carbon steel sheets for car bodies and pitting corrosion in stainless steel sheets [36] Also, as mentioned before, more noble metallic particles containing iron, nickel, and copper cause high rates of corrosion in magnesium alloys by setting up galvanic microcells.

Attempts have been made to quantify the effects of inclusions in terms of their size, number density and chemistry [12]. Inclusion chemistry is process dependent and expected inclusion chemistries are usually fixed for a given process In some instances, inclusion chemistry can be controlled with a fair degree of success by making changes in the metal's processing, as has been demonstrated with improved morphology of sulfides by manganese additions, and changing the morphology of alumina inclusions by calcium silicide injection, in steels Inclusion size and number density, however, depends on the efficiency of physical separation of inclusions and has been shown to be highly unpredictable [37]. To make matters worse, physical properties such as ductility for ease of fabrication, surface quality and fatigue strength are highly dependent on the number of inclusions greater than a critical size, and usually, the larger the inclusions, the worse are the effects. Using a statistical approach, for instance, a model has been developed by Nordberg, to predict the fatigue strength of steels from their inclusion size distribution curves [38]. In another study, an inclusion size distribution curve was used to predict the susceptibility of steel billets to surface defects during hot working operations [39] Analytical methods and empirical data are becoming increasingly available to quantify the effect of a metal's inclusion content on its properties.

Because of the variability in the number density and size of inclusions, and their strong and quantifiable effect on the properties, it is becoming more and more important to monitor inclusion levels in metals. In the next chapter, methods of inclusion measurement are classified and briefly outlined according to their capabilities and principles, and in the following chapter, a method of inclusion measurement in molten metals, based on electric sensing zone (E.S.Z.) principle is described The application of this method to high temperature and reactive metals, namely iron, copper and magnesium melts, forms the basis of this thesis

2. MEASUREMENT OF INCLUSION CONTENT IN METALS

Usually, inclusion measuring methods will either give a result that is indicative of the total volume, or weight fraction, of inclusions, or yield data related to their frequency distribution. The former methods may be termed global, since a global value is obtained on the amount, but not on the size of inclusions. The latter methods are termed sensing zone methods, as inclusions are counted individually, as a metal sample is scanned for their presence. The smallest volume or area that is examined during each scan constitutes the sensing zone, and the size of the sensing zone determines the threshold size of detection and the coincidence in counting. In the following, methods of inclusion evaluation are discussed in terms of their physical principles and capabilities.

2.1 Global Methods

2.1.1 Chemical analysis

As the solid solubility of oxygen and sulfur are negligible in most metals and alloys, chemical analysis for oxygen and sulfur give the first indication of the oxide and sulfide inclusion contents. For accurate oxygen determinations, an approximately 1 g solid sample is fused in a graphite crucible and is heated up to a high enough temperature (2200 °C), until complete reduction of all combined oxygen to carbon monoxide is affected through contact with the graphite crucible. For sulfur, the sample is fused in an alumina crucible and the combined sulfur combusted to sulfur dioxide under an oxidizing atmosphere. The gaseous products are then analyzed for the presence of CO or SO_2, as appropriate Spectral methods, although less accurate, can analyze for sulfur, and high energy spectral methods, such as Auger emission, have also become available for oxygen [40]

Corrosion in magnesium alloys is highly susceptible to the presence of metallic inclusions containing iron, nickel and copper, and their amounts are analysed by spectral means. Although chemical analyses yield the weight fraction of component impurity elements, it is the volume fraction of inclusions that is of fundamental interest. This can be calculated if the associated inclusion chemistry is known, according to:

$$V_{f,inc} = \frac{\rho_{metal}}{\rho_{inclusion}} \cdot \frac{M_{inclusion}}{M_{imp.\,element}} \cdot W_{f,\,imp.\,element} \qquad (1)$$

where V_f and W_f are the volume and weight fractions, ρ is the density, M is the molecular weight.

Table 2. Volume fraction of inclusions vs. weight fraction of the associated impurity element, from Eqn. (1)

Impurity element analysed	Associated Inclusion			V_f / W_f in			
	Chemical Formula	M. W.	Density kg/m3 (a)	Fe 7870(b)	Cu 8960	Al 2700	Mg 1740
O	Al_2O_3	102	3900	4.3	4.9	1.5	
	SiO_2	60	2800	5.3	6.0		
	B_2O_3	70	1840	6.2			
	$MnSiO_3$	131	3500	6.1			
	Mn_2SiO_4	202	3500	7.1			
	$Al_2O_3.SiO_2$	162	3247	4.9			
	$(Al_2O_3)_3.(SiO_2)_2$(c)	426	3156	5.1			
	Cu_2O	143	6000		13.3		
	BeO	25	3020		4.6		
	MgO	40	3700				1.2
S	MnS	87	4000	5.3			
	MnS_2	119	3460	4.2			
	Cu_2S	159	6760		6.6		
Cl	NaCl	58	2170			2.1	1.3

(a) density values are from [41, 42]
(b) values under each metal are their room temperature densities
(c) mullite

Table 2 shows the ratios of the weight fraction of impurity elements to the volume fraction of associated inclusions. Surprisingly for iron, for different inclusion chemistries, this ratio does not fluctuate widely, and a factor of 5 will approximately give the volume fraction of inclusions from a given weight fraction of oxygen or sulfur. However, differences do exist, as for a given oxygen content, Mn_2SiO_4 inclusions in steels, for example, will occupy a proportionately larger volume than alumina inclusions. This difference is particularly pronounced in copper, between Cu_2O versus BeO inclusions. The table also indicates that the same level of oxygen, contained for instance as alumina inclusions, will not mean the same inclusion content in different metals. Therefore, in addition to the uncertainty about inclusion sizes, the actual inclusion content is also open to some interpretation using chemical methods

Similarly, it will be appreciated that any contaminating surface oxide films associated with sample preparation procedures can have a profound influence in the measurement of oxides at the ppm levels.

2.1.2 Microscopy

For the assessment of steel cleanness levels, methods of optical microscopy based on comparison with standard charts, such as the Fox and the Jernkontoret (J K.) counts may be considered as global, since they yield a single index. As these methods are weighted towards larger inclusions, an indication of the latters' frequency can also be obtained [43]. However, the results of these comparison methods are operator dependent, and this has been shown to have a large effect on the accuracy (repeatability) of the results [44]

It has been shown in quantitative metallography that volume fraction, area fraction, line fraction or point fraction of a randomly distributed phase are equivalent and therefore, the best estimates of each other [45] Among these, the point fraction has been found to be particularly useful in determining the inclusion content of a metal, because of its relative ease in counting, and its high reproducibility between different operators [46].

2.1.3 Transmission Attenuation Measurements of Ultrasonic Signals

Considerable research time has been invested in attempting to apply this technique to measure inclusion contents in aluminum, steel and copper melts In principle, inclusions in metallic melts scatter acoustic waves; therefore, the amount of sonic attenuation measured is a function of the inclusion content or their number density. To overcome the temperature problems in molten metals, wave guide extensions have been used to deliver and detect the ultrasound signals The minimum size of inclusion that will cause scattering depends on the wavelength of sound in the melt Presently, because of a rapid increase in signal attenuation by the metal waveguides, signal frequencies cannot be increased to more than about 10 MHz, and for a sound velocity of 4700 m/s in molten aluminum, this corresponds to a minimum wavelength of approximately 500 µm. It is generally recognized that particles greater than about 10% of the signal wavelength will start to cause attenuation [47], however, recently this figure has been debated and it is claimed that particles as small as 3% of the wavelength, too, will contribute to sonic attenuation [48] One practical problem with instruments of this kind is the necessity to measure small differences between large quantities. A great deal of attenuation already takes place at the guide rods and within the pure melt itself, inclusions contributing to only a small fraction of the total It has been possible to demonstrate, for instance, changes in sound attenuation as a melt becomes more contaminated with inclusions However, it has not been possible to assign a cleanness value for a given melt, from a single measurement. If calibration problems can be overcome, the method may yet prove to be useful to assess the total content of oxide inclusions.

2.1.4 Other Global Methods

A method based on Electron Beam (E.B.) remelting of button samples has been developed for special alloys [49]. In this method, samples weighing approximately 600 g are remelted in an E.B. furnace so as to produce a button shape, and inclusions, with the aid of gravity and surface tension, are allowed to amalgamate as a raft on top of the molten button By measuring the dimensions of the raft, the volume fraction of inclusions can be determined directly [50]. Since a complete physical separation is not expected, the results would be selective with respect to inclusion size and shape. The method is particularly suitable for clean alloys (containing, for example, less than 100 ppm volume fraction of inclusions) where, without this preconcentration step, it would not be possible to observe a significant number of inclusions within a reasonable area by standard microscopic techniques

Similarly for aluminum, a preconcentration step for inclusions is necessary before a metallographic technique can be applied. To this end, Alcan, for instance, has developed the Porous Disc Filtration Apparatus (PoDFA), a technique which consists of forcing a measured mass of aluminum sample (2.25 kg) through a porous filter disc under pressure [51]. The pressure is relieved while some metal still remains upon the filter. This overlaying metal is allowed to solidify and the filter cake recovered and examined metallographically. The result is usually expressed as the area of inclusions within a central vertical plane of the filter cake (disc), in mm^2 per kg of metal sampled.

2.2 Sensing Zone Methods

These methods depend on identifying and counting of individual inclusions, and can ultimately yield an inclusion size distribution. Sometimes a global and a sensing zone technique can both be employed to derive information from a given method, as the concentrated inclusions in the filter cake of PoDFA and the raft of E B remelting, are usually examined for the individual larger inclusions under a microscope.

2.2.1 Macroscopic and Microscopic Techniques

Macroscopic techniques attempt to reveal particularly large inclusions. Surfaces are examined visually, and the detectable inclusion size is determined by the resolution power of the human eye, which may be taken as 0.4 mm Usually, the frequency of inclusions in different size intervals are recorded in order to obtain a total severity value, this being the weighted sum of frequency results, wherein larger inclusions have more weight. For most metals such as steels, copper, aluminum, and magnesium, it is also common practice to examine the fresh fracture surfaces, where inclusions would be concentrated. Another way to increase sample size is a step down method, where the sample surface is successively machined in a stepwise fashion, and examined for the presence of macro-inclusions The macro-techniques have been standardized for most structural metals by the American Society for Testing and Materials [52].

Steel tinplate products are particularly inclusion sensitive and for such thin steel sheets, magnetic particle inspection has been developed during the past ten years to rapidly identify inclusions greater than 50 µm [53, 54]. In this method, the steel sheet is magnetized parallel to its surface. When the magnetic lines of force are disrupted because of a non-ferromagnetic material beneath the surface, some magnetic flux leaks and causes a local attraction for magnetic particles which are suspended in a solution and washed over the surface. The results of the indications are expressed as a size distribution of inclusions per m^2 of steel plate; for a 280 µm thick plate, this corresponds to sampling a 2.2 kg steel mass. This method is only applicable to ferromagnetic metals.

Microscopic techniques, by contrast, require a polished surface. Because of the magnification factor (typically 100 x), the scanned area is small (~1 mm^2). Hence, a large number of fields must be covered to obtain a representative sample, especially for the less frequent, larger inclusions. In one method, developed by Brush Wellman Inc. for copper-beryllium alloys, for example, a standard polished surface, 12 mm in diameter is scanned for the presence of oxide inclusions greater than 10 µm [55].

Sizing and counting of inclusions manually, using classical quantitative metallographic techniques proves to be accurate but very laborious. The desire to retain this accuracy, but at higher speeds of counting, has led to the development of automatic image analysers, based on optical or electron microscopy [56-58]. Since their first commercial introduction in 1963, considerable development has taken place in these instruments, especially in ensuring the repeatabilty of the results by overcoming the earlier difficulties of threshold adjustment. Because of their increased reliability, automatic image analysers are now more popular, but still suffer from a considerable time delay between taking a sample and obtaining results.

2.2.2 Radiographic and Ultrasonic Techniques

X-ray radiography has been used to detect large flaws that may be caused by macro-inclusions, gas voids or cracks in critical sections of castings and seam welds. The flaws are identified and registered on a T.V. monitor by the changes they cause in signal attenuation of the X-rays passing through thin sections. This non-destructive method is well suited for the quality control of the finished sections in critical applications, and the procedures are well documented in ASTM standards for different structural metals [59].

Ultrasonic sensing zone techniques to identify inclusions and flaws in solid, and inclusions in liquid metals have been researched extensively. Non-contact methods such as Electro-Magnetic Acoustic Transducers (EMAT's) and pulsed lasers coupled with laser interferometry, to generate and detect acoustic waves, have been developed to inspect hot blooms and slabs of steel at temperatures in excess of 1000°C [60]

The ultrasonic sensing zone probe for molten metals is similar in construction to the through transmission attenuation probe discussed in the previous section, but is designed to detect backscattered pulse-echo signals coming from individual inclusions This technique is claimed to have been developed successfully for aluminum by the Reynold's Aluminum Co [61] Attempts have been made to develop it for molten iron and steel in the University of Toronto [62-63] Its attractiveness lies in its ability to provide on-line information on the frequency of macro-inclusions in the melt As in other instruments that depend on wavelength for detection, only the particles greater than $\frac{1}{2}$ the signal wavelength will cause backscatter, and will be detectable by the ultrasonic method This severely limits the detectable inclusion size in molten metals, to 250 µm in molten aluminum for instance, with the presently attainable ultrasound frequencies of 10 MHz

2.2.3 Electric Sensing Zone Methods

These methods depend on monitoring local changes in electrical resistance caused by inclusions or other defects Eddy current techniques for detecting defects near the surface of solid metals, for instance, may be considered as sensing zone methods. In this technique, a primary coil carrying alternating current acts as the probe, and is moved along the metal surface that is to be inspected The metal becomes the secondary coil and contains induced eddy currents Discontinuities near a metal surface result in a local increase in electrical resistance, reducing eddy currents. These currents, in turn, change the magnetic flux and the inductance of the primary coil. By monitoring the impedance of the primary, flaws, including inclusions, can be sized and counted The method can detect inclusions as small as 50 µm and is suitable as a quality control device on the finished products [64]

A method known as the Coulter Counter represents another electrical sensing zone method, in which suspended particles in an aqueous fluid are sized and counted. The Coulter Counter was invented by Dr. Wallace Coulter in 1953, to rapidly count blood cells in plasma [65, 66]. Since than, it has been widely applied in powder technology to measure size and frequency of particles in aqueous suspensions.

In its principle of operation, the electrically conducting fluid is aspirated into an electrically insulating sampling tube through a small orifice. As a non-conducting suspended particle passes through the orifice, the electrical resistance across the orifice increases, and in the presence of an electric current (established by the suitably immersed electrodes in and outside of the sampling tube), a voltage pulse, of duration approximately equal to the transit time of the particle, is generated. The amplitude of the voltage change is, to a first approximation, proportional to the particle's volume. Thus, by electronically measuring and counting each pulse, the frequency size distribution of suspended particles can be obtained.

The Coulter Counter has been used to measure size distributions of extracted inclusions from steels and aluminum [67-69]. Chemical extraction is carried out by dissolving the metal matrix without affecting the inclusions. Extraction procedures and solvents have been developed for specific metals and inclusion types to increase the method's reliability For the extraction of oxide inclusions from steels, for example, halogens in organic solvents are currently being used [70]. Using chemical extraction and the Coulter Counter, valuable information has been obtained on the typical number of growing nuclei and the size distributions of micro and macro-inclusions in deoxidized steels [71-73]. However the extraction procedure is slow and laborious, and requires great care to avoid artifacts or losses in the extracted residue.

A method developed at McGill in 1980, deriving from the original Coulter Counter principle, overcame this shortcoming by taking measurements directly in molten metals [74]. The method was developed for aluminum melts, in collaboration with Alcan, to obtain on-line information on the size distribution of inclusions greater than 20 µm. The technique has been given the acronym LiMCA for Liquid Metal Cleanness Analysis (see Fig. 2). In a later study, carried out by this author using LiMCA, it has also been found possible to measure size distributions of borosilicate inclusions in a boron - silicon steel [75]. The distinct features of LiMCA over other methods of inclusion measurements in metals can be summarized as follows:

Fig. 2: Commercial LiMCA equipment (by BOMEM Inc.) for Alcan's casting centers

1. Measurements are made available rapidly and can be used on-line, to monitor molten metal quality while it is being processed

2. Because of the sample volume analysed, the sample size is a great deal larger than the typical sample sizes obtainable by other methods based on surface examination. This allows statistically adequate characterization of the macro-inclusions in the melt. The detailed particle size information can be used to construct the right hand side of the inclusion size distribution curve This is particularly useful, since information on larger inclusions are usually of interest in characterizing the effect of inclusions on properties

3. LiMCA measurements do not provide information on the chemistry, shape or the physical state (whether particles are solid, liquid or gas) of inclusions. However, as mentioned earlier, inclusion chemistry is process dependent and

> tends to be fairly predictable, whereas greater variability in inclusion size and number density occurs as a result of incomplete physical separation.

Because of its advantages, it was desirable to extend the range of applicability of LiMCA to other metals of industrial importance, and this was the objective of the work described in this thesis The next chapter describes the development of a LiMCA instrument and its operation, while the following parts deal with its application to high temperature melting point and reactive metals, such as steels, copper and magnesium alloys.

3. THEORETICAL CONSIDERATIONS AND EVOLUTION OF LiMCA

LiMCA may be considered to be an innovation based on the Coulter Counter technique for counting and sizing of inclusions in molten metals, in situ. Both Coulter Counter and LiMCA consist of the following 3 parts:

1. Probe: Sampling Tube and Electrodes
2. Power Supply
3. Data Acquisition and Display System

These parts are illustrated schematically in Fig. 3. The principle of its operation has already been described in the final section of the previous chapter The sampling tube contains the orifice at its lower end, which establishes the sensing zone in the presence of a D.C. electric current. The data acquisition and display system measures and records the resistive voltage pulses caused by the passage of suspended particles during aspiration of liquid metal into the sampling tube. Fig 4 illustrates the generation of a resistive voltage pulse at the orifice.

3.1 Relationship between Particle Size and Resistance Change across Orifice

A simple expression for the resistance change caused by the introduction of a small, spherical particle into a sensing zone was derived by DeBlois and Bean [76], using a relation first proposed by Maxwell. Maxwell showed that, for a dilute suspension of insulating spheres, the effective resistivity could be expressed as:

$$\rho_{eff} = \rho\,(1 + \frac{3}{2}V_f + \quad) \tag{2}$$

where ρ is the electrical resistivity of the fluid and V_f is the volume fraction occupied by the spheres. Using Ohm's law, resistance of a cylindrical sensing zone of length L, diameter D, filled with a fluid of resistivity ρ, is given by:

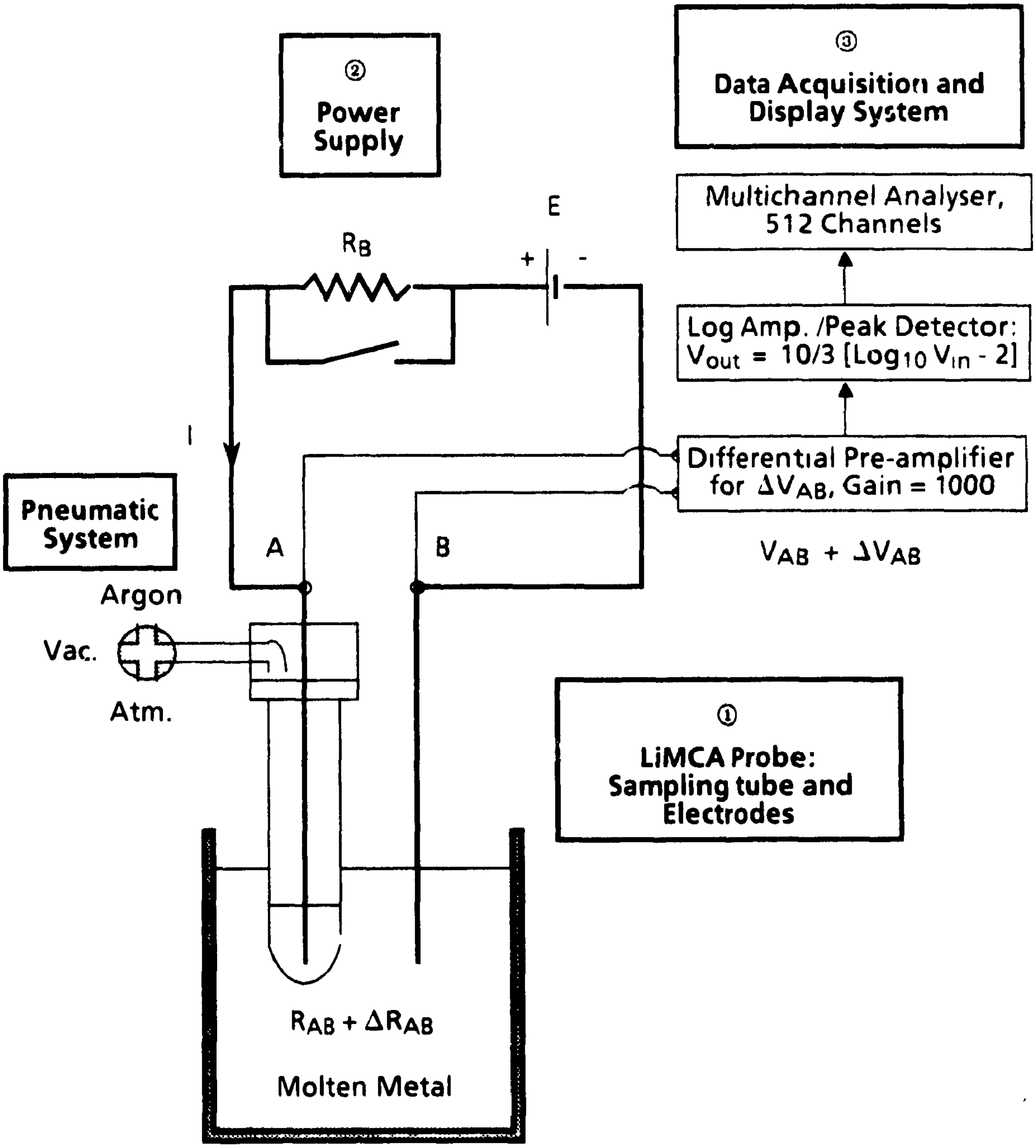

Fig. 3: LiMCA instrument.

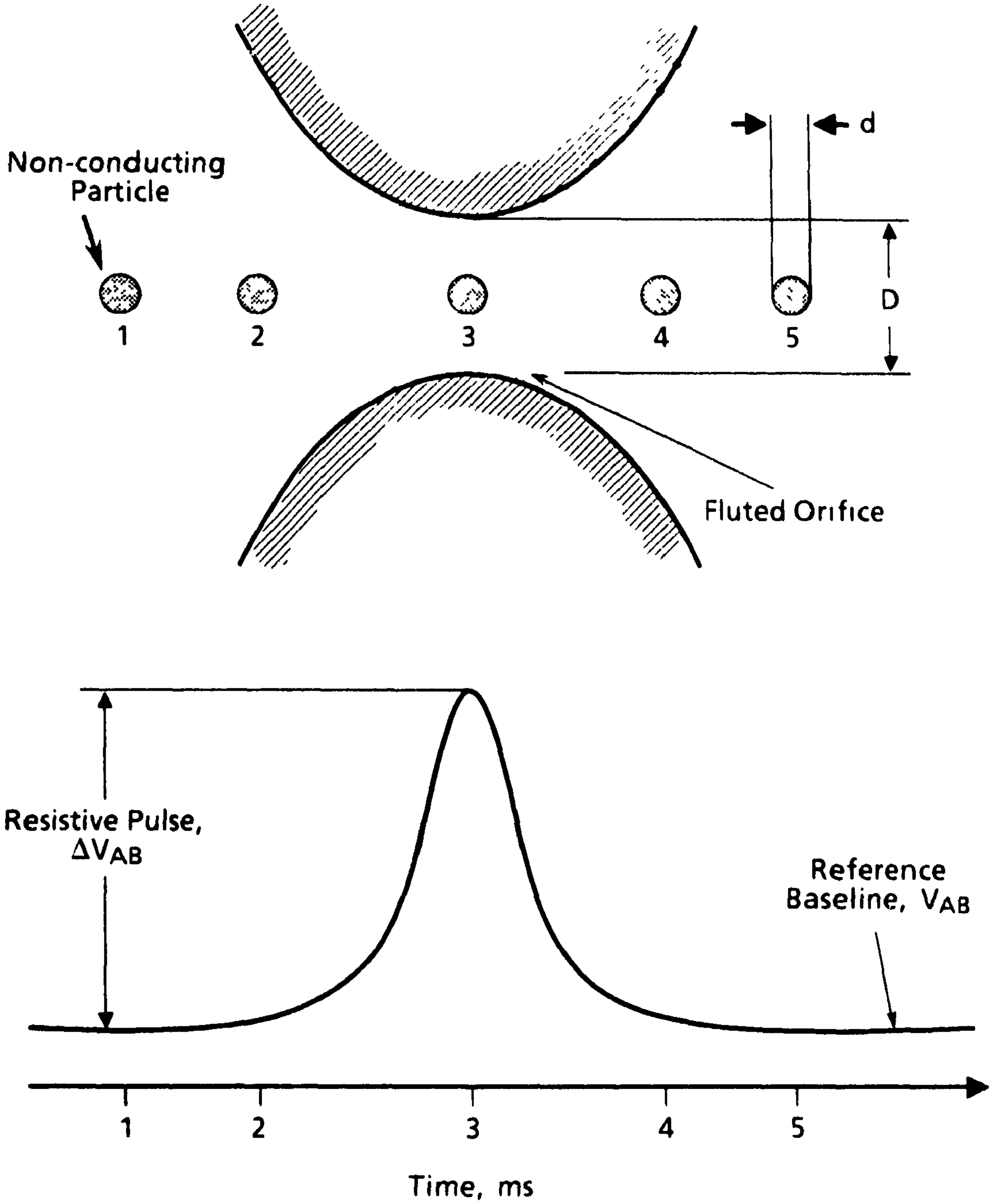

Fig. 4: Generation of a resistive voltage pulse in LiMCA.

$$R_0 = \rho \frac{L}{\frac{\pi}{4} D^2} \tag{3}$$

When a particle of diameter d is introduced into the sensing zone, the fluid may be considered a dilute suspension, and the particle's volume fraction is:

$$V_f = \frac{volume\ of\ particle}{volume\ of\ sensing\ zone} = \frac{\frac{\pi}{6} d^3}{\frac{\pi}{4} D^2 L} = \frac{2\, d^3}{3\, D^2 L} \tag{4}$$

Substituting (3) into (1), into (2) gives:

$$R_1 = \rho \left(1 + \frac{d^3}{D^2\, L} + \ldots \right) \frac{L}{\frac{\pi}{4} D^2} \tag{5}$$

Subtracting (4) from (2) gives the change in resistance because of an insulating particle introduced into an orifice:

$$\Delta R = \frac{4}{\pi} \cdot \frac{\rho\, d^3}{D^4} \quad . \tag{6}$$

Equation (6) predicts the resistance change to be independent of orifice length and directly proportional to the particle's volume. This approach is more accurate than the alternative of integrating a shell equation based on Ohm's law, and assuming a uniform electric field around a spherical particle:

$$\Delta R = \rho \int_0^L \left[\frac{1}{A(x)} - \frac{1}{\frac{\pi}{4} D^2} \right] dx \tag{7}$$

where $A(x)$ is the area of orifice occupied by the fluid at an axial distance x from the entry. For small, spherical particles, this will yield:

$$\Delta R = \frac{8}{3\pi} \cdot \frac{\rho d^3}{D^4} \tag{8}$$

This equation predicts a smaller change in resistance than eqn. (6), by a factor 2/3. The discrepancy arises, because highly curved surfaces, e.g. small particles, will distort the electric field locally and will cause a greater change in resistance than that would be predicted by assuming a uniform field.

Equation (6) applies for an infinitely small, spherical particle, and does not take into account the effect of orifice shape on electric field. Although a complete analytic solution for the problem covering all sizes and geometries does not exist, eqn. (6) can be used as a correct starting point, and numerical solutions have been proposed to check the range of its validity Using a hydrodynamic analogy, for instance, Smythe has shown that the exact values for ΔR_{AB} are only greater by +2% at $d/D = 0.3$ and +5% at $d/D = 0.4$ [77]. For larger particles, a correction factor, $F(d/D)$ may be included in the expression for ΔR_{AB}. A table of calculated values, d/D vs. $F(d/D)$, has been presented by Smythe. DeBlois, Bean and Wesley, however, have proposed the analytic expression [78]:

$$F(\frac{d}{D}) = \left[1 - 0.8(\frac{d}{D})^3 \right]^{-1} \tag{9}$$

The correction factor is accurate to within 1% at $d/D = 0.8$, its accuracy increases as the value of d/D becomes smaller.

Although eqn. (6) was derived for spherical particles, Lloyd [79] has shown that particle shape and orientation are insignificant for $d/D \leqq 0.2$, the system responding solely to particle volume d in this instance, would refer to the equivalent spherical diameter for non-spherical objects. Similarly, the more spheroidal-like are the particles, the less significant are deviations from eqn. (6).

Finally, particle trajectories have been shown to have a significant effect on eqn. (6) in right cylindrical sensing zones with sharp edges at their entry and exit [80, 81]. Because of a non-uniform distribution in the potential gradient across a cross-section, which greatly increases near the edge, particles following off-axis trajectories cause a larger transient change in resistance than that which would be predicted by eqns. (6) and (9). The avoidance of sharp edges by using a fluted orifice (such as that shown in Fig. 4), results in a much more uniform potential gradient distribution across any given cross-section of a sensing zone, and largely eliminates this problem [82]. A fluted sensing zone was also found to favour the establishment of a low noise reference baseline, over which resistive voltage pulses were counted: it was therefore a preferred sensing zone shape for LiMCA instruments.

The reliability of eqns. (6) and (9) in predicting transient changes in resistance in an orifice was tested with respect to particle size, orifice diameter and applied current by using gallium (m.p. 30°C), and introducing insulated steel spheres into electric sensing zone [83]. The equation predicting the magnitude of voltage pulses was found to be in excellent quantitative agreement with those measured.

3.2 Analysis of LiMCA's Electric Circuit

Figure 5 shows a typical diagram of an electric circuit for resistive pulse counting in liquid metals. A battery with an e.m.f. E drives a current I, while a ballast resistance R_B regulates this current. The passage of particles cause transient voltage pulses across the electrodes, ΔV_{AB}, and also interestingly, across the ballast resistor, ΔV_B, riding on steady potential differences V_{AB} and V_B, respectively. As shown by the following derivation, the magnitudes of ΔV_{AB} and ΔV_B are equal and opposite in sign, such that the potential across the battery remains constant at any given moment:

$$V_{AB} = \frac{R_{AB}}{R_{AB} + R_B} E , \qquad V_B = E - V_{AB} \tag{9}$$

$$\Delta V_{AB} = \left(\frac{\partial V_{AB}}{\partial R_{AB}} \right)_{R_B} \Delta R_{AB} \quad and \quad \Delta V_B = \left(\frac{\partial V_B}{\partial R_{AB}} \right)_{R_B} \Delta R_{AB} \tag{10}$$

$$\Delta V_{AB} = -\Delta V_B = \frac{R_B}{(R_{AB} + R_B)^2} E \cdot \Delta R_{AB} \tag{11}$$

$$since \qquad I = \frac{E}{R_{AB} + R_B}$$

$$\Delta V_{AB} = -\Delta V_B = \frac{R_B}{R_{AB} + R_B} I \, \Delta R_{AB} = \frac{V_B}{E} \cdot \frac{4}{\pi} \frac{\rho I d^3}{D^4} \cdot \left[1 - 0.8 \left(\frac{d}{D} \right)^3 \right]^{-1} \tag{12}$$

This fact can be used to advantage by monitoring the transient potentials across the ballast resistance, rather than across the hot probe.

When the ballast resistance R_B is much greater than R_{AB}, the effect of the division of electric potential between probe and the ballast resistance in eqn (12) becomes negligible. However, for a given e.m.f., making R_{AB} too great, will make circuit current too low and resistive voltage pulses too small. Therefore, an optimum value of ballast resistance exists to obtain maximum pulse heights, R_{AB} being prescribed by the dimensions of the orifice and the resistivity of the fluid medium. This optimum can be found by differentiating ΔV_{AB} in eqn. (11) w r t. R_B, keeping R_{AB} constant, and equating the derivative to zero:

$$\left(\frac{\partial V_{AB}}{\partial R_B}\right)_{R_{AB}} = \frac{(R_{AB}+R_B)^2 - 2\,(R_{AB}+R_B)\,R_B}{(R_{AB}+R_B)^2}\,E \cdot \;\Delta R_{AB} = 0$$

$$R_{AB} = R_B \tag{13}$$

Hence, matching the ballast resistance with the resistance across a probe will maximize the pulse heights. This is particularly applicable to Coulter Counter type probes, operating in aqueous medium, where resistance across a probe is typically 100 kΩ. In LiMCA, on the other hand, this resistance is of the order of a few mΩ's, and having a matching ballast resistance coupled to a 6 V battery will generate too great a current that will put excessive thermal load on the orifice. For LiMCA, therefore, the ratio of electric potential across the ballast resistor, and the battery e.m.f., is closer to unity.

3.3 Data Acquisition and Display System

For electronic processing of LiMCA signals, as shown in Fig. 3, the voltage pulses were first strongly amplified using an oscilloscope / differential pre-amplifier, with a gain G usually set at 1000. The oscilloscope trace allowed one to observe a steady D.C. baseline, referenced as zero and corresponding to the steady potential drop V_{AB}, and the transient resistive voltage pulses ΔV_{AB} which rode over this baseline. The high pass filter was set at an appropriate level, between 0.1-1 kHz, to automatically restore the baseline to its zero reference level, should a change in V_{AB} (low frequency oscillations or sudden permanent changes) occur. The low pass filter was usually set at 10 kHz, to eliminate as much high frequency noise as possible. A logarithmic amplifier / peak detector with a variable pulse rise time amplified and conditioned the pre-amplifier output signals whose magnitudes could vary in the range from 10 mV to 10 V, to 0 to 10 Volts, each cycle of magnitude being placed linearly on a 3.3 V band,so as to condition signals for acquisition by a Multi Channel Analyser (M.C.A.). Since resistive pulse signals had fixed periods determined by the rate of metal flow through the orifice, appropriate setting of pulse rise time was used to screen out any spurious peaks having much longer or shorter rise times Finally, signals were recorded in a multichannel analyser, in individual channels that corresponded to logarithmically spaced pulse height intervals. The MCA therefore, effectively displayed a histogram of the number of peaks observed as a function of their magnitude. This pulse height information was then converted into particle size distribution through the use of eqn. (12).

3.4 Comparison of Coulter Counter Technique and LiMCA

LiMCA for molten metals was developed thirty years after Coulter's invention in 1953. The primary difficulty in developing a similar E S.Z. device for molten metals, when compared with aqueous electrolytes, was their very low electrical resistivity (~ million times lower), which made the resistance changes caused by particles displacing liquid metal in the orifice (see eqn. (6)), very much smaller. To obtain measurable voltage pulses, the circuit current was made much higher, while the pulse height detection limit was greatly lowered by reducing the inevitable background noise on the reference baseline as far as possible. This was accomplished through the use of sensitive electronics and by electromagnetic shielding and appropriate grounding of circuit components. Ripple free D C currents were generated by utilizing a 6 Volt heavy duty lead-acid storage battery Hence, the significant difference in the design of a Coulter Counter and a LiMCA is the use of a very low impedance circuit which enables high D.C currents to pass and, at the same time, helps to minimize electromagnetic induction on circuit components. Presently, for operations in most molten metals, background electronic noise can be reduced below 10 µV, allowing resistive voltage pulses above a threshold value of 20 µV to be counted.

Table 1 compares the typical operating conditions of E.S.Z. devices using water and various molten metals as the measuring media. As can be seen, for a given size orifice, the minimum particle sizes that can be currently detected in metals at McGill University are about twice as those in water.

3.5 Application of LiMCA to reactive and / or high melting point metals

Referring to Fig. 3, therefore, a major innovation in conceiving LiMCA was in the design of the second component, the power supply. The circuit was first tested in

Table 3. Comparison of E.S.Z. instruments in water and molten metals.

	Tap Water [84]	Aluminum [83]	Magnesium [85]	Copper [86]	Silicon-Boron Steel [87]
Temperature of Operation, °C	20	700	700	1100	1350
Electric Resistivity, Ωm	30	0.25×10^{-6}	0.28×10^{-6}	0.20×10^{-6}	1.4×10^{-6}
Electric Current, Amperes	50×10^{-6}	60	60	60	20
Orifice Diameter, µm	300	300	300	300	300
Pulse Height Detection Limit, µV	200	20	20	20	20
Minimum Particle Size Detected, µm	9.5	20	20	22	16.6
d/D, %	3.2	6.7	6.7	7.3	5.5

gallium, near room temperature, and after successful demonstration of the principle, was applied to aluminum. For measurements in aluminum, a LiMCA probe consisting of a heat resistant borosilicate sampling tube and steel electrodes, was developed. A fluted orifice measuring 300 µm diameter was produced at the lower end of the sampling tube by the application of a micro oxyacetylene flame, and a method of conditioning this orifice using a high current was discovered.

In its application to high temperature melting point and reactive metals, such as iron, copper and magnesium alloys, the electrical circuit design was essentially the same, but new probes had to be developed for each metal. This was not a trivial task, however As in LiMCA's earlier development, much greater effort was expended in developing a working probe for aluminum than testing the new electric circuit design in gallium [29].

In designing a LiMCA probe for a given metal or alloy, the following considerations applied:

1. Electrode designs capable of establishing a current path of high amperage (>20 Amps), with a low background noise (<20 μV), for a sufficiently long time (>20 minutes).

2. Sampling tubes resistant to thermal shock, resistant to chemical wear and electrically insulating.

3. Sensing zones (orifice) remaining dimensionally stable and providing a smooth entrance for molten metal.

The following sections expand on these criteria and give details of the development and testing of probe components.

3.5.1 Electrodes

It was generally found necessary to use freely dissolving electrodes, or an electrode system that at least reacted with a dissolved component in the molten metal. To test for reliable performance, independent tests were carried out on the electrodes. As shown schematically in Fig. 5, electrode arrangements were inserted into the melt without a sampling tube, and D.C. currents, equal in magnitude to the operating current of LiMCA passed. Background electronic noise was then monitored. Satisfactory performance indicated that noise problems due to environmental induction, shielding and grounding of circuit components, as well as any contacting problems between the electrode and molten metal had been overcome. Particularly, the electrode-melt interactions included wetting phenomena, slagging, formation of intermetallic compounds, dissolution, gas bubble generation, oxidation and the like.

3.5.2 Sampling Tube

In the construction of a sampling tube, it is easy to understand the need for thermal shock and chemical wear resistance. Electrical insulation can also be important, as most ceramic insulators become conducting at high temperatures. The

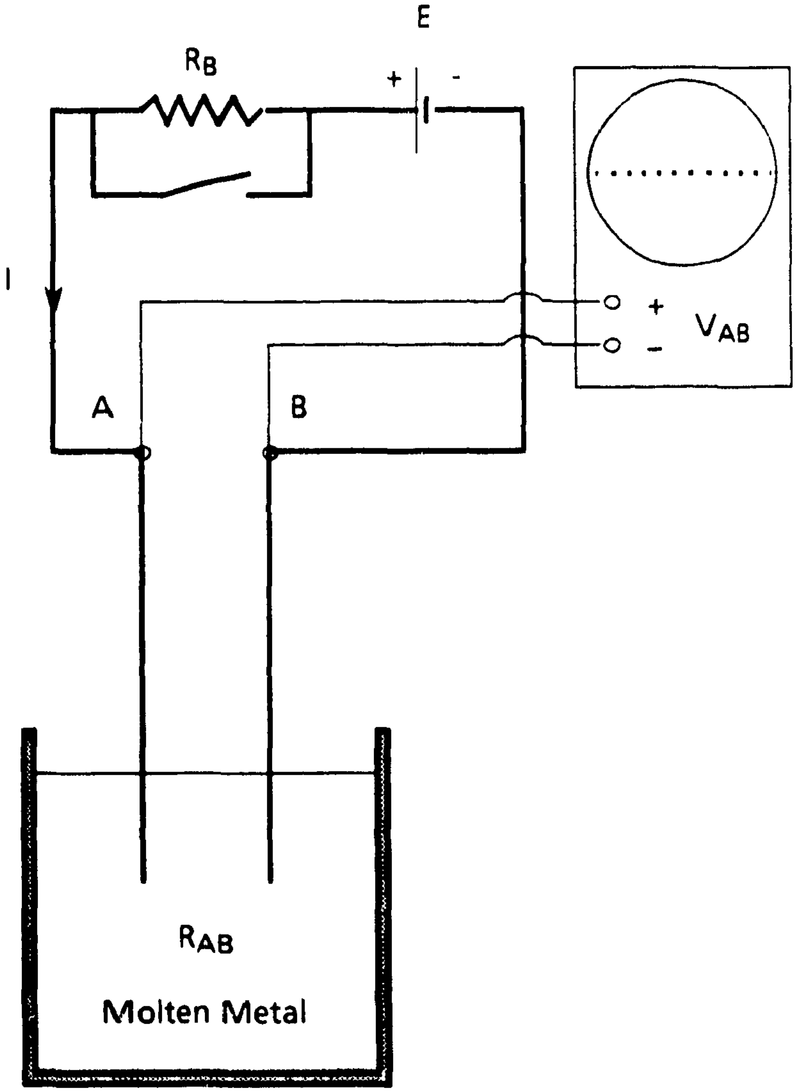

Fig. 5: Set-up for independent testing of electrodes.

effect of using a partially conducting sampling tube versus a completely insulating one, will be to lower the magnitudes of the resistive voltage pulses. Referring to Fig. 6, the extent of this lowering can be deduced as follows: when the sampling tube has a finite resistance, R_{AB} consists of two parallel resistances: the wall resistance of the sampling tube R_{ST} and the resistance of the molten metal within the orifice R_O. ΔR is the transient change in R_O caused by the passage of a particle through the

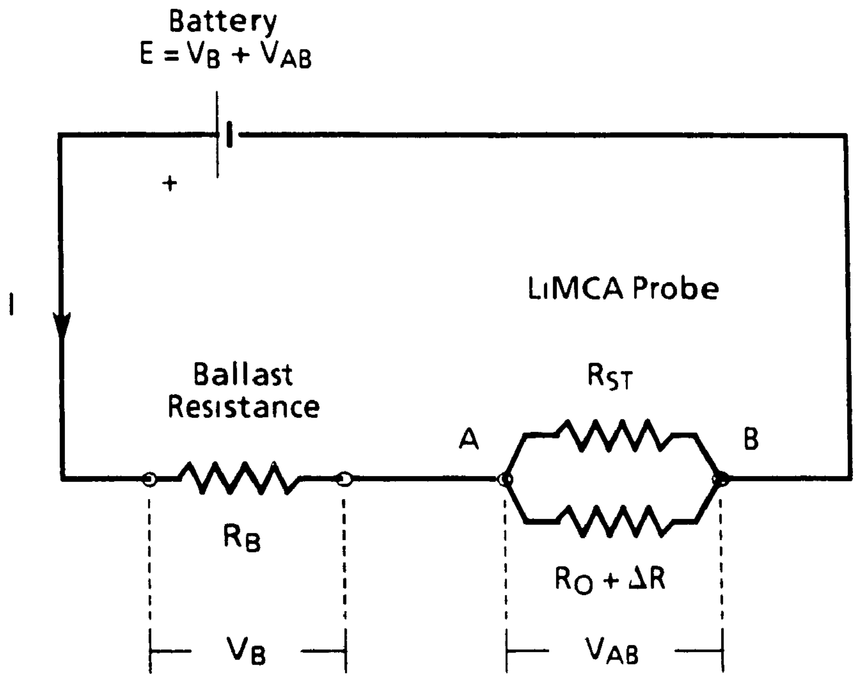

Fig. 6: Effect of a partially conducting sampling tube

orifice, its magnitude given by eqn. (6). The transient resistance change across AB, ΔR_{AB} will be given by:

$$\frac{1}{R_{AB}} = \frac{1}{R_{ST}} + \frac{1}{R_O} \quad \rightarrow \quad R_{AB} = \frac{R_{ST}R_O}{R_{ST}+R_O}$$

$$\Delta R_{AB} = \left(\frac{\partial R_{AB}}{\partial R_O}\right)_{R_{ST}} \Delta R \tag{14}$$

$$\Delta R_{AB} = \left(\frac{R_{ST}}{R_O + R_{ST}} \right)^2 \cdot \ \Delta R \tag{15}$$

Also from eqn. (12):

$$\Delta V_{AB} = \frac{R_B}{R_B + R_{AB}} \ I \cdot \ \Delta R_{AB} \tag{16}$$

when the sampling tube is completely insulating, $\Delta R = \Delta R_{AB}$. Hence, substituting (15) into (16):

$$\Delta V_{AB} = \Delta V_{AB}^{ins.\,tube} \cdot \left(\frac{R_{ST}}{R_O + R_{ST}} \right)^2 = \Delta V_{AB}^{ins.\,tube} \cdot \ f(\alpha) \tag{17}$$

where $\alpha = R_O/R_{ST}$, and $f(\alpha) = [1/(1+\alpha)]^2$. If no more than 10% reduction in pulse height can be tolerated, then $f(\alpha) > 0.90$ and $\alpha < 0.05$. Assuming the wall thickness and the orifice length to be the same,

$$\alpha = \frac{R_O}{R_{ST}} = \frac{\rho_M / A_O}{\rho_{ST} / A_{ST}} < 0.05 \qquad or \qquad \rho_{ST} > 20 \frac{A_{ST}}{A_O} \cdot \ \rho_M \tag{18}$$

where A_{ST} is the area of sampling tube exposed to molten metal, and A_O is the orifice area. For a 300 µm diameter orifice in a 40 mm diameter sampling tube, inserted 40 mm deep into a steel bath, for instance:

$$\rho_{ST} > 20 \, \frac{\frac{\pi}{4}\,40^2 + \pi\,(40)(40)}{\frac{\pi}{4}0.3^2} \quad (1\;4 \quad 10^{-6}) = 2\;5\,\Omega m$$

Stabilized zirconia has good thermal shock resistance and is resistant to chemical wear in molten steels. However, because of its low resistivity, 0.094 and 0 016 Ω.m at 1300°C and 1600°C, respectively [88], it is clearly not suitable as a sampling tube material

3.5.3 Sensing Zone

The orifice that serves as the sensing zone has been found to be the most critical region in LiMCA's operation. It is required to have dimensional stability against chemical erosion or physical attachment of inclusions to its walls, in the presence of rapid fluid flow and converging streamlines. It can be generated on the side of a sampling tube, as has been the case with borosilicate or quartz tubing, or can be produced as an insert, made of a superior material such as BN, that is subsequently attached to a sampling tube of less expensive ceramic

In LiMCA's operation, when an unstable baseline develops, it is important to establish the source of electronic noise causing interference. This can be diagnosed by by-passing the inside electrode in the sampling tube with another electrode, into the melt, hence removing the orifice from the current path. If a steady reference baseline returns, then the cause can be attributed to orifice deterioration, possibly caused by inclusion attachment and loss of smooth surface at the orifice wall. If electronic noise persists, then, other sources such as imperfect electrical contacts, or environmental noise, could be of suspect.

REFERENCES

1. P.M.B. Walker Gen. Ed in *Chambers Dictionary of Science and Technology*, W.&R. Chambers, Edinburgh, U.K., 1988.

2. Sybil P. Parker, Ed. in Chief, in *McGraw Hill Dictionary of Scientific and Technical Terms*, McGraw-Hill, New York, 1984.

3. D. Birchan, in *Dictioanary of Metallurgy*, The Chauser Press, 1965.

4. *Metals Handbook, Vol. 9: Metallography and Microstructures*, pp. 9, ASM, Metals Park, Ohio, 1985.

5. I.D. Sommerville and S. Dawson, "Inclusions: Their formation, detection and control", in *Troubleshooting the Steel Casting Processes*, Conf. Proceedings, pp. 1-60, Steel Founders' Soc. of America, Schaumburg, Illinois, 15 Nov. 1987.

6. D.J. Lloyd, "Metal matrix composites, an overview", *Int. Symp. on Advanced Structural Materials*, CIM, 27th Ann. Conf. of Metallurgists, Montreal, Aug. 28-31, 1988.

7. B.A. Mikucki et al., "Magnesium matrix composites at Dow: Status update', *43rd Annual World Magnesium Conf.*, pp. 13-23, L. A., California, June 1968.

8. *Oxide Dispersion Strengthening*, Metallurgical Soc. Conferences No. 47, Second Bolton Landing Conf., Bolton Landing, N.Y., June 27-29, 1966.

9. J.E. Hillis, "The effects of heavy metal contamination on magnesium corrosion performance." *Society of Automotive Engineers*, Paper No. **830523**, 1983, pp. 553-559.

10. T. Tanaka, S. Asami, and K. Nishitsuji, "Agglomeration and settlement of TiB_2 particles in molten aluminum", *Aluminum*, **58**, (10), 1984, pp. 600-604.

11. E.F. Emley, In *Principles of Magnesium Technology*, pp. 180, Pergamon Press, New York, 1966.

12. R. Kiessling, "Clean steel - a debatable concept", *Proceedings of the Second Int. Conf. on Clean Steel*, Balatonfured, Hungary, June 1-3, 1981, pp. 1-9, The Metals Society, London, 1983.

13. T. Emi and Y. Iida, "Impact of injection metallurgy on the quality of steel products", *Scaninject III, 3rd Int. Conf. on Refining of Iron and Steel by Powder Injection*, pp 1.1-1.31, Lulea, Sweeden, 15-17 June 1983.

14. D. Brookbank and K.W. Andrews, "Stressfield around inclusions and their relation to mechanical properties", *Production and Application of Clean Steels*, Int. Conf. at Balatonfured, Hungary, 23-26 June 1970, pp. 186-198, The Iron and Steel Institute, London, 1972.

15. F.B. Pickering, "The need for inclusion assessment", in *Inclusions*, Ed. F.B. Pickering, Institution of Metallurgists, Monograph No. 3, pp 182-198, Chameleon Press, London, 1979.

16. W.R. Bandi, "Second phases in steel", *Science*, **196**, (4), 1977, pp.136-142.

17. J. Briggs and W. Simmons, "Inclusions in cast iron", *Foundry Pract.*, **212**, Mar 1986, pp. 11-15.

18. W Schneider, "Requisite characteristics of AlTiB pre-alloys for the grain refinement of aluminum Part II", *Aluminum*, **64**, (2), 1988, pp 157-160

19. P. Reznicek and M. Halmanova, "Assessment of faults in aluminum castings using the SEM", *Aluminum*, **64**, (1), 1988, pp 76-79

20. C.C. Baker, "The effect of non-metallic inclusions and test temperature on the fatigue life of cast C355, 354 and A206 aluminum", *Int. Symp. for Testing and Failure Analysis*, pp. 299-307, ASM, Los Angeles, California, 20-24 Oct 1986

21. H Pops and G. Kingsbury, "On the origin of twist test cracks in copper rod", *Wire J. Int.*, **21**, (1), 1988, pp. 58-71.

22. S. Nourbakhsh and J. Nutting, "The metallography of cuboid shaped inclusions in commercial Cu-Be-Co alloy" *J. Mater. Sci* , **14**, (11), 1979, pp 2642-2644.

23. G.A. Chadwick "Castings - current practice and future potential", *Metals and Materials*, **2**, (11), 1986, pp 693-698.

24. B. Lagowski "Reacted sand inclusions and their effect on the tensile properties of magnesium alloys", *83rd Annual Mtg., American Foundrymen's Soc.*, Birmingham, Alabama, 30 Apr.-4 May 1979.

25. H.P. Haastert, H. Richter, H. Taxhet, and J Wolf, "The use of various desulfurization agents and their efects on Steel cleanness and service properties" *Proceedings of the Second Int. Conf. on Clean Steel*, Balatonfured, Hungary, June 1-3, 1981, pp. 281, The Metals Society, London, 1983.

26. K. Kawakami, "Metallurgical researches and developments - hot direct rolling", *4th Int. Conf. on Continuous Casting*, Brussels, Belgium, 17-19 May 1988.

27. H. Iso et al., "Progress on continuous casting and direct rolling process at Sakai works", *Steelmaking Proceedings*, ISS, 5th Int Iron and Steel Cong , pp 457-466, Washington, D.C., 6-9 April 1986.

28. K. Ogawa, H. Matsumoto, T. Onoue, and K. Narita, "Changes of morphology of non-metallic inclusions of high carbon steels for wire rod by flux treatment", *Steelmaking Proceedings*, ISS, 5th Int. Iron and Steel Cong , pp 457-466, Washington, D.C., 1986.

29. D.A Doutre, "The development and application of a rapid method of evaluating molten metal cleanliness", PhD Thesis, McGill University,1984

30. D.J. Harris and T.C. Waram "The influence of inclusions on the formability of D&I tinplate, and casting practices developed for their control", *Second Int.*

Symp. on the Effects and Control of Inclusions and Residuals in Steels, pp. IV.27-IV.43, CIM, 25th Ann. Conf. of Metallurgists, Toronto, 17-20 Aug. 1986.

31. F. Moussy and C. Quennevat, "The effect of inclusions on steel properties: A new approach", in ref. 30, pp. IV.1-IV.11, 1986.

32. T.A. Khalifa, "Effect of inclusions on fatigue limit of a heat treated carbon steel", *Mater. Sci. Eng. A*, **102**, July 1988, (2), pp. 175-180.

33. W.E. Duckworth, "The achievement of high fatigue strength in steel", *Metallurgia*, **69**, Feb. 1964, pp. 53-55.

34. T. Lund and J. Åkesson, "Cleanliness requirements on rolling bearing steels", *SKF Steel Technical Report*, Jan. 1986.

35. M.T. Shehata, G.J. Biefer, and J.D. Boyd, "Effects of non-metallic inclusions on stepwise cracking behaviour of line pipe steels", in *Failure Analysis and Metallography*, Conf. Proceedings, pp. 263-277, ASM, Philadelphia, Pennsylvania, 15-18 July 1984.

36. M.B. Ives, R. Guo, and S.C. Srivastava, "Pitting nucleation in austenitic stainless steels", *10th Int. Cong. on Metallic Corrosion*, Madras, India, 7-11 Nov. 1987.

37. H-J. Fleischer et al., "Investigations into the degree of cleanliness of special steels with reference to deformation by rolling", *Proceedings of the Second Int. Conf. on Clean Steel*, Balatonfured, Hungary, June 1-3, 1981, pp. 10-21, The Metals Society, London, 1983.

38. H. Nordberg, cited in ref. 12, 1983, pp. 8.

39. W.M. Wojcik, R.M. Raybeck, and E.J. Paliwada, "Inclusion counting of steel residues as means of assesing the hot working performance of steel", *J. Metals*, **19**, 1967, (12), pp. 36-40.

40. D.M. Hercules and S. H. Hercules, "Analytical chemistry of surfaces, part II. Electron spectroscopy", *J. Chem. Education*, **61**, (6), 1984, pp. 483-489.

41. J.C. Smitthells, ed., "General physical properties", in *Metals Reference Book*, 5th edn., Butterworths, Boston, 1976.

42. G.V. Samsanov, ed., *The Oxide Handbook*, 2nd edn., IFI/Plenum Data Co., New York, 1982.

43. S. Johansson, "Inclusion assessment in steel using the new Jernkontoret inclusion chart II for quantitative measurements", *Proceedings of the Third Int. Conf. on Clean Steel, Balatonfured, Hungary,* pp. 60-67, Inst. of Metals, 1987.

44. J.R. Blank, "Methods for the assessment of non-metallic inclusions in steel", in *Inclusions*, Ed. F.B. Pickering, Institution of Metallurgists, Monograph No. 3, pp. 199-216, Chameleon Press, London, 1979.

45. J.E. Hilliard, "Measurement of volume in volume", in *Quantitative Metallography*, eds. R.T Dehoff and F N. Rhines, pp 45-76, McGraw-Hill, New York, 1968.

46 D.M. Cottingham, "Cleanness assessment of continuously cast steel", *Continuous Casting of Ferrous and Non-ferrous Metals*, Proceedings of Continuous Casting Symp., pp J1-J14, April 1965

47 T.L Mansfield, "Ultrasonic technology for measuring molten aluminum quality", *J. Metals*, **34**, Sept. 1982, pp. 54-57

48. S Dawson, M.Sc. Thesis, University of Toronto, 1986.

49. R.C. McAllister, "Superalloy cleanliness characterization by electron beam melting", in *Proceedings of the 1986 Vacuum Metallurgy Conf. on Speciality Metals Melting and Processing*, pp 75-79, ISS-AIME, Pittsburgh, Pennsylvania, 9-11 June 1986.

50. W.H. Sutton and I.D Clark, "Development of an electron beam melting test to evaluate the cleanliness of superalloys", *Conf. on Electron Beam Melting and Refining, State of the Art 1983*, ed. R. Bakish, pp 33-60, Bakish Materials Corp., 1983.

51. D. Doutre et al., "Aluminum cleanliness monitoring· Methods and applications in process development and quality control", *Light metals*, pp. 1179-1195, TMS-AIME, 1985.

52. "Standard practice for determining the inclusion content of steel", *American Society for Testing and Materials*, Designation E45-84, 1984.

53. G.R. Webster et al., "Detecting inclusions in tin mill products using the magnetic particle method" *Iron and Steelmaker*, Oct. 1985, pp 18-27

54. P. Neu, P Riggi, and B. Sarter, "Tinplate for D.I. can: Magnetic particle testing for microinclusion detection", *Proceedings of the Third Int Conf. on Clean Steel, Balatonfured, Hungary*, pp 99-105, Inst. of Metals, 1987.

55. R.L. Ashbrooke, private communication, Brush Wellman Inc., Cleveland, Ohio, 1986.

56. R. Lagneborg, S. Ekelund, and T. Werlefors, "Combined image and X-ray analysis in scanning electron microscopy for automatic multiparameter characterisation of non-metallic inclusions", *Proceedings of the Second Int Conf. on Clean Steel*, Balatonfured, Hungary, June 1-3, 1981, pp 39-62, The Metals Society, London, 1983

57. M.T. Shehata and J.D. Boyd, "Assessment of nonmetallic inclusions in steels by automatic image analysis", *Second Int. Symp on the Effects and Control of Inclusions and Residuals in Steels*, pp III.19-III 33, 25th Annual Conf of Metallurgists, Toronto, 17-20 Aug. 1986

58. T. Gladman, "Quantitative metallography: Recent experience with automatic image analysis", *Proceedings of the Third Int. Conf. on Clean Steel, Balatonfured, Hungary*, pp. 50-59, Inst. of Metals, 1987.

59. "Radiographic testing", *American Society for Testing and Materials*, Designation E94, 1984.

60 D.A. Hutchins, "Non-contact methods for ultrasonic inspection of steel", *Steel Industry / Researcher, Sensor Research Workshop*, Sponsored by CSIRA and CANMET, 1984, pp. 29-31.

61. T.L. Mansfield, "Reynold's 4M™ system capabilities and applications", *Proceedings of the 3rd Int. Aluminum Extrusion Tech. Seminar*, pp. 273-278, The Aluminum Assoc , Atlanta, 1984

62 N.D G Mountford and A McLean, "The detection of particles in molten Iron using a pulsed ultrasonic technique", *Steel Industry / Researcher, Sensor Research Workshop*, Sponsored by CSIRA and CANMET, 1984, pp. 97-98.

63 N.D.G Mountford et al , "The development of an ultrasonic sensor for metal quality in steel casting tundishes", *Steelmaking Proceedings*, ISS, 5th Int. Iron and Steel Cong., pp 699-704, Washington, D.C., 6-9 April, 1986.

64 V.S. Cecco, "Eddy current testing", *Steel Industry / Researcher, Sensor Research Workshop*, Sponsored by CSIRA and CANMET, 1984, pp. 21-27.

65 W.H. Coulter, "Means for counting particles suspended in a fluid", U. S. Patent No. 112819, 20 Oct. 1953.

66. W.H. Coulter, "High speed automatic blood cell counter and cell size analyser", *Poceedings of the National Electronics Conf.*, pp. 1034, Chicago, 1956.

67. D.A. Flinchbaugh, "Expanded capability of the Coulter Counter with a new aperture apparatus", *Analytical Chemistry*, **43**, 1971, (2), pp. 172-175.

68. D.A. Flinchbaugh, "Use of a modified Coulter Counter for determining size distribution of macroinclusions extracted from plain carbon steels", *Analytical Chemistry*, **43**, (2), 1971, pp. 178-182.

69. C.J. Siemensen, "Sedimentation analysis of inclusions in aluminum and magnesium", *Met. Trans.*, **12B**, 1981, pp. 733-743.

70. R.G. Smerko and D A. Flinchbaugh, "Recent progress in the chemical extraction of non-metallic inclusions", *J. Metals*, **20**, (7), 1968, pp. 43-51.

71. D.A. Flinchbaugh, "Determining size distribution of oxides in plain carbon steels by halogen-in-organic solvent extraction and Coulter Counter measurement", *Analytic Chemistry*, **41**, (14), 1969, pp. 2017-2023

72. R.M. Raybech, "Determination of particle size distribution of isolated non-metallic inclusions in steel", *Pittsburgh Conference on Analytical Chemistry and Applied Spectroscopy*, paper 63, 5 March 1967.

73. M. Ihida et al., *Trans. ISI Japan*, **6**, pp. 31-38, 1966.

74. D.A. Doutre and R.I.L. Guthrie, *Method and Apparatus for the Detection and Measurement of Particulates in Molten Metal*, U.S. Patent 4,555,662, Nov. 1985.

75. S. Kuyucak, "On-line detection of non-metallic inclusions in molten iron", M.Eng. Thesis, McGill University, Montreal, 1985.

76. R.W. DeBlois and C.P. Bean, "Counting and sizing of sub-micron particles by the resistive pulse technique", *Review of Scientific Instruments*, **41**, (7), 1970, pp. 909-915.

77. W.R. Smythe, "Flow around a sphere in circular tube", *Physics of Fluids*, **17**, (5), 1964, pp. 633-638.

78. R.W. DeBlois, C.P. Bean, and R.K.A. Wesley, "Electrokinetic measurements with sub-micron particles and pores by the resisitive pulse technique", *J. of Colloids and Interface Sci.*, **61**, (2), 1977, pp. 323-335.

79. P.F. Lloyd ,*Coulter Counter Electronics Conference*, 1968, cited in R. Kahrun, R. Davies, B.H. Kaye, and M.J. Clinch, "Studies on the Coulter Counter - Part I.", *Powder Technology*, **11**, 1975, pp. 157-171.

80. W.R. Smythe, "Off-axis particles in Coulter type counters", *Review of Scientific Instruments*, **43**, (5), 1972, pp. 817-818.

81. R. Wilson, "Calculation of the electric field within an electric sensing zone counter", *Particle Charactheristics*, **1**, 1984, pp 37-43.

82. R. Davies, R. Karhun, and J. Graf, "Studies on the Coulter Counter-Part II", *Powder Technology*, **12**, 1985, pp. 157-166.

83. D. Doutre and R.I.L. Guthrie "On line measurements of inclusions in liquid metals", in *International Symp. on Refining and Alloying of Liquid Aluminum and Ferroalloys*, Engh, Lyng, Oye, Eds., pp. 147-163, Trondheim, Norway, 26-28 August 1985.

84. S. Kuyucak, H. Nakajima, and R.I.L. Guthrie ,"On-line measurement of inclusions in liquid steel", *Process Technology Proceedings*, ISS, 5th Int. Iron and Steel Cong., Washington, D.C., pp. 193-198, 1986.

85. S. Kuyucak and R.I.L. Guthrie, "On-line detection and measurement of inclusions in molten alloys of magnesium", *26th Ann. Conf. of Metallurgists*, CIM, Winnipeg, 23-26 August 1987.

86. S. Kuyucak and R.I.L. Guthrie, "On the measurement of inclusions in copper based melts", *Can. Met. Quart.*, **28**, (1), 1989, pp. 41-48.

87. S. Kuyucak and R.I.L. Guthrie, "On-line inclusion detection and measurement in a transformer steel", *Second Int. Symp. on the Effects and Control of Inclusions and Residuals in Steels*, pp. I.-I., CIM, 25th Annual Conf. of Metallurgists, Toronto, 17-20 Aug. 1986.

88. Peter T.B. Shaffer, in *High Temperature Materials, No. 1*, Plenum Press, New York, 1964.

89. *Fractography of Modern Engineering Materials: Composites and Metals*, ASTM STP 948, J.E. Masters and J.J. Au, Eds., American Soc. for Testing and Materials, Philadelphia, 1987.

List of Figures

List of Tables

PART 2: APPLICATION OF LiMCA TO STEEL AND CAST IRON MELTS

1. INTRODUCTION

Next to aluminum, the potential application of LiMCA to steels was given first priority in view of the technological benefits such an instrument can bring to this important structural material. Working probes were therefore developed, despite the difficulties involved, for steel melts. LiMCA's operation in steel was found to be strongly influenced by the melt's chemistry and the nature of its inclusions.

2. EXPERIMENTS WITH TRANSFORMER STEEL ALLOY, Fe, 5% B, 3% Si

The first successful LiMCA measurements in iron-base melts were made in an iron melt containing boron and silicon. This particular industrial alloy is used in the manufacture of magnetically soft sheets and strips of iron for transformer cores, and is produced by Metglass Division of Allied Corp., N.J., U.S.A. It has a low melting point, in the region of 1200°C, and planar flow casting techniques are used to produce thin sheet (50 µm thick) with a metallic glass structure. The elimination of magnetic domain boundaries gives this steel its "super soft" magnetic properties.

It was desirable to monitor and control the levels of borosilicate inclusions in this steel alloy. The following section gives a summary of the earlier work by the author to produce a working probe in this steel [1], and then describes further developments.

2.1 Development of LiMCA Probe for the Transformer Steel Alloy

First, independent electrode tests (see PART 1, Section 3.5.1) were carried out to find a suitable electrode system. Among the many high temperature conductors, such as steel, molybdenum, tungsten, and graphite rods tested, a combination electrode, with a graphite tip and a molybdenum rod extension was found to be the best. The molybdenum rod was threaded into the graphite, and a small amount of tin was used at the threaded connection to improve the electrical contacts. Both graphite and molybdenum were shielded at their side with refractory tubing of alumina or mullite to avoid rapid dissolution of graphite in molten steel, and atmospheric oxidation of molybdenum to volatile MoO_3. Dissolution of graphite occured only at the tip of the electrode, and as the electrode receded into the refractory shield, expectedly, the rate of dissolution of graphite became slower. Since carbon rich steel was lighter than the bulk, the effect of natural convection was greatly reduced in transporting dissolved carbon, from the electrode tip, to the bulk of steel.

Electrodes assembled in this way lasted an indefinite period in low m.p. steel alloys, indeed, little dissolution occured in alloys containing a high level of silicon (>2% Si). Usually, a high electronic noise accompanied the initial functioning of these electrodes, as shown in Fig. 1A. Following prolonged contact, or conditioning procedures, the background noise could be reduced sharply, to a level acceptable for particle detection measurements, Fig. 1B. This electrode arrangement also worked in a low carbon steel at 1550-1600°C; the rate of dissolution of graphite was measured to be 20-30 mm into the protective electrode shield, within a 20 min. period.

Earlier construction of a sampling tube for these melts consisted of a 15 cm long BN tube with a quartz tube extension. An orifice was drilled into a BN insert which was attached to the side of the BN tube. An alumina base cement (Aremco 503) was used to fix the various components and to provide gas tight seals. The complete probe asembly is shown in Fig. 2.

Fig. 3A shows one of the first resistive voltage pulses obtained in this steel using a similar probe. The thickness of the baseline is an indication of the electronic noise, which was kept well below 20 μV. One problem that remained with this design was orifice enlargement. BN was sensitive to the oxygen content in steel, and as seen in Table 2, unless dissolved oxygen was reduced to very low values, enlargement in orifice diameter occured. Another problem was the occurence of baseline jumps, one of which is seen in Fig. 3B. The jumps occured in either the positive or negative directions, and might have been caused by particles sticking, or becoming free, at the sensing zone. The positive jumps were counted as particles. The frequency of baseline jumps usually increased with continued measurement, and gave an

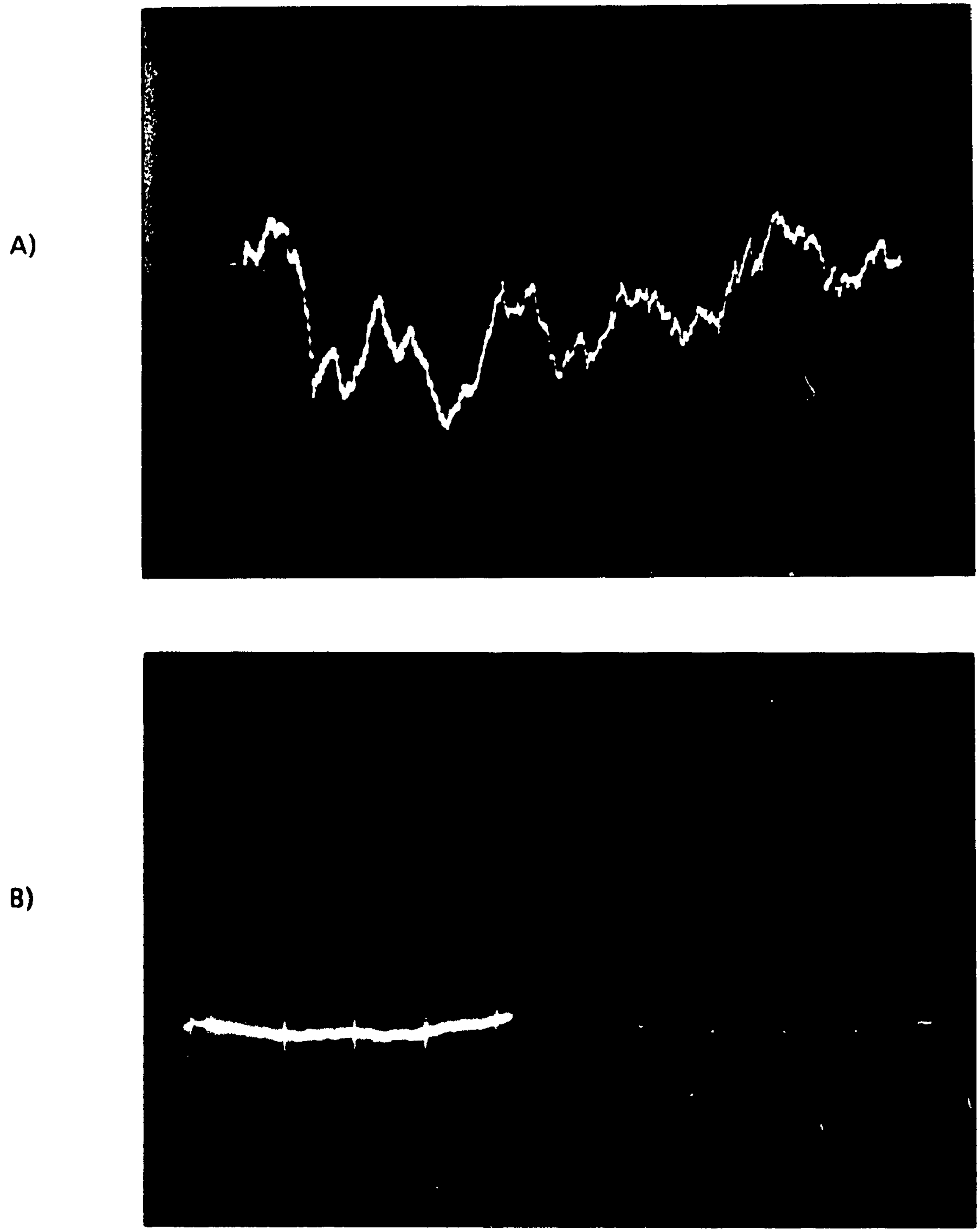

Fig. 1: Independent test of electrodes, oscilloscope traces showing initial electrode noise (A), and the establishment of a pulse-free baseline (B). Vertical displacement: 50 µV/div., time axis: 1 ms/div.

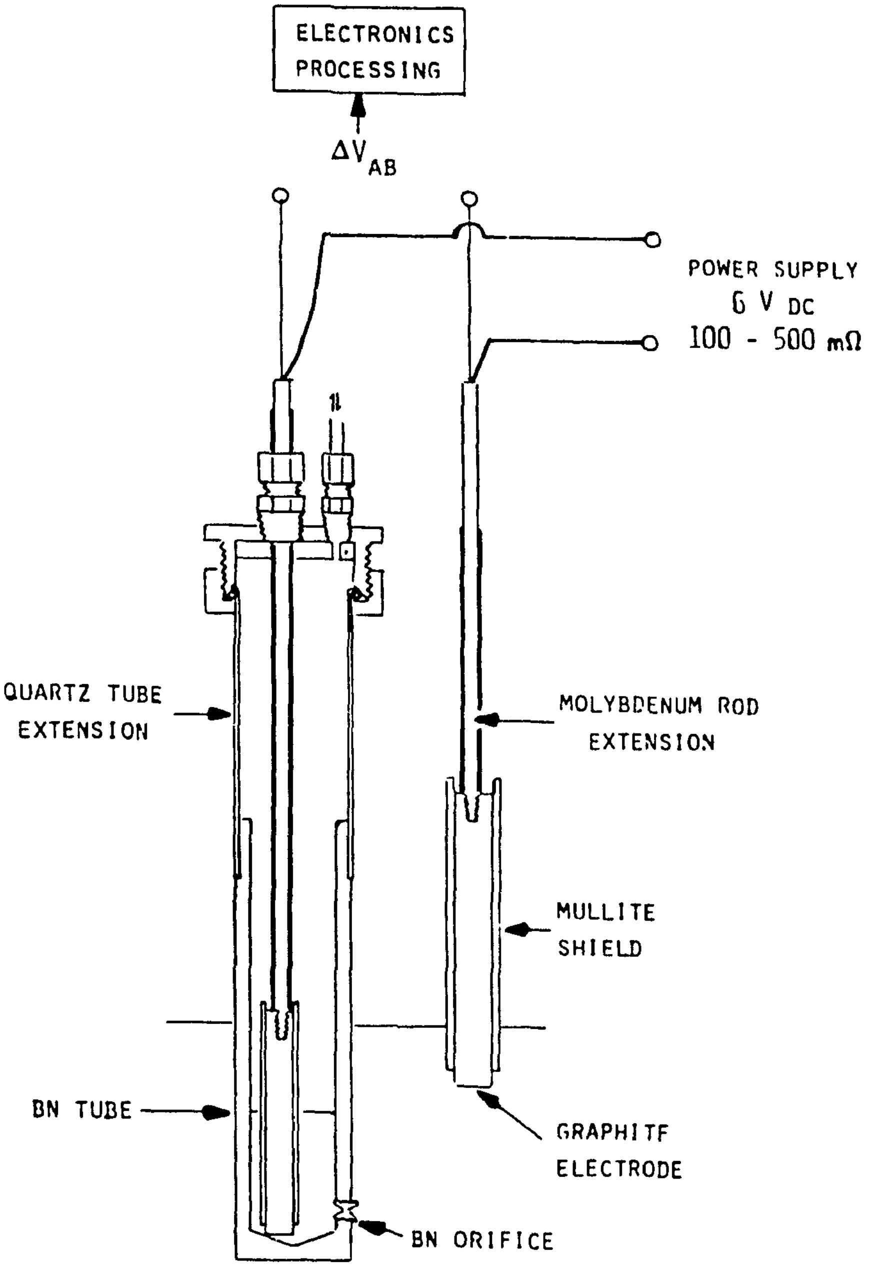

Fig. 2· LiMCA probe design for steel melts, incorporating a BN sampling tube with sensing zone contained in a BN insert, and refractory shielded graphite electrodes with molybdenum extensions

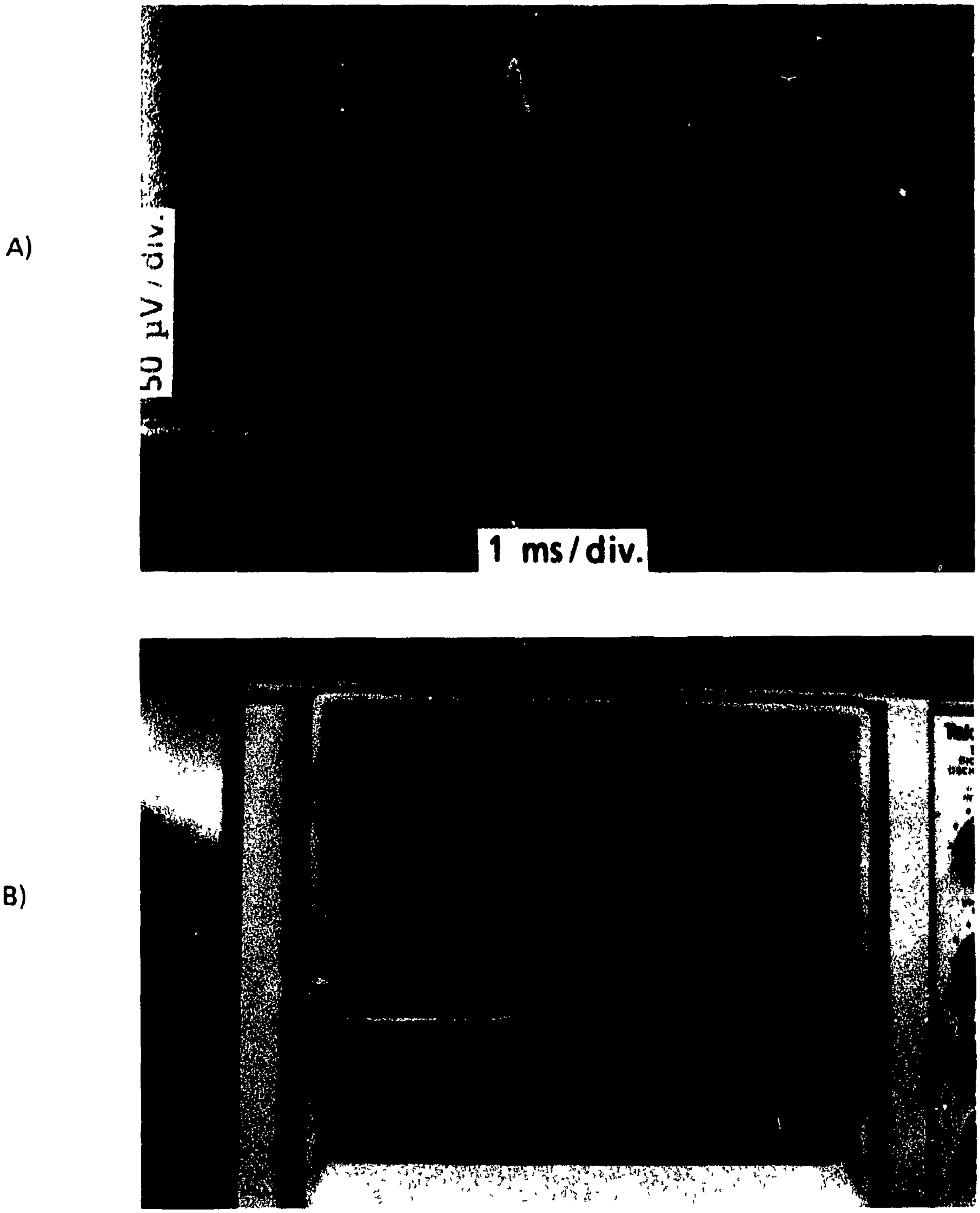

Fig. 3: (A) Resistive pulse obtained with the probe shown in Fig. 2. (B) Baseline jump. Vertical displacement: 50 µV/div., time axis: 1 ms/div.

Table 1. Typical rates of orifice enlargement for 300-400 µm diameter boron nitride orifices in steel and cast iron melts [1].

Metal Composition	*Rate of Orifice Enlargement, µm / aspiration*	*Temperature Range, °C*
Fe, 5% B, 3% Si, 400 ppm Al	-	1200-1400
Fe, 5% B, 3% Si	20	1200-1400
Fe, 4% C, 1% Si, 1%Mn	10-30	1200-1400
Fe, 0.1% C, 1% Si, 1%Mn	40	1550-1600

indication of orifice deterioration, which in the extreme case, led to random oscillations and a complete loss of reference baseline It was found possible to condition the orifice in this steel by passing a high current (150-200 Amps) momentarily, to "clean" the BN orifice and restore a steady baseline, for further measurements.

When a sudden shift in the reference baseline occurred, the high pass filter of the differential preamplifier, operating in the AC mode, restored this shift to its original zero value by "bleeding" the input capacitors to their ground state through resistors, so that new differential pulses could be acquired. The rate of restoration depended on the filter setting, whose time constant was given by the product of R C in Fig. 4. This filtering action also caused a predictable loss in the magnitude of the recorded resistive pulses, as well as the negative backshoot following the original pulse in Fig. 3A.

Unexpectedly, sampling tubes made of fused silica glass retained their form up to 1500°C, and were used in this steel, in a temperature range of 1200-1400°C, Fig. 5. A fluted orifice with a glazed surface was produced on the side of a tube by first drilling a larger hole, and then heating this area to locally soften the silica glass, thereby causing it to flow, so as to minimize its surface energy by rounding off the sharp edges. This was continued until desired shape and size of orifice was obtained

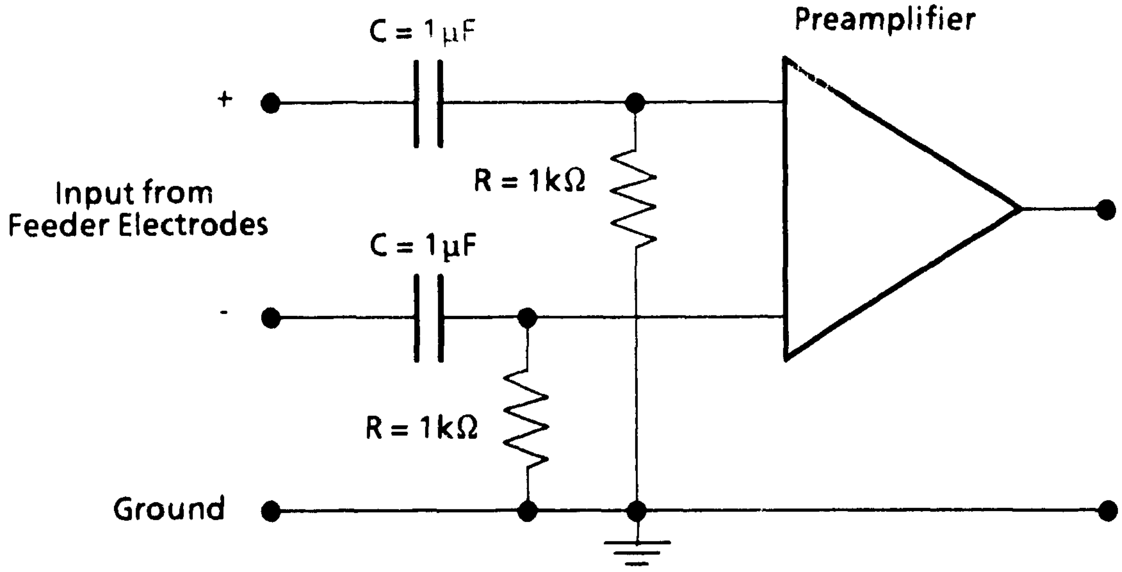

Fig. 4: Schematic of a high pass filter set at $RC = 1$ ms [2].

Orifices produced in this way had a particularly good performance. Orifice deterioration was reduced, baseline stability was maintained for a longer period, and the overall performance, as measured by the number of resistive pulses of correct shape and duration vs. other disturbances, on the baseline was comparable to that of the LiMCA borosilicate probes in used aluminum melts, i.e. >95% resistive pulses [2]. However, with some probes, double pulses of the type shown in Fig. 6, and asymmetric pulses, shown in Fig. 7 were obtained with an associated rise in high frequency background noise, and a decline in baseline stability. When orifices were sectioned in a plane passing through their longitudinal axis, some were found to have a humped profile, Fig. 8A. This was possibly because of material moved from the center of the orifice at the early stages of softening. The desirable fluted profile was then obtained by drilling a larger hole and heat shrinking a greater area, Fig. 8B. It was found possible to heat shrink holes of up to 600 μm in diameter in a 1.5 mm thick silica glass, holes greater than this tended to expand.

Figure 9 shows a resistive voltage pulse typical in this steel, obtained with a well functioning orifice in a quartz glass sampling tube. Dimensional stability of such

Fig. 5: LiMCA probe design with silica glass sampling tube and sensing zone, used in later experiments with boron - silicon steel melts.

orifices were good, as no measurable expansion was observed in orifice diameters after an experiment (see Fig. 10).

2.2 Comparative Inclusion Measurements in the Transformer Steel Alloy

2.2.1 Selection of Measurement Conditions

20 kg of molten alloy was prepared in an induction furnace and LiMCA measurements were made with the furnace power switched off, during cooling from

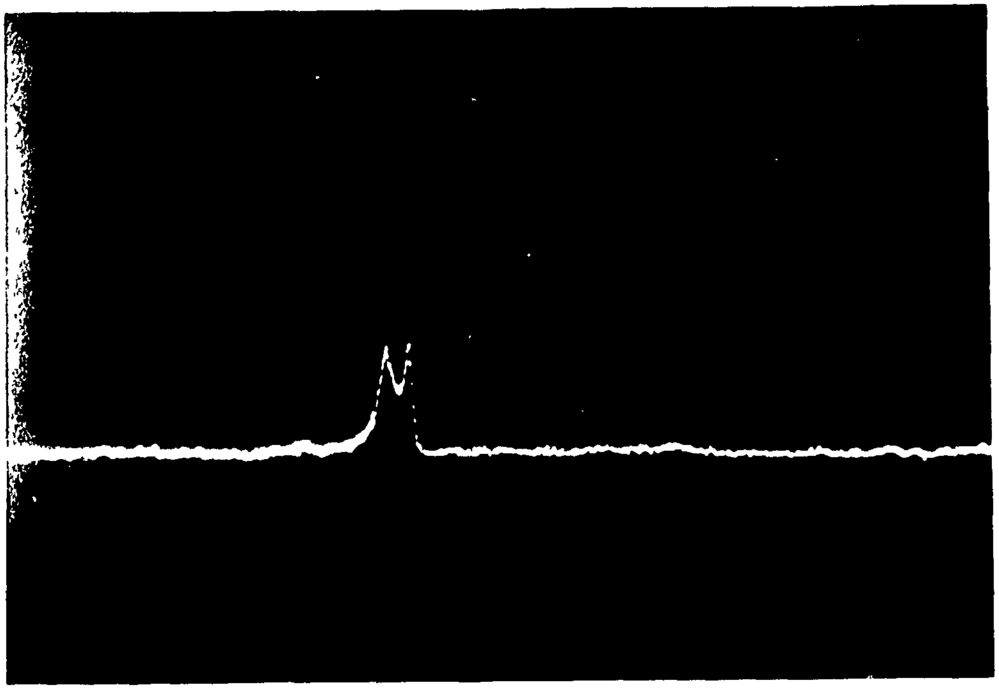

Fig. 6: Double pulse generated in a silica glass orifice.

1400°C to 1200°C. A heavy coat of ceramic fiber blanket was laid next to the water-cooled copper inductor and the bottom of the furnace, for insulation, to minimize heat losses from the crucible. Sand was packed betwen the crucible and the insulation to provide the necessary rigidity for the crucible, to prevent cracks developing during melting. This insulation provided a 20 minute working time for LiMCA measurements.

In order to detect a significant number of borosilicate inclusions within a typical liquid sample in this melt, and inclusion sizes being so small, it was found necessary to reduce the orifice diameter to 200 µm or less. No special problems were encountered in aspirating this steel through such a fine opening, an aspiration vacuum of 24 cm Hg (32 kPa), corresponding to 85% of the theoretical pressure difference, calculated for a completely non-wetting orifice (γ_{Fe} = 1 87 N/m [3]), was sufficient for overcoming surface tension effects and drawing the steel into the sampling tube.

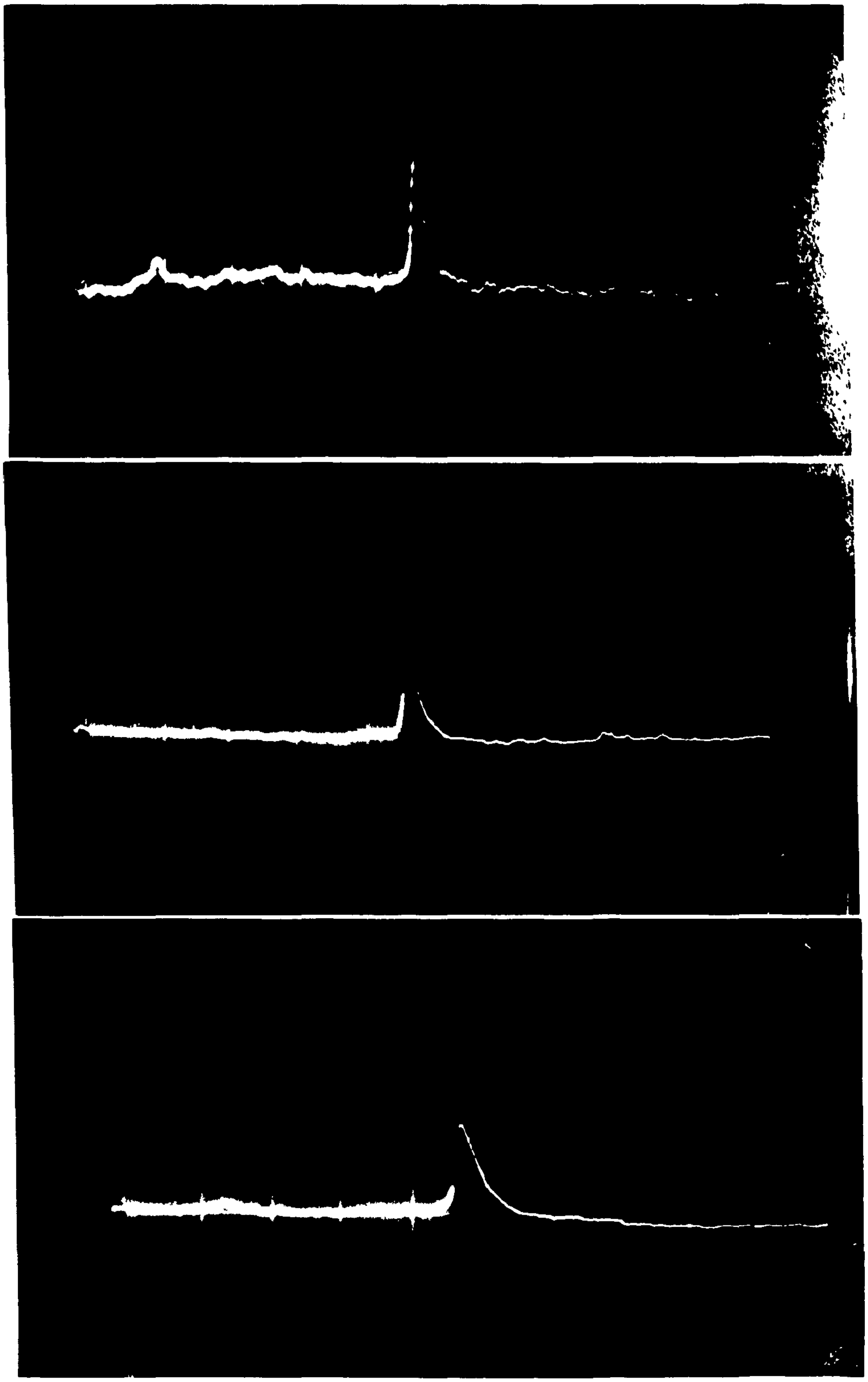

Fig. 7: Asymmetric pulses generated in a silica glass orifice As the sharp edge of the orifice rounded off, the apeces of the signals became less sharp and baseline stability improved.

Vertical displacement: 50 µV/div , time axis: 1 ms/div.

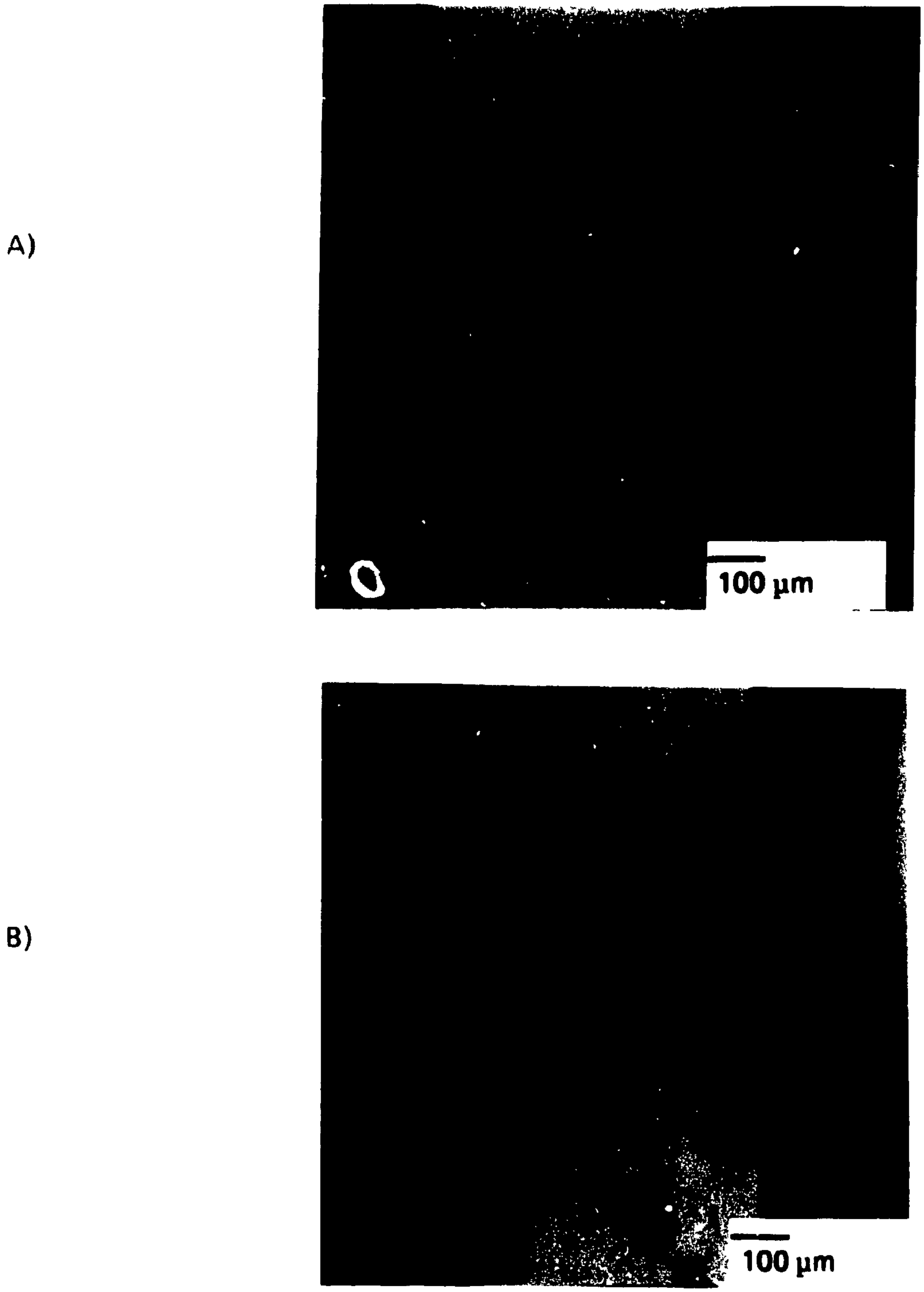

Fig. 8. Orifices set in silica glass, sectioned in a plane passing through their central axes. A microflame was applied to their left side. (A) humped profile resulted from inadequate heat shrinking, (B) fluted profile obtained by heat shrinking a larger, initial diameter.

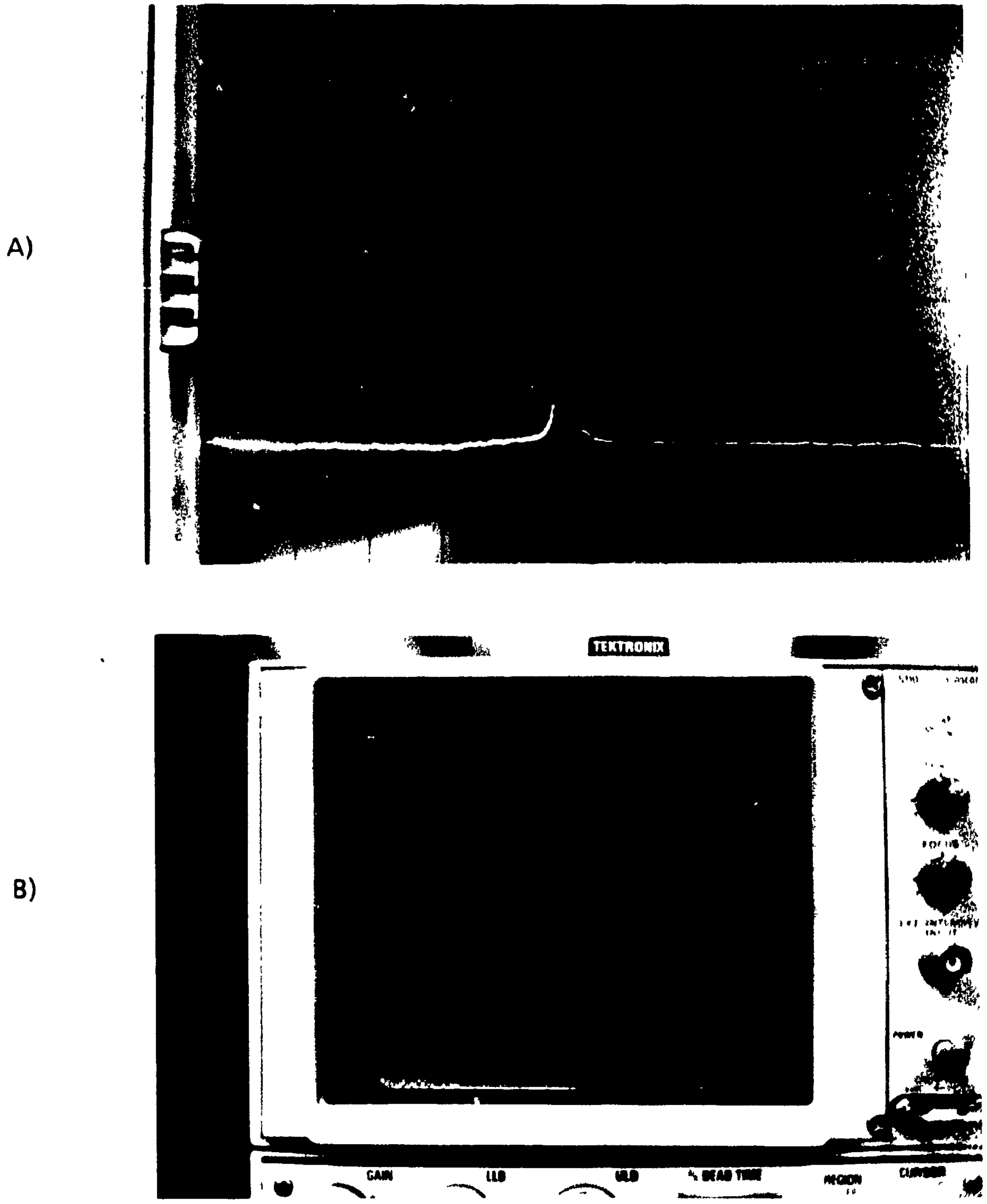

Fig. 9: Resistive voltage pulse obtained in a transformer steel melt using a silica glass sampling tube with a well functioning orifice (A), and the accompanying pulse height distribution in an M.C.A., accumulated over a 10 s data acquisition period (B).

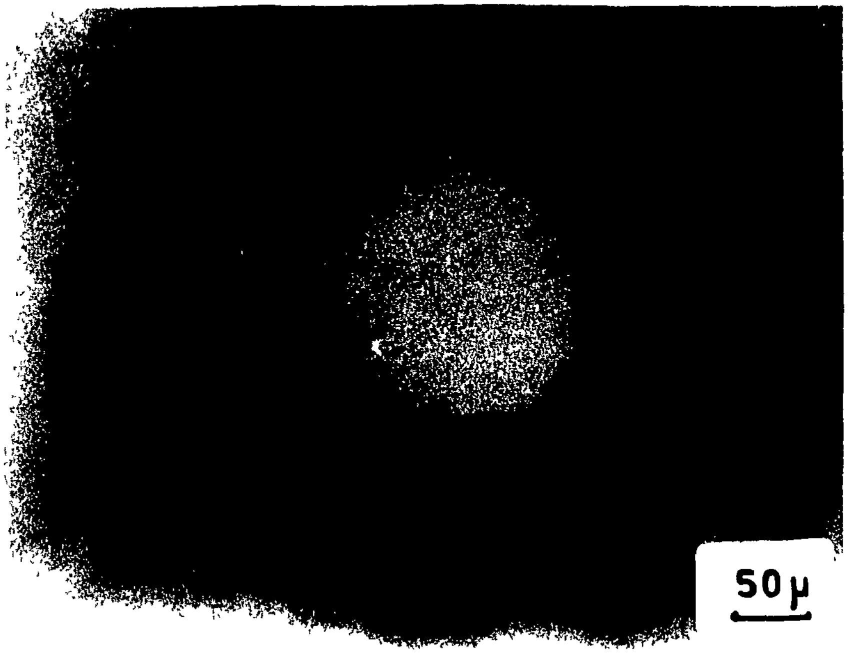

Fig. 10: Stability of a 260 μm orifice set in silica glass. No measurable expansion in orifice diameter was observed.

Operating currents for measurements were evaluated on the basis that excessive thermal load should not be placed on the orifice. Rate of metal temperature rise due to resistance heating at the orifice (in the absence of heat losses), is given by:

$$\frac{dT}{dt} = \frac{\rho_e i^2}{\rho C_p} \tag{1}$$

where the numerator is the volumetric rate of heat evolved according to Ohm's law, and the denominator is the volumetric heat capacity of the molten metal. Taking a typical LiMCA operation in aluminum melts with a 300 μm diameter orifice and a 60 Ampere operating current as an arbitrary standard, required currents were calculated for steel melts that yielded similar rates of temperature rise. Table 2 compares operating currents for a given size orifice, along with other computed values, for aluminum and steel melts.

Table 2. Operating currents for LiMCA in aluminum and steel melts.

Melt	D, µm	I, Amp.	$\rho_e I^2$, W/mm³	ρC_P, J/mm³ °C	dT/dt, °C/ms
Aluminum	300	60	180	$2.6 \cdot 10^{-3}$	70
Steel	200	20	570	$5.6 \cdot 10^{-3}$	100
Steel	100	5	"	"	"

For molten steel, $\rho_e = 1\ 4\ \mu\Omega$ m, $\rho = 7000$ kg/m³ [3], and $C_P = 0\ 8$ J/g [4]

Sample volumes were estimated from the known data acquisition periods during sampling and the applied vacuum, using the following relations:

$$V = \bar{u}\ A\,\Delta t; \qquad \bar{u} = C_D \sqrt{\frac{2\,\Delta P}{\rho}}\ ; \qquad C_D = a + b\,[Re] \mp \varepsilon_{0\,95} \tag{2-4}$$

where V: sample volume, $\bar{u}$: mean metal velocity at the orifice, Δt: data acquisition period, C_D: discharge coefficient. Linear relationship betwen the discharge coefficient and the Reynolds number *[Re]* in eqn. (4) was shown to hold for liquid zinc, using a similar sampling tube and orifice [5] From the data obtained, the coefficients a, b, and the 95% confidence interval for C_D, $\pm\varepsilon_{0\,95}$, were deduced These results are summarized in Table 3. Such linear relationships between Reynolds number and the entry and exit losses have been predicted theoretically and observed experimentally for laminar flow in pipes [6] Since zinc and steel have similar densities, the same coefficients were used to estimate the volumes of samples taken by LiMCA in steel melts.

2.2.2 Comparative Measurements

Figure 9B provides a typical histogram of the resistive pulses recorded by the Multi Channel Analyser (M.C.A.) for a 200 µm orifice, and accumulated over a 10 s data acquisition period. For the inductively stirred melts, few large inclusions (>10 µm) were detected. A threshold voltage of 20 µV, above which particles were counted, corresponds to the brighter points to the right of the first major division. Such histograms were then converted into hatched size distribution charts of the

Table 3. Relationship between discharge coefficient and Reynold's number in a LiMCA orifice, using molten zinc.

ΔP, cm Hg	$\bar{u}$, m/s	[Re]	C_D
6	1.05	525	0.67
8	1.20	600	0.66
10	1.42	700	0.70
12	1.60	800	0.72
16	1.98	990	0.77
20	2.24	1120	0.78

$\hat{C}_D = a + b[Re] \pm \varepsilon_{0.95}$, correlation coeff., $r = 0.98$

$a = 0.2 \cdot 10^{-3}$, $b = 0.55$, $\varepsilon_{0.95} = 62 \cdot 10^{-6} \{ ([Re] - 791)^2 + 43\,620 \}^{\frac{1}{2}}$

from $\varepsilon_{1-\alpha} = t_{\alpha/2,(n-2)} s_{xy} \{(x-\bar{x})^2 / S_{xx} + 1/n\}^{\frac{1}{2}}$ [7]

type shown in Fig. 14. As the bar chart shows, no particles greater than 25 µm were detected within the 4.7 g portion of the melt sampled.

Figure 11A shows a typical random area in the microstructure of this steel where many small inclusions (borosilicates) of about 1-3 µm are present. The very few larger inclusions were found after checking many fields of view: Fig. 11B shows one such large spherical inclusion, measuring 7 µm in diameter.

A 0.1% aluminum addition was then made to this inductively stirred melt, and ten minutes later the melt quality again recorded (see distribution B in Fig. 14). Since the 210 µm orifice of the sampling tube had blocked, the second sampling was carried out using a back-up sampling tube containing a 370 µm orifice.

The corresponding micrograph from a quenched sample, is shown in Fig. 12A where addition of aluminum leads to larger, less spherically shaped inclusions of aluminum borosilicate, indicating a change in their melting point. Larger inclusions were more frequent; one such inclusion is shown in Fig. 12B. It is believed that dissolved aluminum diffuses into molten borosilicate inclusions, changing their chemistry and causing growth largely by way of coagulation. Figure 13 shows, on its left, an electron microprobe image of a cluster of inclusions following an addition of aluminum, and on its right, its associated X-ray map for aluminum. The latter shows aluminum clearly incorporated within the oxide inclusions.

Each field of view in Figs. 11 and 12 represents 0 01 mm^2 of surface area Such randomly selected fields from both samples were subjected to manual image analysis (Mrs. G. Cheng). The resulting inclusion size distributions are shown in Figure 15. The difference in size distributions obtained by the image analysis and the LiMCA probe reflect the importance of sample size in obtaining the right hand tail of an inclusion size distribution curve. Figure 16 shows the sample sizes that can be obtained by LiMCA during a 10 s data acquisition period, in terms of both weight of steel sampled and the equivalent surface area to be examined microscopically. The latter is calculated by assuming that the sample volume is equal to the product of the sample area and the minimum detectable inclusion size. In Figure 14, although 57 inclusions greater than 10.4 µm were counted in a 4.7 g steel sample; one can readily deduce that there would have to be, on average, only one such corresponding inclusion per 10 cm^2 of steel surface, far greater than the surface area actually analysed.

Interestingly, although the dissolved oxygen content, as measured by an oxygen analyzer (Electronite, Celox 2 probe) decreased from 3 ppm to practically zero following the 0.1% aluminum addition, total oxygen contents, as measured from solid samples with a Leco oxygen analyser, remained the same, at about 80 ppm. This showed that there was no significant change in the volume fraction of oxide inclusions between the two melts.

A simple mass balance calculation indicates that less than 1% of this oxygen is contained within the inclusions measured, i.e. greater than 10 µm in diameter The population density of smaller inclusions, say with a median size of 1-3 µm, would need to be in the order of 2-3 million per gram of steel to make up the balance of oxygen. Indeed, the population density of such inclusions in the Figs 11 and 12 is very high, and more accurate measurements made on a volume basis, utilising inclusion extraction techniques from solid steel samples and Coulter Counter measurements in aqueous electrolytes also confirm large numbers of small inclusions [8].

Figure 17 illustrates another test on boron steel, in which the number density of borosilicate inclusions within the melt following melt down in an inductively stirred furnace, was raised by passing air through the melt for one minute, at a flowrate of 4 Nl/min. As seen, further oxidation of boron and silicon lead to an increase in the number of particles in all size ranges, with a shift towards larger inclusions

The smallest orifice size used with the present E.S.Z. instrument for this alloy steel was 120 µm. The melt was sampled under a current of 5 Amperes yielding a calculated detection limit of 7.8 µm The inclusion distribution measured is shown in Fig. 18. The orifice size being smaller, the detection limit was lowered, causing the resistive pulses to become larger. As there are many more smaller inclusions than the larger ones, inclusion population density also rose sharply, apparent from the oscilloscope images shown in Fig. 19. For such settings, coincidence can be a problem The latter is a measure of the likelihood of two or more particles entering the sensing zone at the same time. Inclusion coincidence may cause an increase or a decrease in the true counts, depending on whether it is predominantly of a primary or of a secondary nature [1,9].

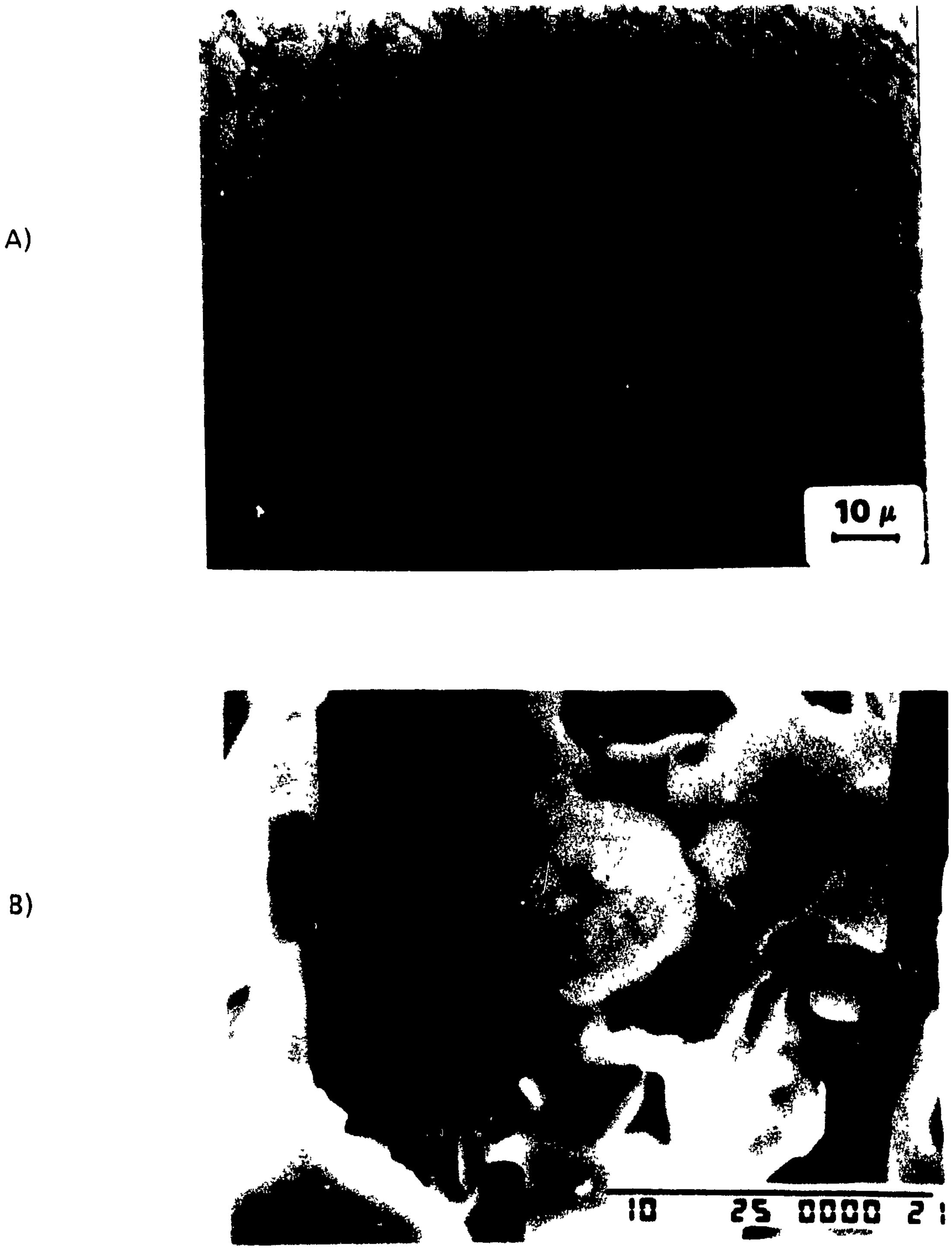

Fig. 11: Typical area (A), and a large spherical borosilicate inclusion (B), in the microstructure of 5% B, 3% Si, Fe steel.

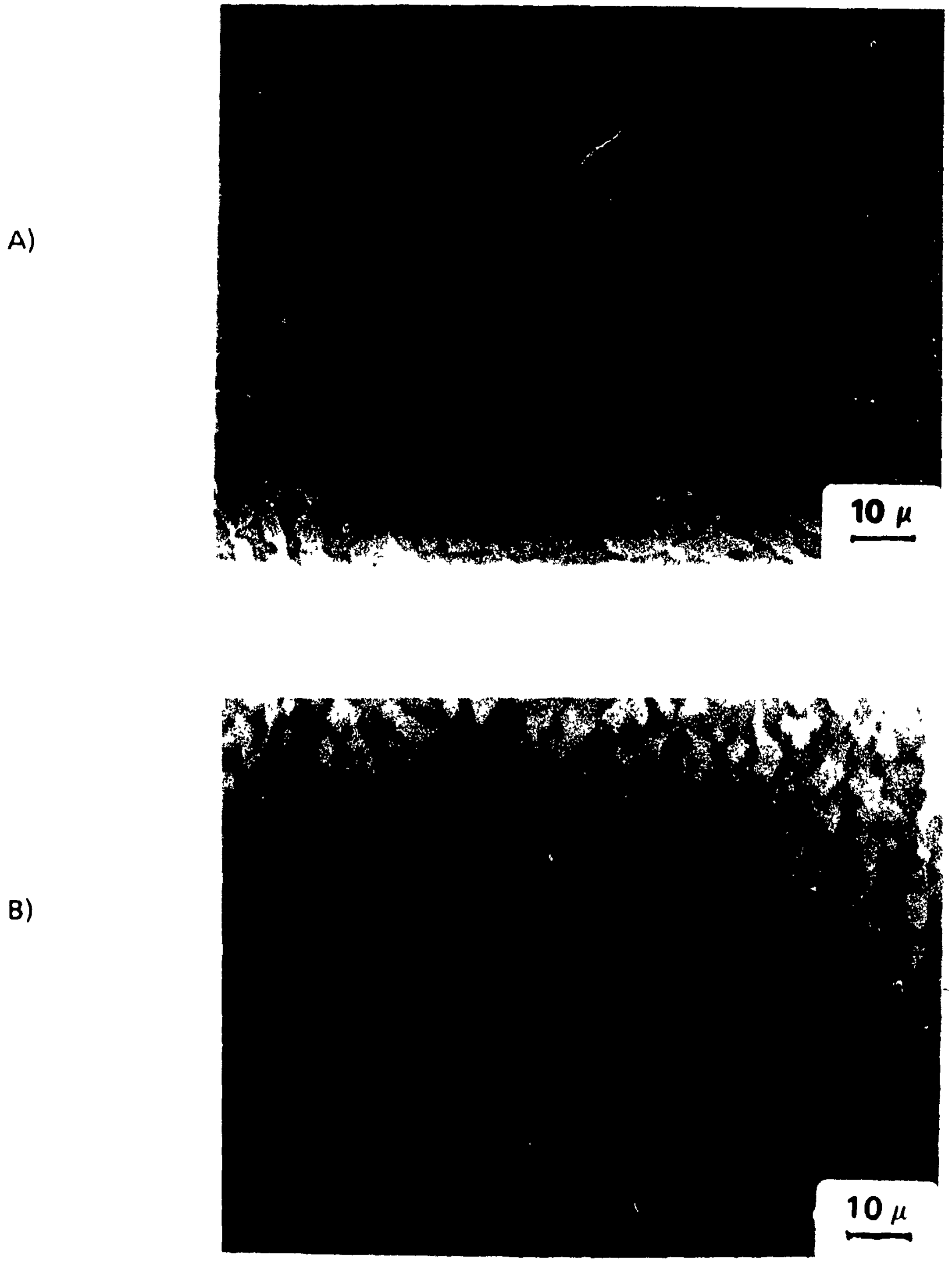

Fig. 12: Microstructure of the 5% B, 3% Si, Fe steel after 0.1% Al addition (A), and a larger inclusion in this microstructure (B).

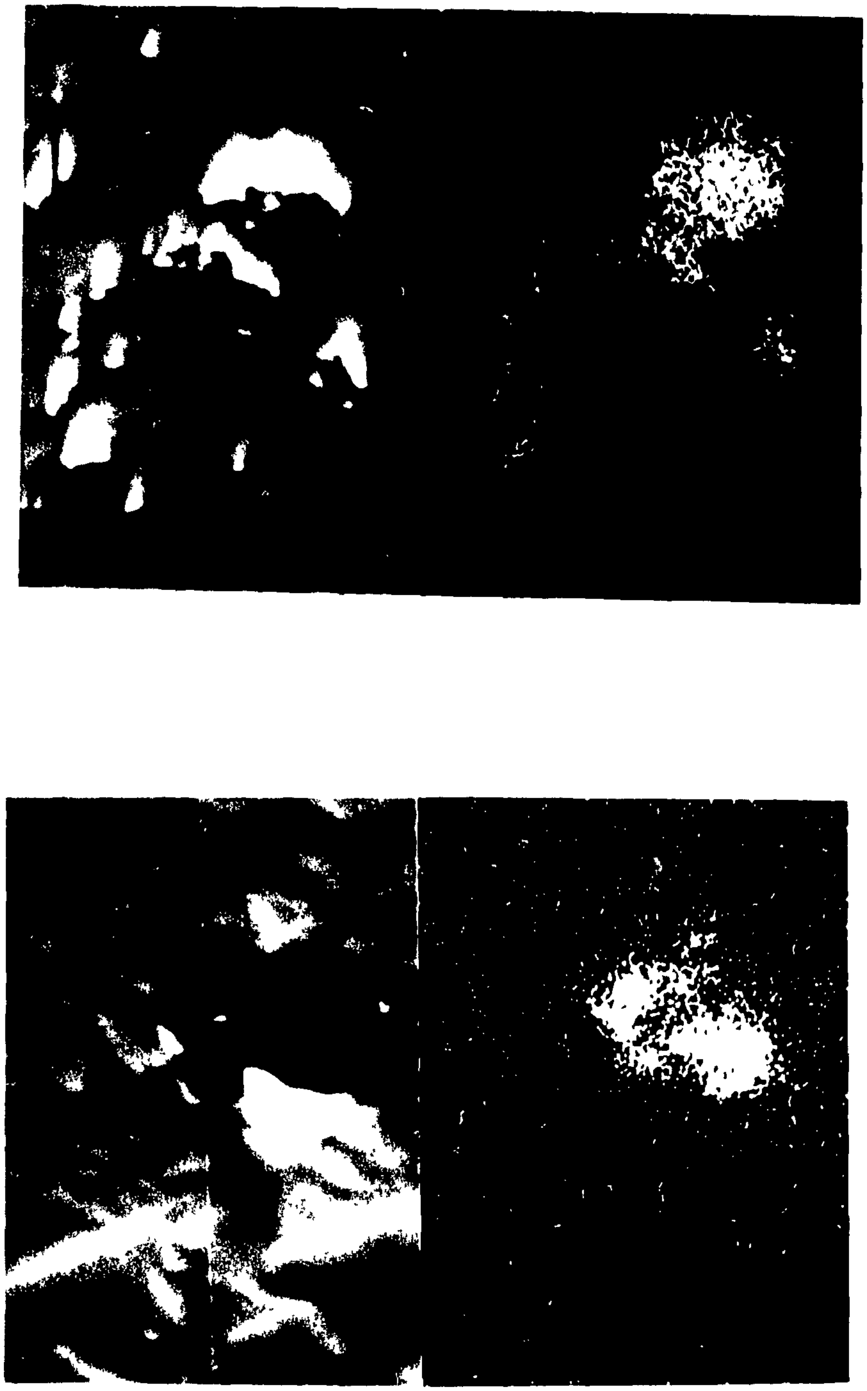

Fig. 13: Cluster of inclusions after 0.1% Al addition (L.H.S.) and their corresponding X-ray aluminum maps (R.H.S.).

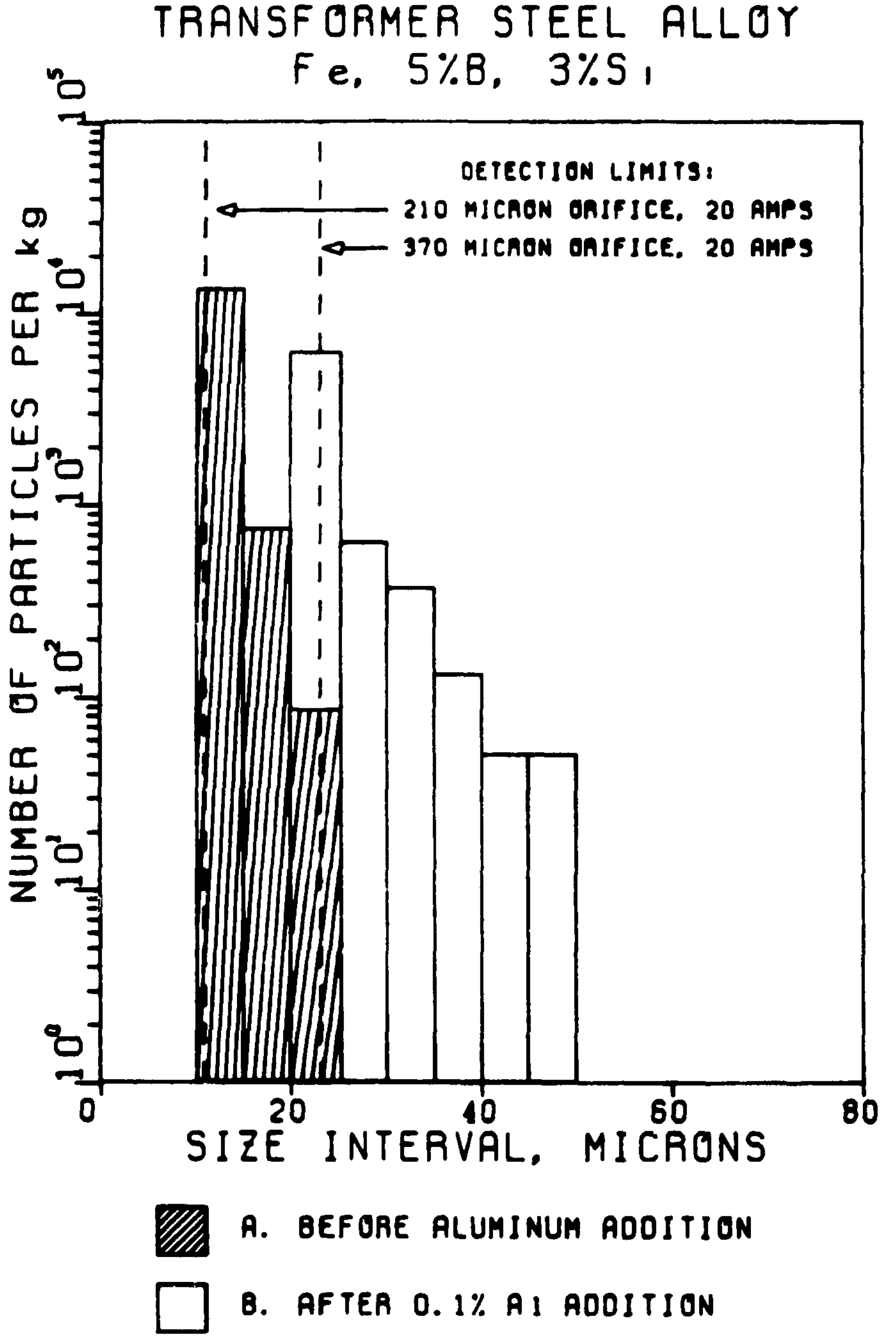

Fig. 14: Size distribution of inclusions in the transformer steel before, and following, a 0.1% Al addition to the melt.

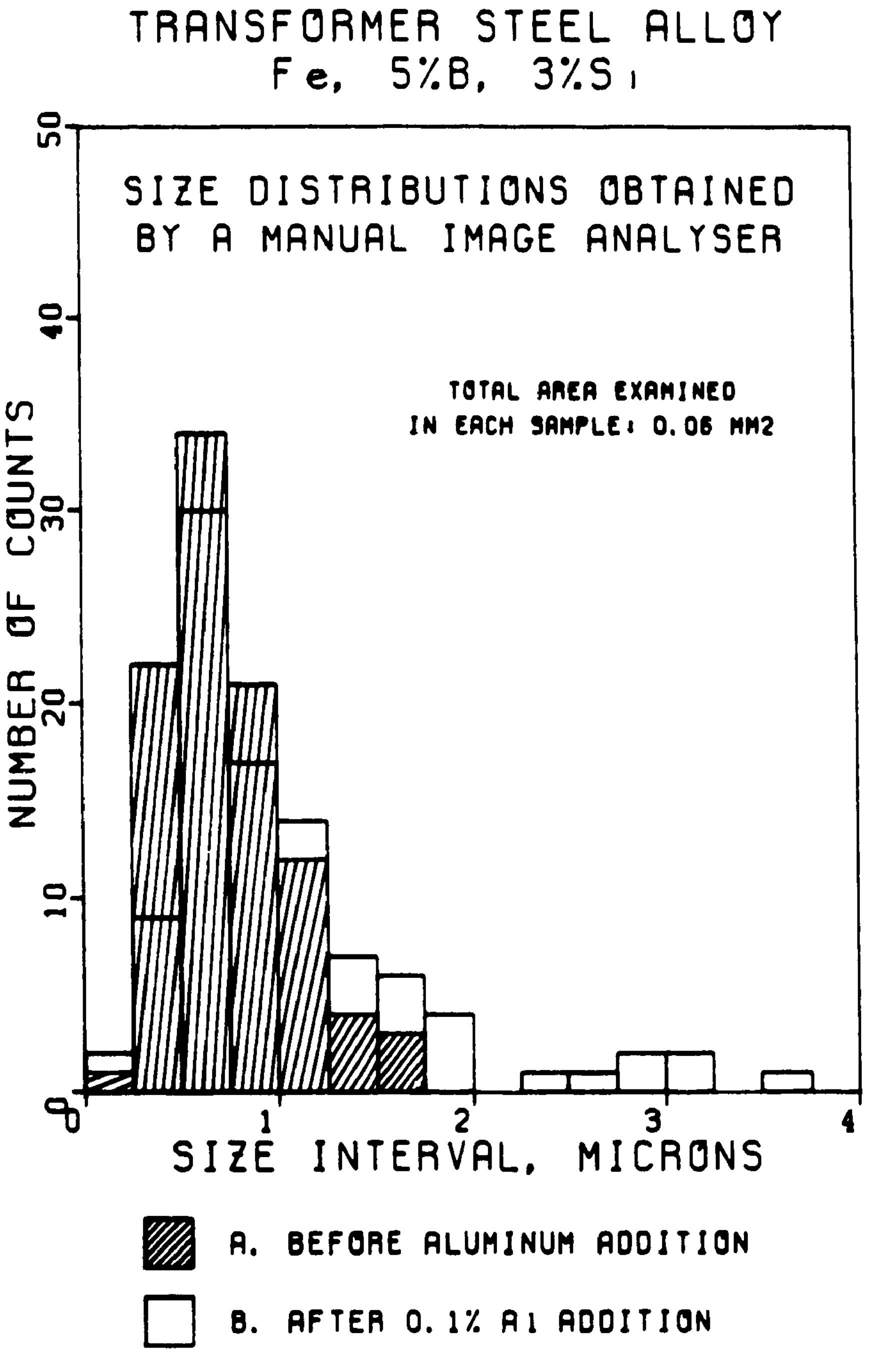

Fig. 15: Size distribution of inclusions obtained by subjecting random frames such as Figs. 11 and 12 to a manual image analyser

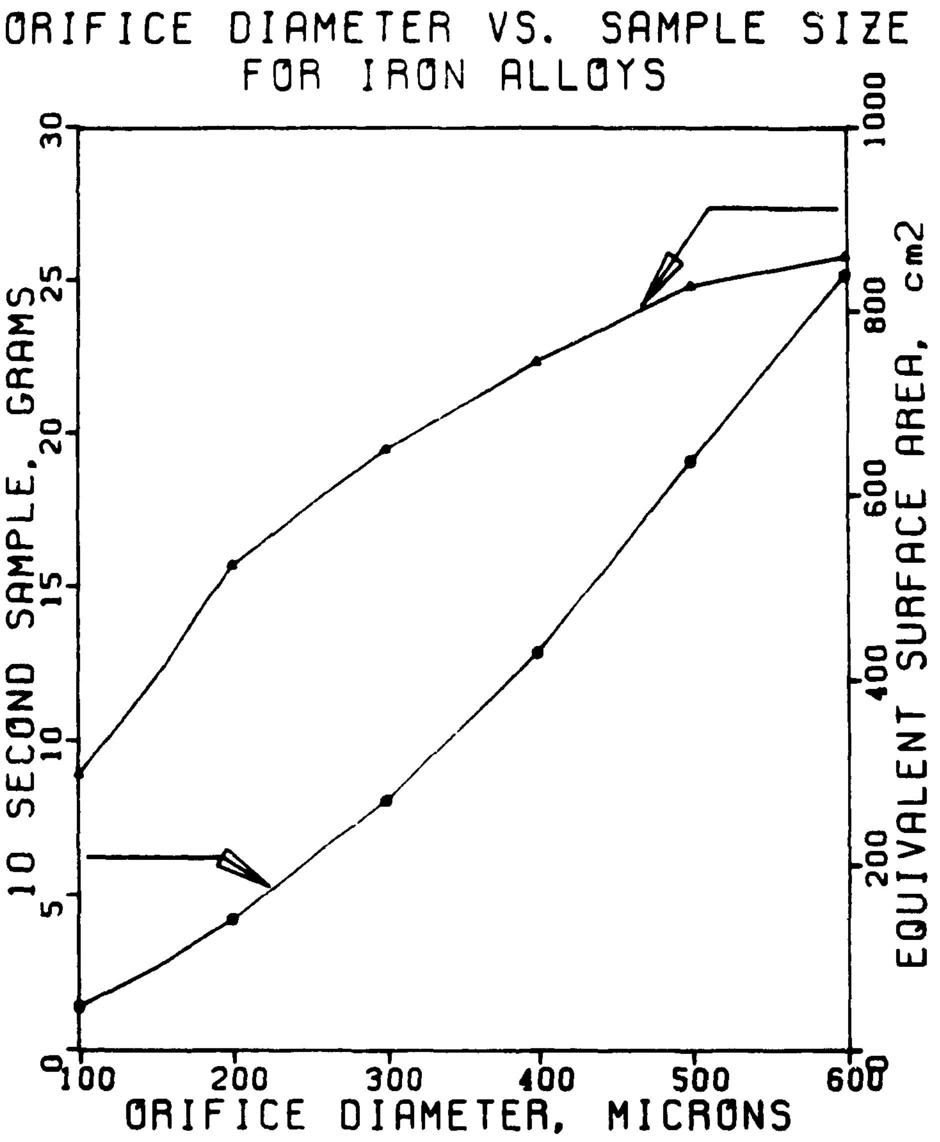

Fig. 16: Sample size obtained by LiMCA as a function of orifice diameter.

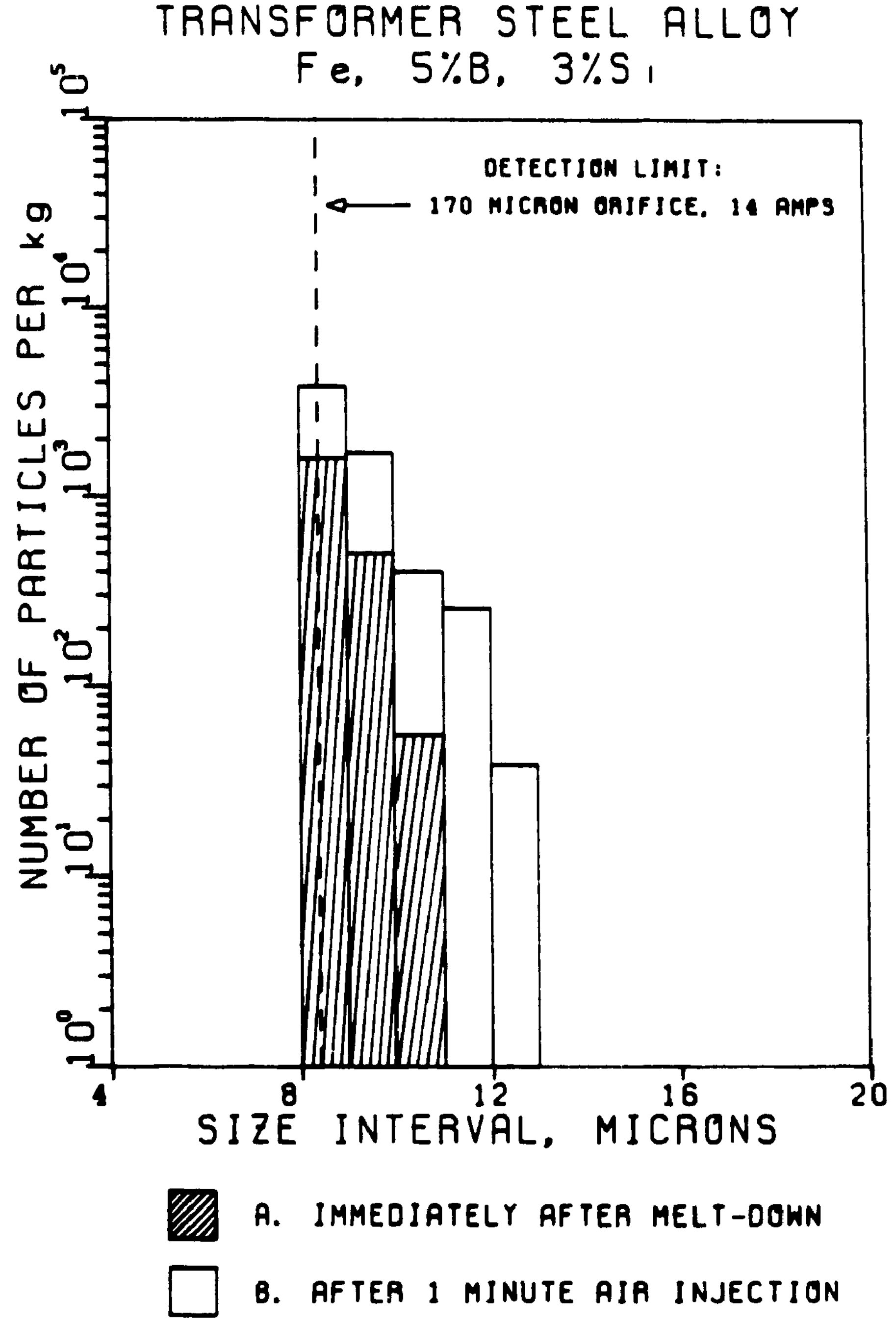

Fig. 17: Size distribution of inclusions immediately after melt-down, and following a one min. air injection at a rate of 4 ℓ/min, in a transformer steel melt

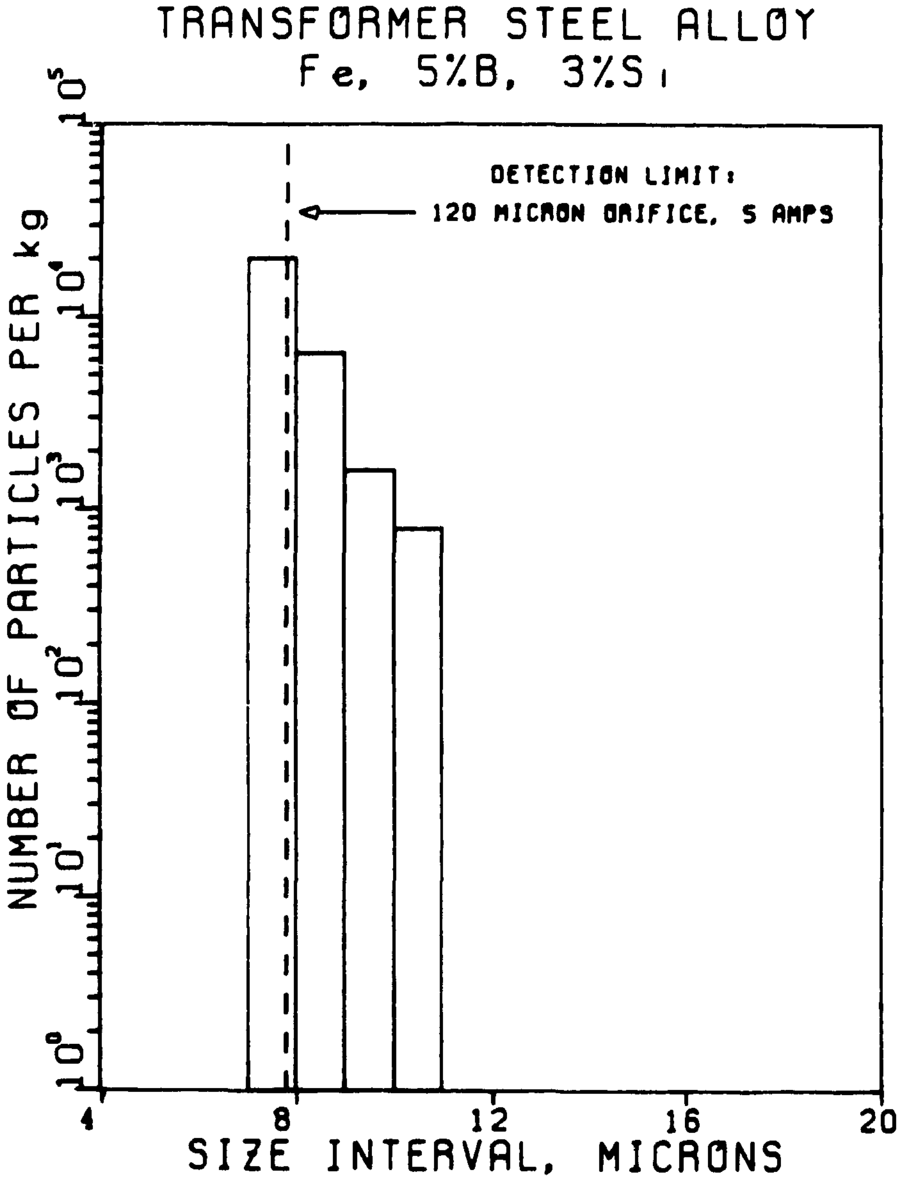

Fig. 18: Size distribution of inclusions detected in a transformer steel melt using a very small orifice (120 µm diameter).

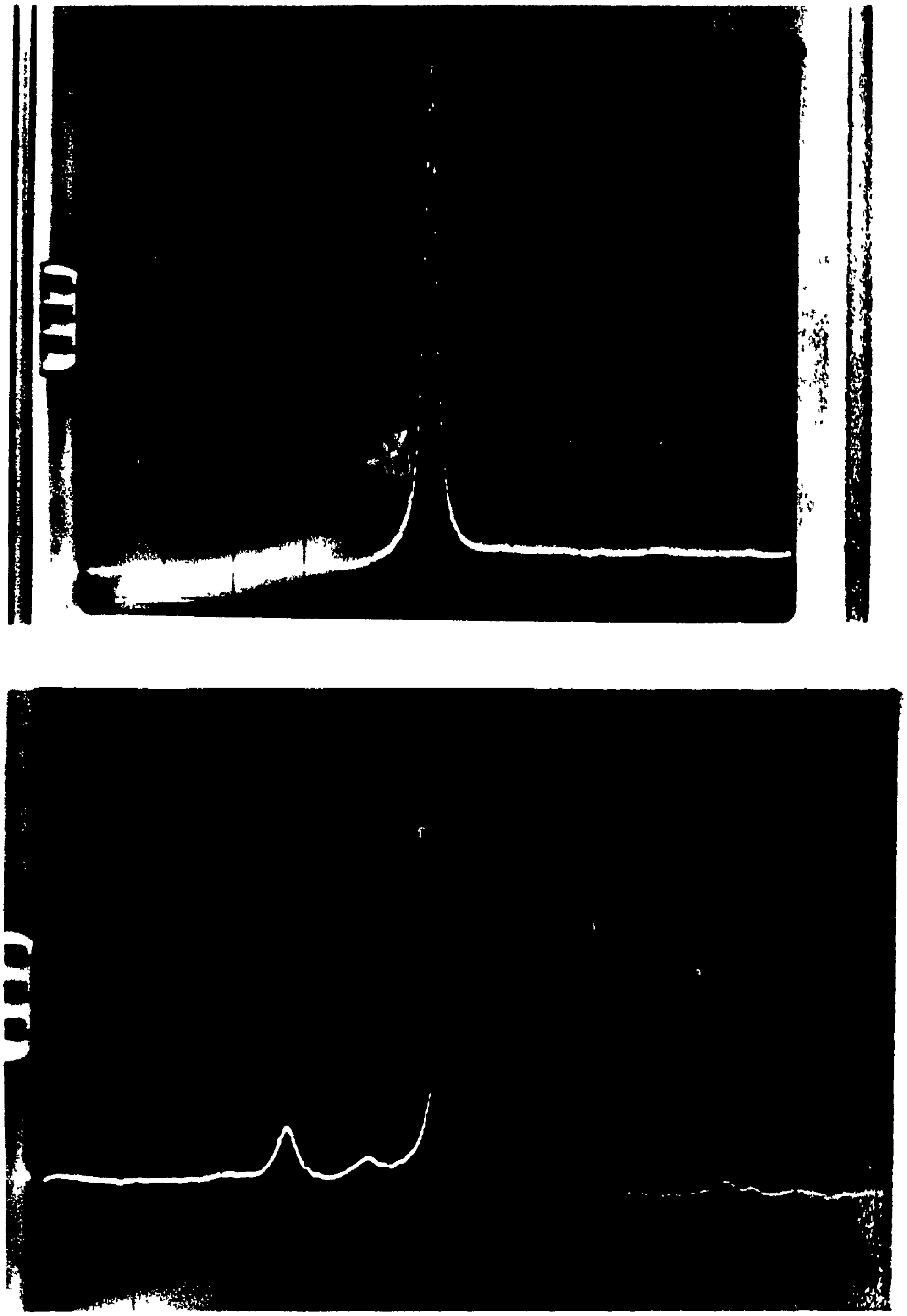

Fig. 19: Resistive voltage pulses recorded during LiMCA's operation with the 120 µm diameter orifice.
Vertical displacement: 50 µV/div., time axis 1 ms/div

3. EXPERIMENTS WITH CAST IRON

It was considered that cast iron represented another low temperature m.p. alloy where the probe described for Fe-Si-B alloys could be applied Other than an academic curiosity, such a probe could also serve to monitor non-metallic inclusion levels in inclusion sensitive cast irons In a newly developed Vacuum Assisted Casting (VAC) process for nodular cast iron, for instance, it has become possible to produce high strength, thin wall, light weight castings with high metal yield and near net shape (Fig 20) However, parts requiring fatigue strength, such as the connecting rods in car engines, became notch sensitive to inclusions when cast in thinner cross-sections. It was suggested that these inclusions had to be monitored, and when necessary, removed from the melt prior to casting, in order to take full advantage of the VAC's capability for producing thinner sections [10].

However, LiMCA probe experiments in cast iron met with difficulties. Using a 430 µm orifice, it was not even possible to pass a continuous current. Figure 21A shows rapidly rising voltages because of periodic disruptions in the current path at the orifice Cavitation because of CO formation at the orifice exit was ruled out, because the same discontinuities were observed when the sampling tube was under pressure, as well as under vacuum. Increasing dissolved silicon levels to 1% made the matter worse, causing a complete loss of current. Upon raising the orifice above the melt, it was observed to be physically blocked, molten metal trickling, rather than jetting out of the orifice, as would have been the case with a transformer steel melt. Larger orifices (*D*>1000 µm) did not block immediately, but still suffered from an eventual deterioration, as evidenced by disturbances and oscillations of the reference baseline voltage traces on the differential oscilloscope. Attempts to condition the orifice with a high current in cast iron did not help, but rather hindered, and resulted in a rapidly blocked orifice and loss of current.

Since borosilicate inclusions in the transformer steel melt were fluid, it was hypothesised that accumulation of solid inclusions at or around the orifice, were to blame. It was therefore decided to investigate the effect of liquifying silica inclusions by manganese additions, in order to prevent the orifice deterioration. The results obtained are summarized in Table 4.

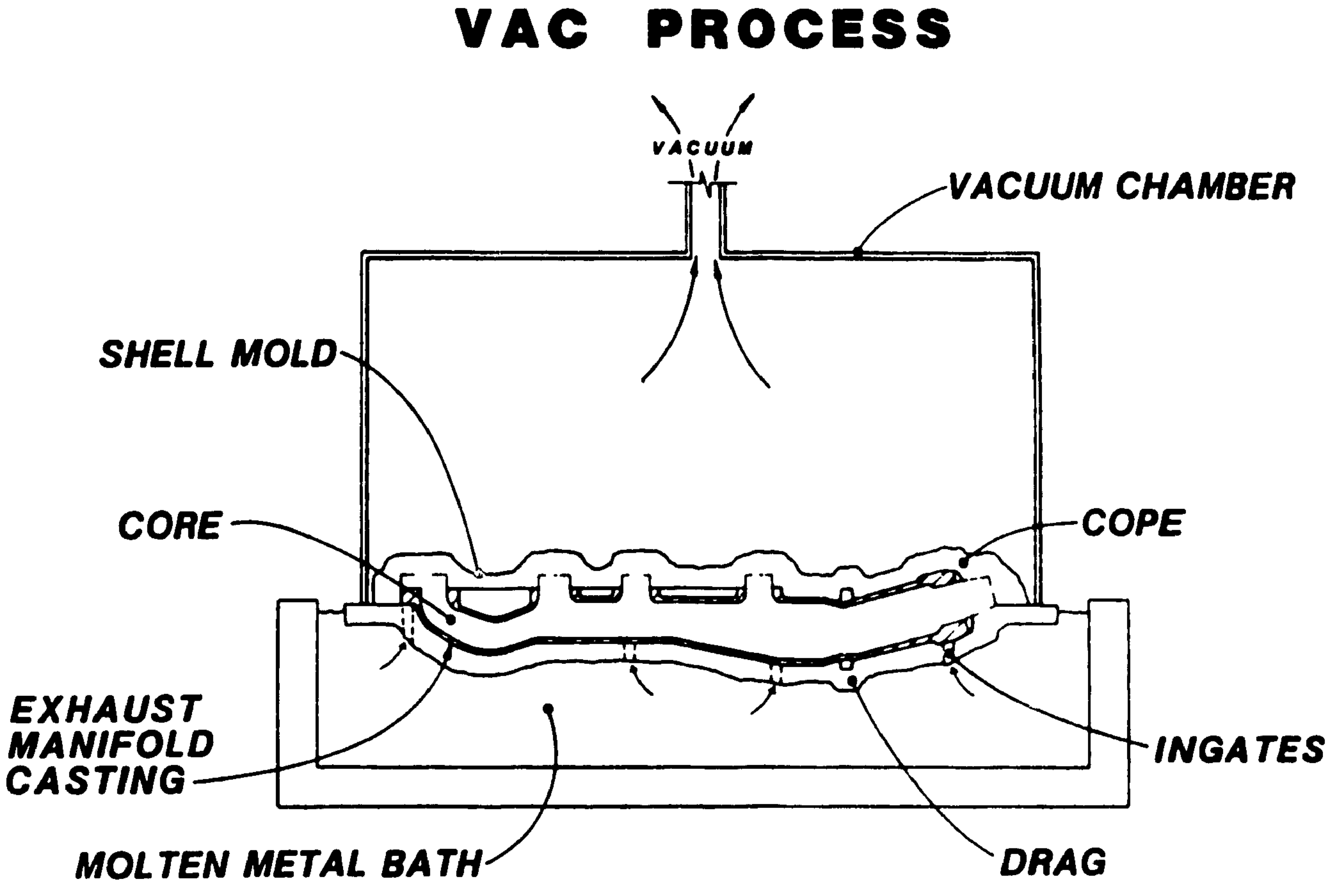

Fig. 20: Vacuum Assisted Casting (VAC) process for nodular iron, developed by G.M. Corp. A bonded sand mold is lowered into molten iron and vacuum is applied to degas and to draw metal into the casting cavity, for a high strength, thin wall, near net shape casting [10].

After having a 1% Si in the melt, increasing the manganese levels returned a steady current but baseline stability was not obtained (Fig 21B) Increasing manganese further, up to 4%, resulted in rapid orifice enlargement because of the interaction between manganese and silica glass to form lower melting point manganese silicates. The best operation for the silica probe was established at low silicon, high manganese levels, when resistive pulses caused by inclusions could be

Table 4. Summary of experiments in cast iron.

No	% Si	% Mn	Comments
1	0.25	0.015	melt down: 4.1-4.6% C, 0.012% S, 0.035% P Fig 21A
2	1	0.015	
3	1	0.5	
4	1	1.1	some current
5	1	2.2	steady current, Fig. 21B
6	1	3.3	
7	1	4.4	rapid orifice enlargement, D>1000 μm
8	0.65	0.015	
9	0.65	0.70	slag on melt surface became molten
10	0.65	1.4	best operation, Fig. 22
11	1.3	1.4	baseline stability was lost.

Chemical compositions were calculated from the ferroalloy additions made, assuming 100% recoveries. Spectral analysis for samples 6 and 7 were.

No	%Si	%Mn
6	0.66	3.2
7	0.69	4.4

N.B. Mn values (above 2%) were determined by extrapolation

observed, but baseline instability was still too high for meaningful measurements, Fig. 22.

Although some dissolved silicon was necessary to prevent the oxidation of carbon, high silicon levels led to rapid orifice deterioration and physical blockages. The possibility of silicon carbide precipitation causing apparent blockages according to:

$$\underline{Si}_{Fe} + \langle C \rangle \rightleftharpoons \langle SiC \rangle$$

was checked for thermodynamic possibility. Table 5 gives the thermodynamic data available for computation of this reaction's equilibrium constant. Taking

Table 5. Data used to compute the equilibrium constant K_4 between graphite, $\underline{Si}_{Fe}$ and SiC in cast iron [11].

i	Reaction	ΔG°_i, J/mol
1	$\langle Si \rangle + \langle C \rangle = \langle SiC \rangle$	-73 050 + 7.66 T
2	$\langle Si \rangle = \{Si\}$	+ 50 540 - 30.0 T
3	$\{Si\} = \underline{Si}_{Fe}$	-131 500 - 17 24 T
4	$\underline{Si}_{Fe} + \langle C \rangle = \langle SiC \rangle$	+ 7910 + 54.9 T

⟨solid⟩, {liquid}, pure component st state, $\underline{X} \equiv 1$ wt% st. state
$\Delta G^\circ_4 = -RT \ln K_4$, $K_4 = 1/h_{Si}$

Table 6. Initial composition of cast iron and the interaction coefficients of silicon used in calculating the equilibrium silicon composition in K_4 [12].

	C	Si	Mn	S	P
%	4.1-4 6	0.25	0.015	0.012	0.035
e_{Si}	0.24	0 1	0.28	0 06	0.09

also see Table 12 for references on interaction coefficients

$a_{SiC} = a_C = 1$, and using the interaction coefficients for silicon in Table 6, the corresponding silicon compositions needed for SiC precipitation were calculated for 1200°C and 1400°C, respectively:

Temp., °C	log K_4	h_{Si}	% Si
1200	-3.18	1515	10.8
1400	-3.15	1410	10.6

Owing to a large positive deviation from Henry's law, equilibrium silicon concentrations were much smaller than their corresponding activity values The computations indicate that greater than 10% Si would be necessary to precipitate SiC. The margin of error is expected to be high for this computation, since apart from the uncertainties in interaction coefficients, the solution was no longer dilute in C and Si. Nevertheless, these results indicate that the formation of SiC would be unlikely.

Since silicon raises the activity of carbon, it might also have caused carbon to exceed its saturation limit and precipitate as graphite flakes from cast iron. Figure 23 compares equilibrium diagrams for Fe-C binary and the Fe-C pseudo binary in the presence of 2% Si As seen, the stability of the mushy zone containing graphite is moved towards lower carbon contents and higher temperatures at higher silicon levels

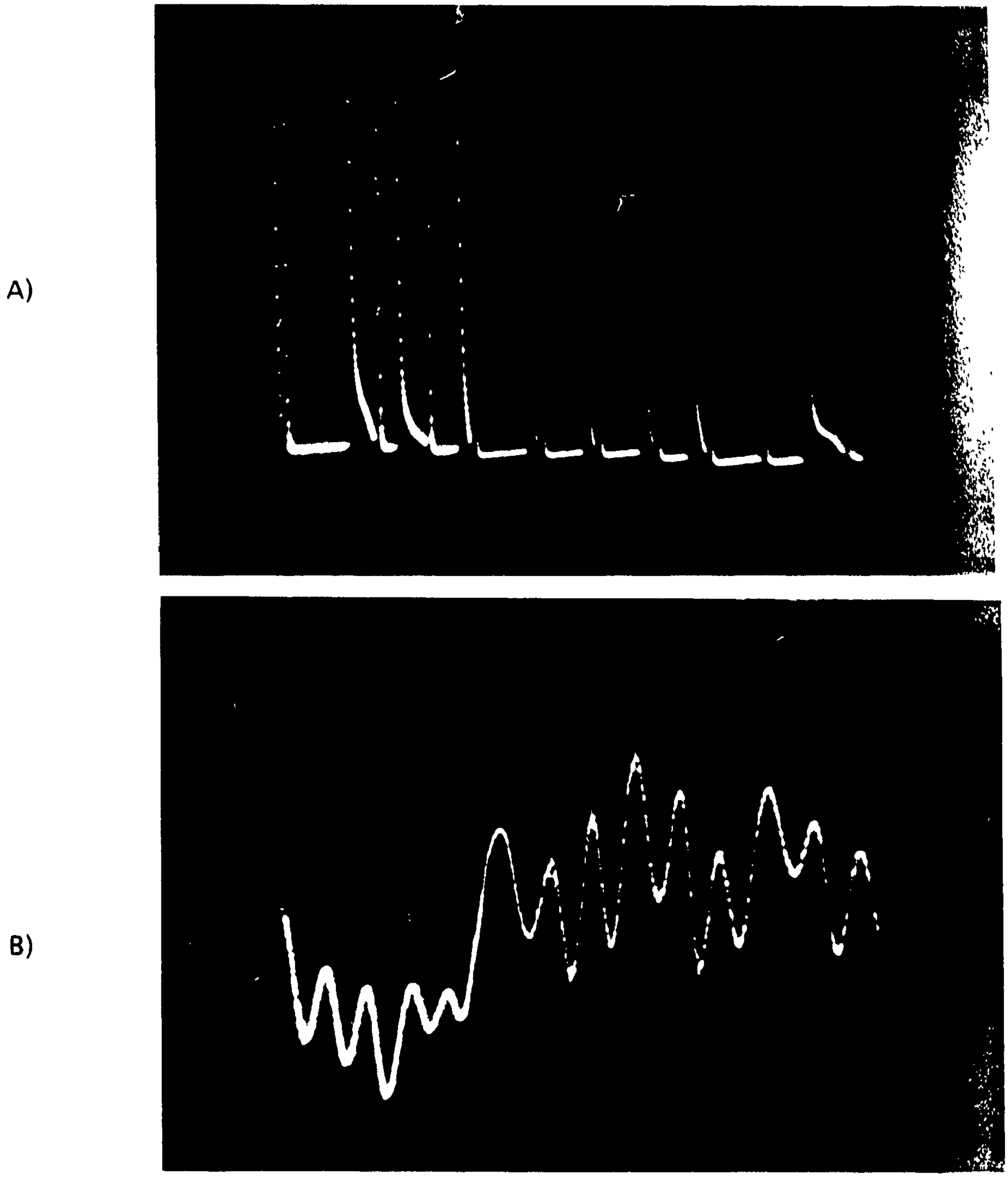

Fig. 21: (A) Discontinuities observed in the transient voltage across an orifice ΔV_{AB} in cast iron. When the orifice becomes insulating, the potential drop across the orifice approaches 6 Volts (battery e.m.f.), hence the spikes. Circuit current dropped to few Amps from an expected value of 40 Amps.

Vertical displacement: 5 mV/div, time axis: 10 ms/div

(B) Oscillations on the reference baseline after Si and Mn additions into cast iron. Circuit current was maintained at 40 Amps.

Vertical displacement: 50 µV/div, time axis: 1 ms/div

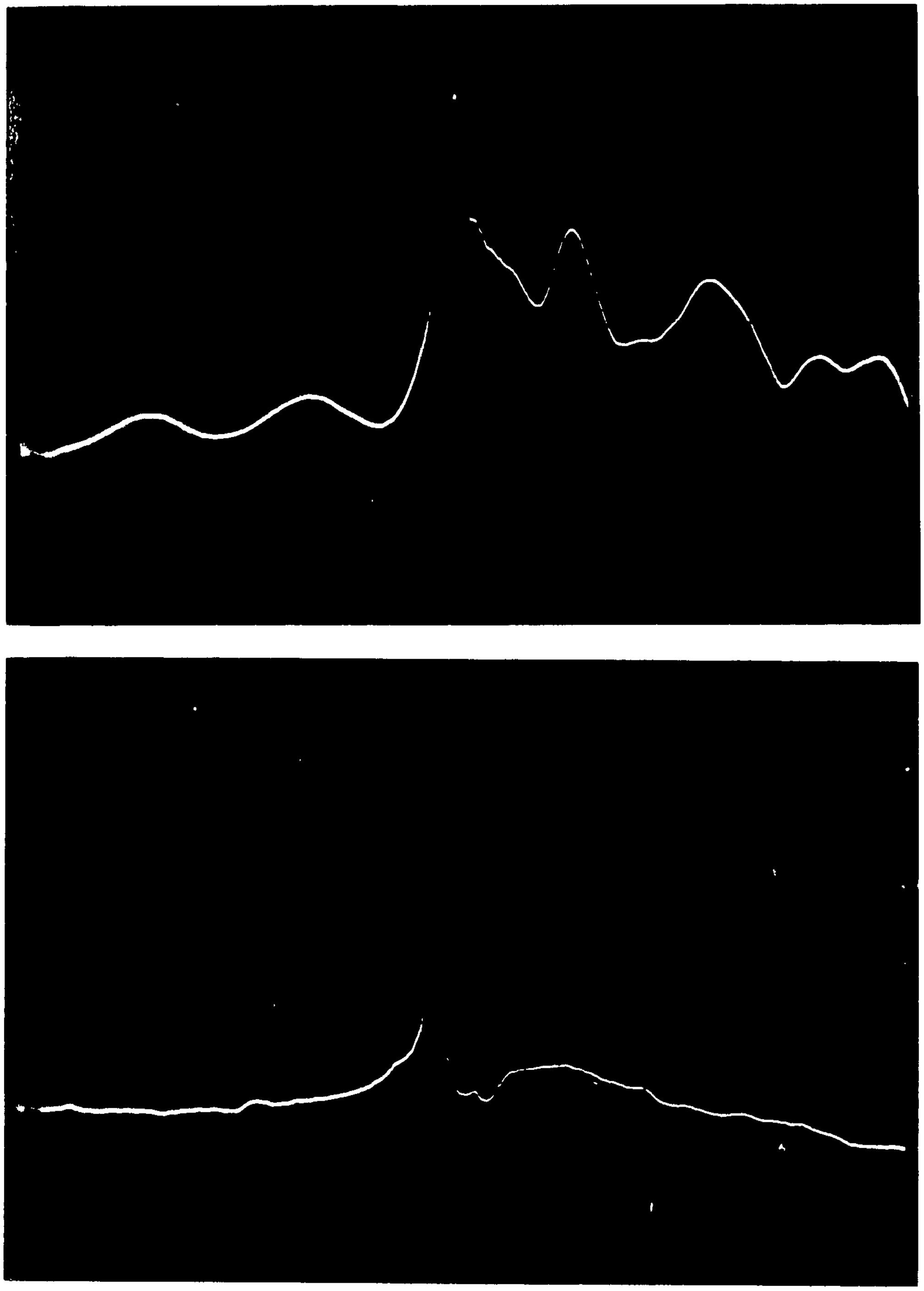

Fig. 22: Resistive voltage pulses obtained in low Si, high Mn cast iron with accompanying instability.
Vertical displacement: 50 µV/div., time axis: 1 ms/div.

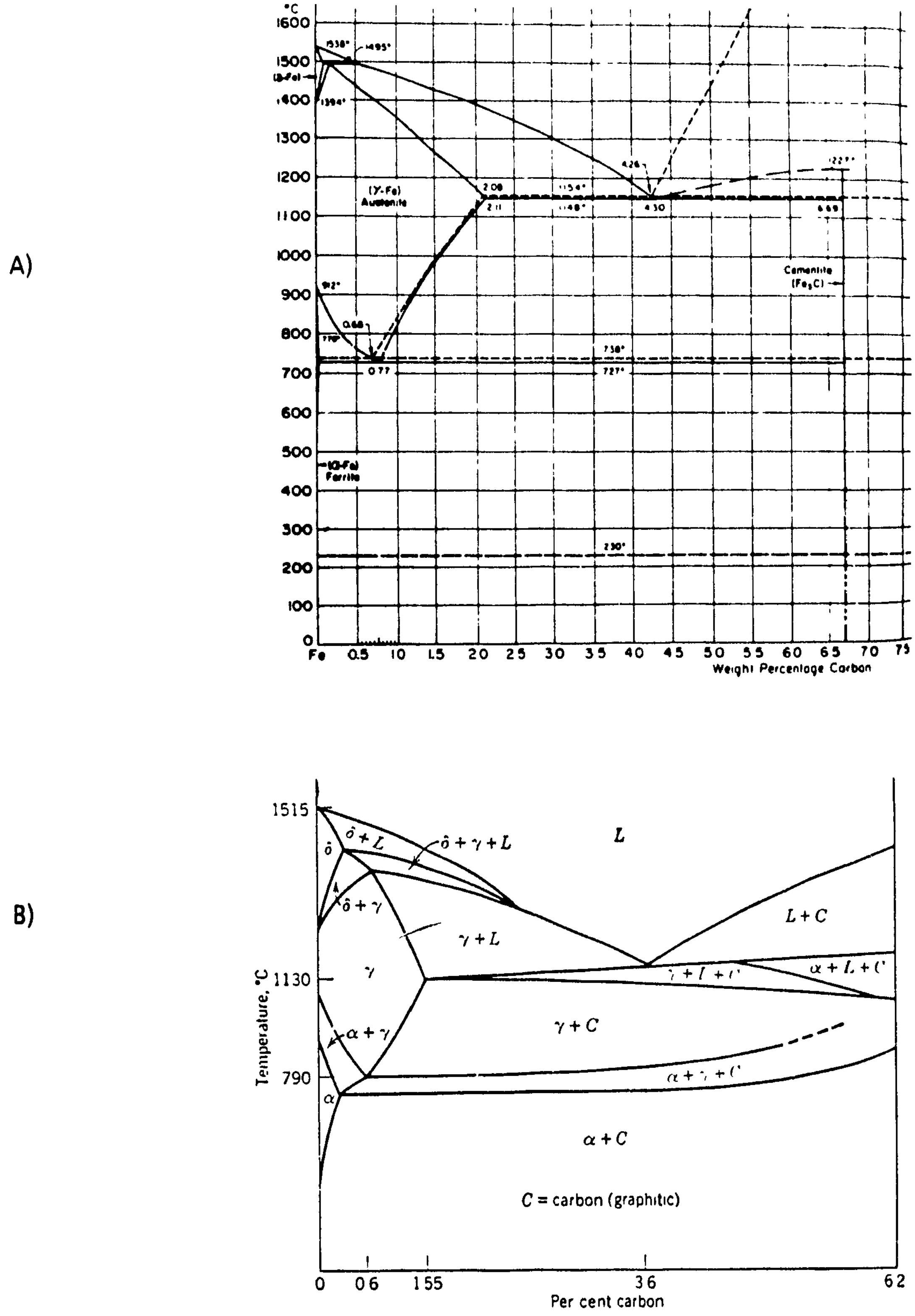

Fig. 23: Equilibrium diagram for (A) iron-carbon binary [13], and (B) iron-carbon pseudo-binary at 2% Si [14].

4. EXPERIMENTS WITH EUTECTIC STEELS

To avoid complications with carbon in cast iron, systematic investigations were made with Fe, 18% Si eutectic steels, which also provided another low m.p. system similar to the transformer steel melt. Fig 24 shows the equilibrium diagram for the Fe-Si binary

The results are summarized in Table. 7 In this steel too, with orifices measuring 400-600 µm in diameter, baseline instabilities were a problem. Although increasing manganese levels reduced such blockages, they did not significantly improve baseline stability High manganese levels did not lead to the dissolution of quartz glass, as was the case in cast iron, but started its devitrification (Fig 25).

Table 7 Summary of experiments in Fe, 18% Si eutectic steel

No.	% Mn	% B	Comments
1	0.2	-	blockages and baseline jumps
2	1 1	-	
3	2.1	-	
4	3.0	-	reduced blockages
5	4 0	-	
6	-	1	
7	-	2	
8	-	4	better operation h increasing boron
9	-	6	

When boron additions were made to Fe, 18% Si steel, baseline stability improved with increasing boron, and measurements were possible with 6% B, using a 330 µm orifice. Conditioning the orifice with high current helped in recovering a stable baseline in these steels.

Finally, the Fe-B binary was considered, Fig. 27, and an experiment was made in Fe, 4% B eutectic steel. Although no special problems were encountered in

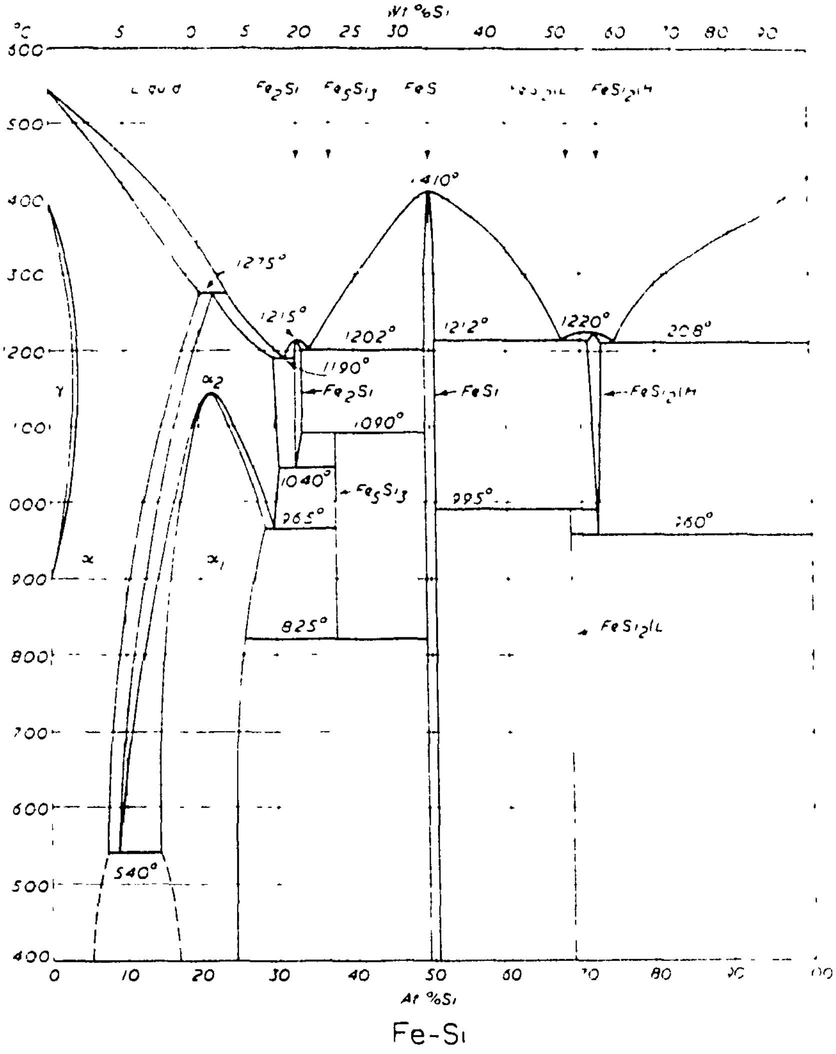

Fig. 24: Fe-Si binary phase diagram [3]

aspirating this steel through a 200 µm diameter orifice, and retaining a stable reference baseline in the latter stages of sampling, the sampling tube was attacked

Fig 25. Cross-section of a quartz glass sampling tube wall in contact with Fe, 18% Si, 4% Mn steel, showing devitrified layers.

by boron Figure 26 shows the deeply etched quartz glass sampling tube and the expanded orifice, after the experiment, and Fig. 28, the SiO_2-B_2O_3 equilibrium diagram Referring to the diagram, reaction product on the silica surface must have been molten, but it strongly adhered to silica Even on cooling to room temperature, the white opaque product layer chipped off with a layer of transparent silica attached, it was not possible to separate the two

Fig. 26: Attack by $\underline{B}_{Fe}$ on the quartz glass sampling tube Photograph on the right shows the expanded orifice (on the central axis, at equal distance from the sides and the bottom).

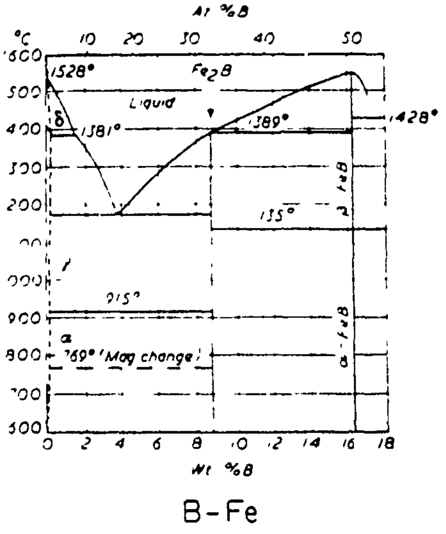

Fig. 27: Fe-B binary phase diagram [3]

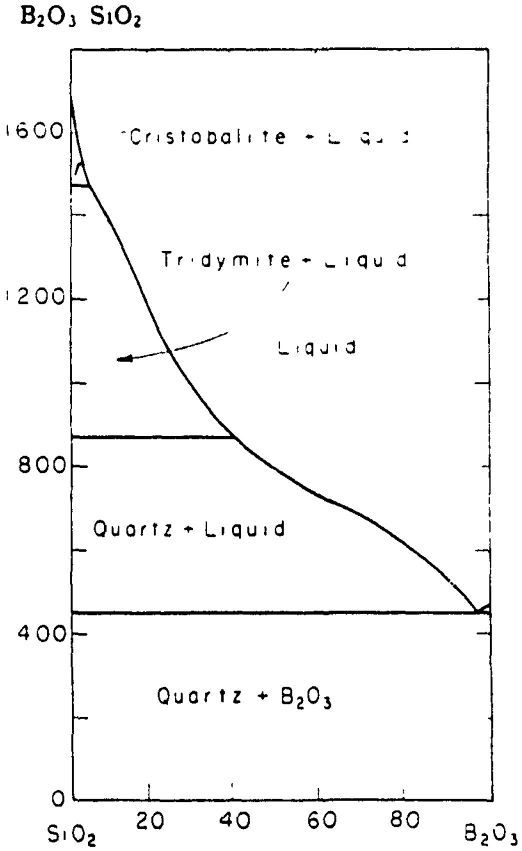

Fig. 28: SiO_2-B_2O_3 phase diagram [15].

5. EXPERIMENTS WITH LOW CARBON STEELS

From an economic point of view, operation of LiMCA would be most useful and would have the widest application in these steels Therefore, in spite of the earlier difficulties with low temperature analogues, the design and construction of a high temperature LiMCA probe was researched for use in low carbon steels

5.1 Construction of a Permanent Electrode

Although graphite tipped electrodes worked in a low carbon steel for a reasonable length of time (up to 20 minutes), a more permanent, steel tipped electrode was constructed using water cooling, Fig 29 It was desirable to extract heat from the tip of the electrode only, therefore, the electrode arrangement was surrounded by an insulating ceramic refractory The object of this was to draw as little heat from the steel bath as possible, thereby, to prevent an unwieldy solid shell forming on the melt surface, around the electrode The critical feature in the design was the length of the steel electrode If kept too long, the steel would melt into the ceramic shield and contact would be lost, if too short, there would be excessive build-up of solid shell around the electrode. The length "ℓ" of the steel rod could be estimated simply by considering uniaxial flow of heat through the steel electrode, assuming its sides to be completely insulated If the two ends of the steel rod are kept at 1535°C and 50°C, respectively, the rate of heat conduction along the steel rod, $\dot{Q}_{st}$, is balanced against the rate of heat input from the melt into the steel rod, $\dot{Q}_{melt}$, as shown schematically in Fig 30:

$$\frac{dQ_{st}}{dt} = k_{st} \frac{dT}{dz} \quad \frac{\Pi}{4} d^2 \tag{3}$$

$$\frac{dQ_{melt}}{dt} = h_{melt} \Delta T_{melt} \quad \frac{\Pi}{4} d^2 \tag{4}$$

where d: rod diameter, k_{st}: thermal conductivity of steel at a given temperature, h_{melt}: heat transfer coefficient in the molten metal, its value varying between 4000

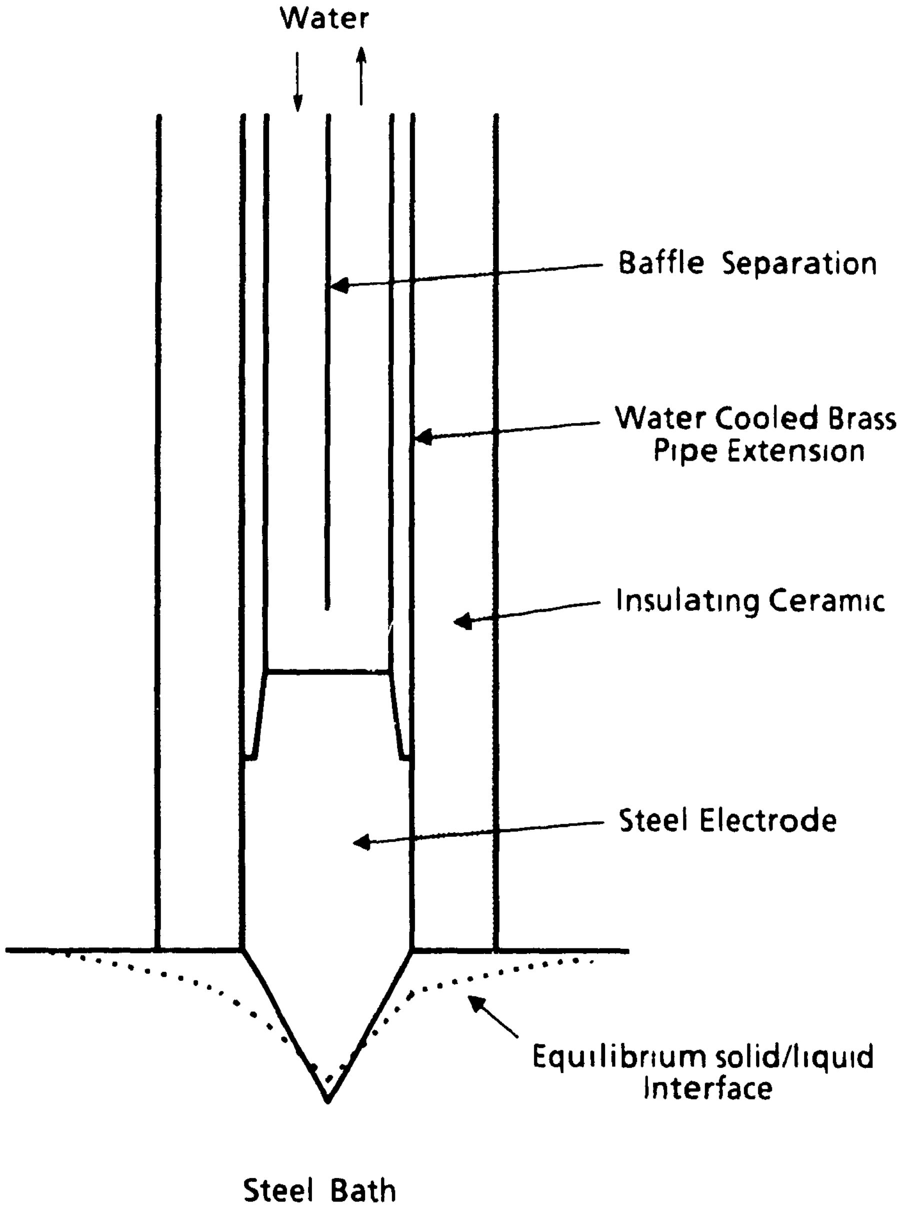

Fig. 29: Water-cooled electrode design for molten steel.

W m^{-1} K^{-1} under natural convection and 8000 W m^{-1} K^{-1} in forced convection conditions [16]. ΔT is the temperature difference across the boundary layer in the melt, and may be taken as 80°C maximum Equating $\dot{Q}_{st}$ to $\dot{Q}_{melt}$ and solving for ℓ:

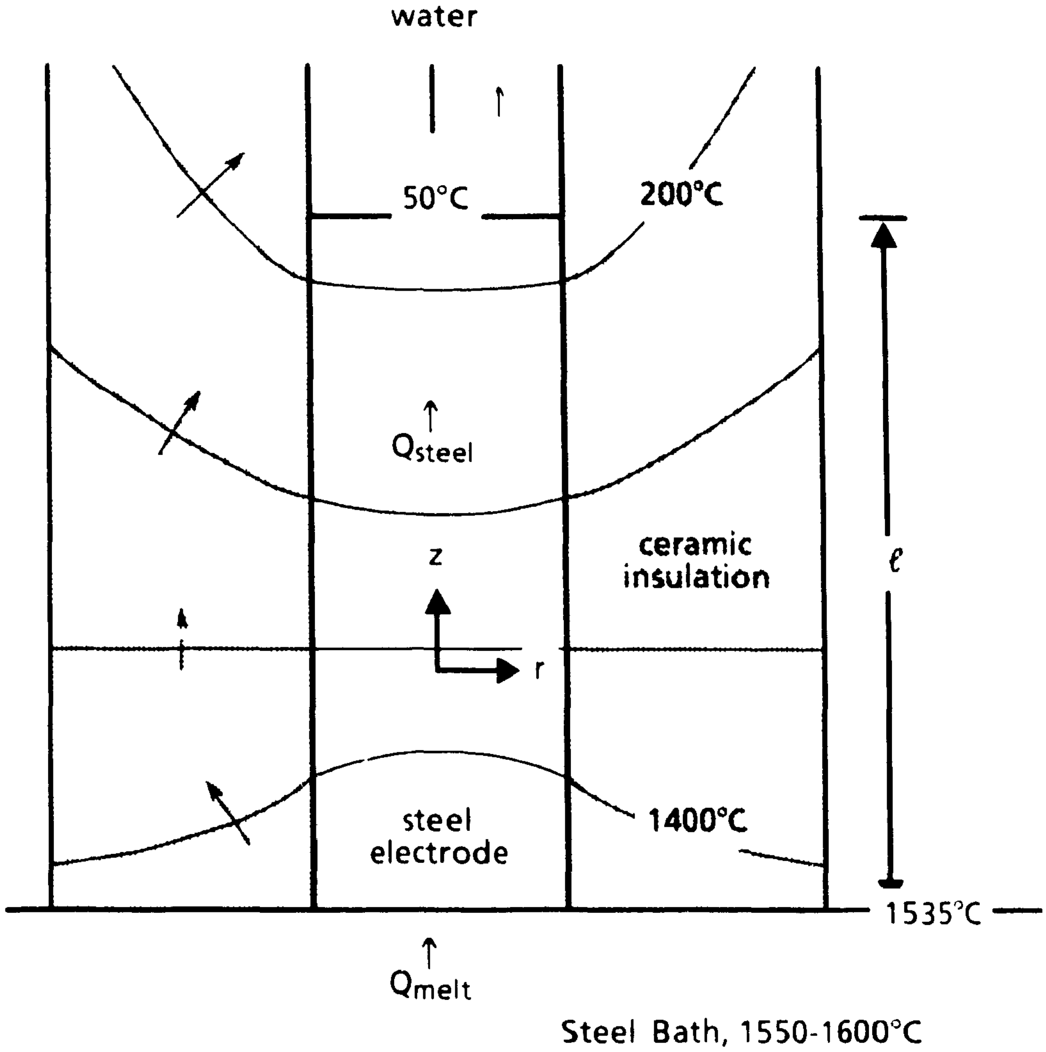

Fig. 30: Heat balance for the steel electrode with hypothetical isotherms, and the unknown dimension "ℓ".

$$\ell = \frac{\int_{50}^{1535} k_{st}\, dT}{h_{melt}\Delta T_{melt}} \tag{5}$$

Table 8 gives the thermal conductivities of a steel, and two silica based insulating refractories that could be used as shields For the case of forced convection in the melt, ℓ is computed to be 8.5 cm and the heat removed from the melt, using a 22 mm diameter electrode (O D of a $\frac{1}{2}$" standard pipe), $\dot{Q}_{melt} = 80$ W Fig 30 also shows the effect of radial conduction. Considering the radial direction only, in the lower and the hotter part, the electrode acts as a fin and the heat is conducted in the +ve r-direction, out of the refractory insulation, towards the water-cooled part, on the other hand, this would be reversed

Table 8 Thermal conductivities (W m^{-1} K^{-1}) of low C steel [3] and two silica based refractories [17].

T, °C	Steel†	Masrock™‡	Fusil 50™‡
20	60	[1900 kg/m^3,	[800 kg/m^3,
100	58	15% porosity]	40% porosity]
200	53		
400	46	0.7	0.2
600	37	0.9	
800	29		
1000	28		
1600	(30)		

† Fe, 0 08% C, 0 3% Mn

‡ Trade names of Harbison-Walker refractories Thermal conductivity and refractoriness of a given ceramic insulation depends on its bulk density

A water-cooled electrode was then assembled using Masrock™ insulation and a 6 cm long steel rod, connected to a $\frac{1}{2}$" standard brass pipe, as shown in Fig. 29, and tested in molten steel. The circuit was completed using a consumable steel rod as the other electrode. The electrode performed satisfactorily, as a low noise, stable reference baseline was achieved immediately after insertion, and maintained for an indefinite period. A 1 cm thick steel shell formed around the electrode, indicating that a longer steel tip could have been used as predicted.

5 2 Construction of a Sampling Tube

Since Nakajima reported unsatisfactory performance by the BN orifice in low carbon steel melts, and good operation for an orifice set in silica glass [18], it was decided to try this earlier design for the sampling tube, shown in Fig. 31. In this design, a graphite chamber prevented softened silica glass from collapsing inwards during aspiration, and also served as the inside electrode. Figure 31 shows two

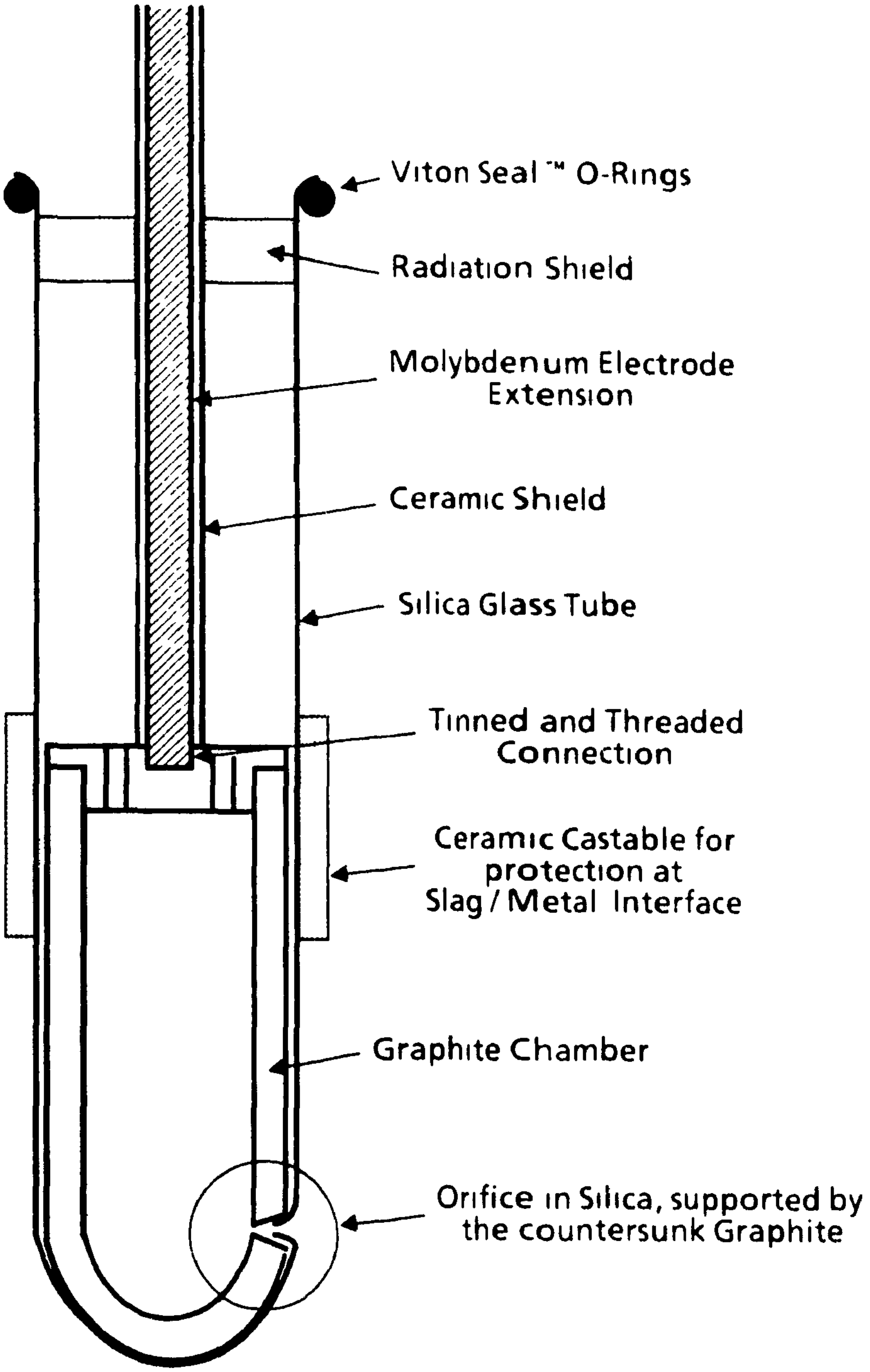

Fig. 31: Design of a silica glass sampling tube with a graphite back-up for low carbon steel.

A)

B)

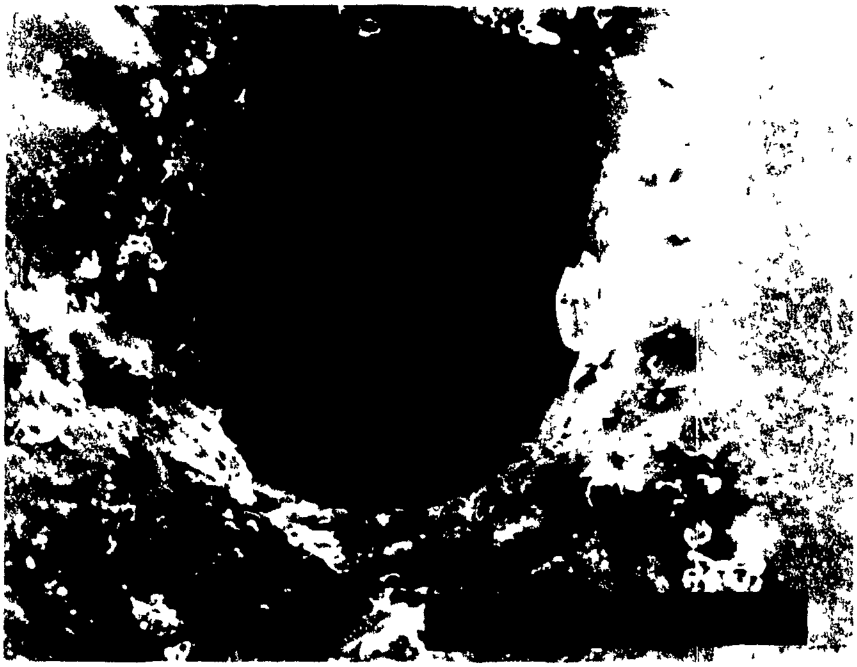

Fig 32: Silica glass stability in Armco Iron:
(A) Above 1550°C, initial diameter: 550 µm,
(B) Below 1550°C, initial diameter: 500 µm.

modifications made to the earlier design. The mechanically attached steel rod electrode extension was found to cause unacceptably high electronic noise because of deteriorated electrical contact at high temperatures, and was replaced with a molybdenum rod with a tinned and threaded connection Also, instead of having a 6 mm diameter hole at the back of the orifice, a better mechanical support was made by countersinking the graphite and shaping the silica glass locally such that it followed the contours of the countersink. Following this, an orifice was drilled and heat-shaped at the base of the contoured area.

The system was tried in Armco iron, de-oxidized with 0.2-0.4% Si, 0 5-1% Mn, with or without 200-400 ppm Al additions. Dissolved oxygen contents measured with a Celox probe incorporating Cr/Cr_2O_3 reference cell, decreased to a range of 60-8 ppm, from an expected value of 600-800 ppm, depending on the amounts of deoxidizers used.

The resilience of silica tubing against mechanical deformation was found to be remarkable: In the temperature range of 1535-1575°C, it was possible to apply 4-6 cm Hg positive pressure in order to to exhaust the metal from the sampling tube without noticeble deformation of the silica glass A similar negative pressure was used to aspirate the metal. This time, in combination with the ferrostatic pressure acting in the same direction, silica glass deformed towards the graphite back-up and filled any existing gaps between the two.

Orifices smaller than 400 µm invariably blocked in this steel, particularly following an aluminum addition. When forced with greater vacuum, they deformed and expanded. Therefore, orifice diameters ranging between 400-800 µm were used. Figure 32 shows the orifice stability in Armco iron subjected to low aspiration vacuums: below about 1550°C, orifices retained their geometry, while above this temperature, they expanded and their shape was lost

5.3 Results and Discussion

In spite of the mechanical stability of the orifice, LiMCA's operation in Armco iron did not prove to be any better than that in a eutectic silicon steel A high proportion of baseline instabilities prevented one from taking meaningful measurements Nevertheless, Nakajima made a claim for LiMCA measurements of inclusions in this steel, backed by inclusion counts via microscopy in solid samples obtained in parallel with LiMCA [18]. One such result is shown in Fig. 33. Since microscopy gave the frequency of inclusions per unit area N_A, it was necessary to convert this to the frequency of inclusions per unit volume N_V in order to compare the two results. This was done using the incorrect equation.

$$N_V = N_A^{3/2} \tag{6}$$

The correct expression being [19]:

$$N_V = \frac{\overline{N_A}}{\overline{d_V}} \quad \textit{or more generally} \quad N_{V_i} = \frac{\overline{N_{A_i}}}{\overline{d_{V_i}}} \tag{7}$$

where N_V is the number of particles per unit volume, $\bar{N}_A$ is the expected number of particles per unit area, and $\bar{d}_V$ is the average equivalent spherical diameter. Subscript i refers to the particles in the ith size class. To aid visualization, Fig. 34 illustrates this relation schematically, where an inclusion is cut into two halves by the plane of observation. For volume distributions, the sample volume would be the product of observed area A times the depth penetrated by inclusion ($\sim\frac{1}{2}$ of its diameter). However, when the sample is cut into two parts, the observed plane below is identical to the matching plane on top, and by observing one, the other is also completely determined. Therefore, the true depth penetrated by an inclusion, for the puposes of estimating a sample volume, is its full diameter. More precisely, for spherical particles, the distributions can be related via an integral equation, known as Abel's equation [19]:

$$N_A(r) = r\int_r^{\infty} \frac{N_V(R)}{\sqrt{R^2 - r^2}}\, dR \tag{8}$$

where $N_A(r)$ is the measured , and $N_V(R)$ is the desired quantity, and r and R refer to section and spherical radii.

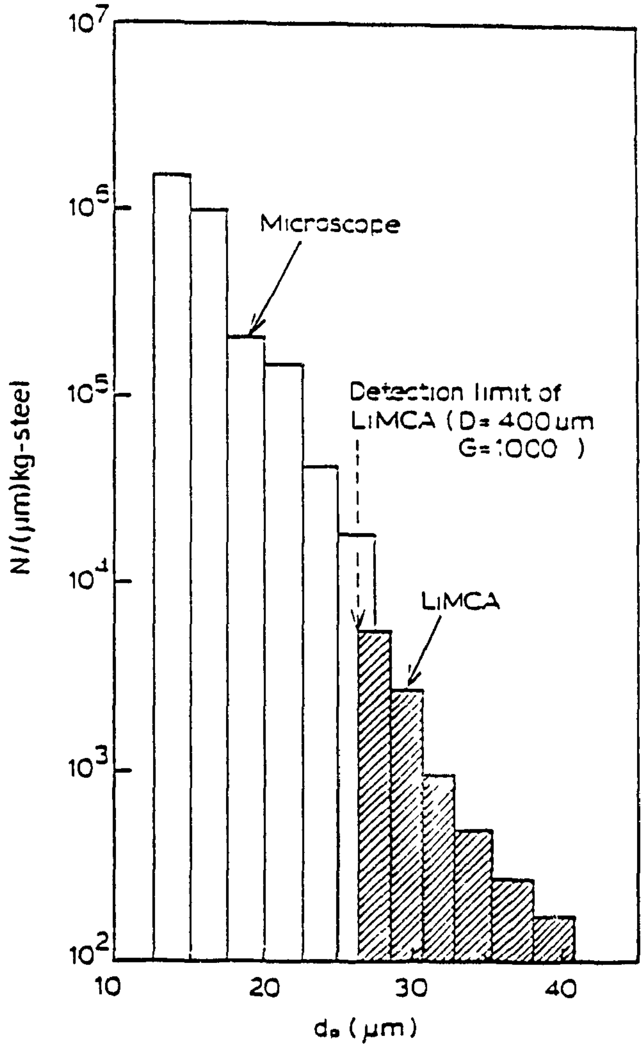

Fig. 33: Measured inclusion size distributions in Armco iron deoxidized with 1% Si, 0.4% Mn, and 0.1% Al Open bars are from inclusion counts obtained by examining 200 fields at 1000 x magnification under microscope, bringing the total area examined to 2 07 mm2 Hatched bars are from a LiMCA measurement with a 400 μm orifice, sampled under an electric current of 20 Amps, and a vacuum of 12 5 cm Hg, for 30 seconds, estimated sample mass being 60 g, from [18].

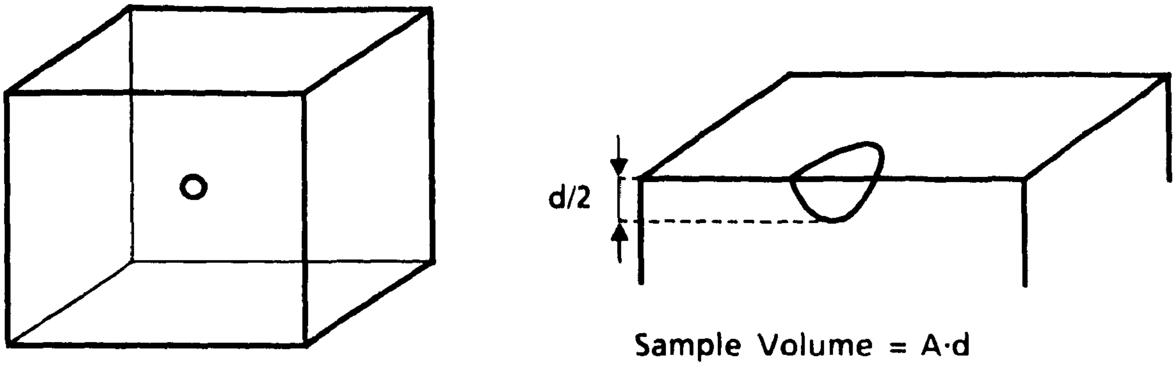

Fig. 34: Spherical inclusion inside a unit volume, and another, cut into half by a plane of observation. The observed area is A, and the volume, A·d.

By grouping inclusions into discrete size intervals, Δ, Eqn. 8 can be solved numerically, and the resulting expression has the following form:

$$N_{Vi} = \frac{1}{\Delta}\left[\alpha_{ii} N_{Ai} - \sum_{j=i+1}^{k} \alpha_{ij} N_{Aj}\right] \tag{9}$$

The coefficients α_{ij} have been tabulated by Saltykov (1958) and those relevant for integrating the microscopy counts in Fig. 33 are shown in Table 10. For integration, among the total of $k = 11$ size intervals, $i = 6$-11 were considered, with $\Delta = 2.5$ µm. Table 9 shows the data derived from Fig. 33, the estimated actual microscopy counts in the 200 fields examined, and the most probable volume distribution of inclusion sizes in this steel using the Schwartz-Saltykov method. As seen, more than two orders of magnitude difference exists between the given and the corrected inclusion frequencies, indicating a poor agreement between microscopy counts and LiMCA measurements, signifying that meaningful LiMCA measurements were not made. The same, of course, would apply for the three other inclusion size distributions reported in the same work, where excellent agreements between microscopy and LiMCA were shown. It is possible that the much lower than expected LiMCA counts were due to orifice expansion during these experiments.

Table 9. Inclusion size distributions in volume from Fig. 33, and the corrected values using the derived data from Fig. 33 and Saltykov's method.

Size Interval		Data derived from Fig. 33		Distribution in Volume, no. per gram		
i	*i* Δ, μm	Total no. in 2.07 mm2	no. per mm2	from Fig. 33	using Saltykov's method	using Eqn. 10
6	12.5-15	11	5.3	1 500	56 400	76 000
7	15-17.5	8	3.9	980	45 200	47 000
8	17.5-20	3	1.5	210	13 390	15 400
9	20-22.5	2.3†	1.1	150	10 900	10 400
10	22.5-25	1	0.5	42	4 540	4 000
11	25-27.5	0.6†	0.3	18	3 400	2 200

† Fractional counts probably resulted from an inclusion not being completely covered by the random area.

Table 10. Saltykov's table of coefficients, α_{ij}, for integrating microscopy counts.

Size Interval, *i*	*j*					
	6	7	8	9	10	11
6	0.3015	0.1081	0.0346	0.0163	0.0091	0.0058
7		0.2773	0.1016	0.0329	0.0155	0.0090
8			0.2582	0.0961	0.0319	0.0151
9				0.2425	0.0913	0.0310
10					0.2294	0.0872
11						0.2182

A simplified but a less accurate treatment for converting an area based distribution to a volume based distribution can also be obtained by considering the section diameters to be equal to the actual spherical diameters. Indeed, when a random plane cuts a sphere, the probability density that it will cut exactly on the equator is infinity, and that it will pass tangentially is zero. More quantitatively, 87% of the time the section diameters will be greater than ½ the spherical diameter This is illustrated in Fig. 35, with the accompanying derivations.

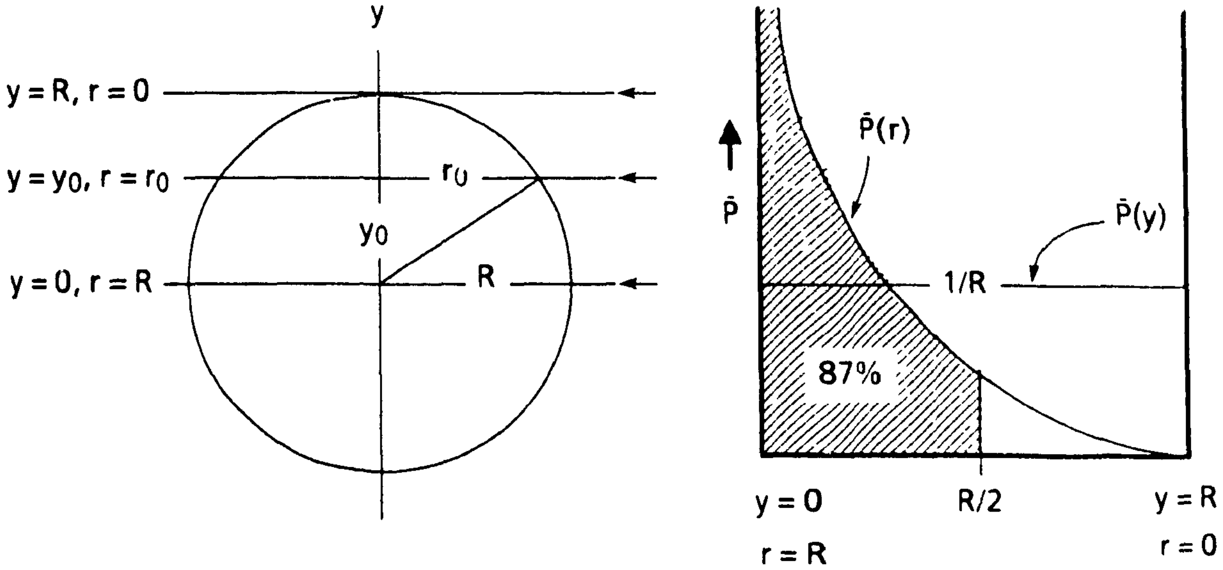

$$\bar{P}(plane\,at\,y=y_0) = \frac{1}{R}$$

$$P(y<y_0) = P(r<r_0) = \frac{y_0}{R} = \sqrt{1-(\frac{r_0}{R})^2}$$

$$\bar{P}(plane\,at\,r=r_0) = -\frac{\delta P(r>r_0)}{\delta r} = \frac{r_0/R}{\sqrt{1-(\frac{r_0}{R})^2}} \quad \frac{1}{R}$$

Fig. 35 Probability density of a random plane cutting a spherical inclusion of radius R at a section radius of r_0.

When the frequency of section diameters N_{Ai} is considered, some of these will belong to spheres with diameters greater than d_{Ai}. But, equally, some of the smaller section diameters will belong to spheres of diameter d_{Ai}, and the two trends will tend to cancel each other. For consistency with quantitative metallography, the expected area fraction of a phase is equal to its volume fraction. For the size class i, equating the section diameter d_{A_i} to spherical diameter d_{V_i} will yield:

$$N_{A_i} \frac{\pi}{4} d_i^2 = N_{V_i} \frac{\pi}{6} d_i^3$$

$$N_{V_i} = \frac{N_{A_i}}{\frac{2}{3} d_i} \tag{10}$$

Using this relation, the size distribution in the final column of Table 10 was calculated from the data given in column 3. As seen, good agreement was observed betwen this, and Saltykov's method. This latter method was then used in estimating the equivalent metallographic sample area of a LiMCA sample in Fig. 16, and also in converting metallographic counts into volume counts for the copper alloys, in Part 3

6. DISCUSSION AND CONCLUSIONS

6.1 Inclusion Frequency versus Inclusion Size

One significant observation in the measured size distributions in Fe, 5% B, 3% Si steels, was the rapid decline in inclusion population with increasing size intervals. A 50% increase in size brought about a reduction of 10-100 times in the number of inclusion counts. Also significant was the great degree of variability in inclusion numbers in different melts. In Figures 14, 17 and 18, the number of inclusions greater than 10 µm were:

Fig. 14:	after melt-down	15 000 kg^{-1}
Fig 17:	after melt-down	60 kg^{-1}
Fig. 17:	after air injection	750 kg^{-1}
Fig. 18:	after melt down	850 kg^{-1}

Apparently the macro-inclusion content of the steel depended on its previous history. For instance, the melt in Fig. 14, once prepared as the alloy, had been remelted and used many times in different experiments. In spite of this great variance, the mass and the number density of these macro-inclusions represented only a small fraction of the total inclusion content of more than 10^{10} kg^{-1} (based on the metallographic counts in Fig. 15).

An upper limit for particle size in an electrolytic sensing zone (of the Coulter-Counter type) was given as 40% of the orifice diameter, a high concentration of particles greater than this size increasing the likelihood of blockages and baseline instability [20]. This is probably also true for LiMCA. Taking this value, and the minimum particle size detected, the dynamic range of LiMCA may be said to be 6-40% of the orifice diameter in metallic melts.

Because of the great variability in the number density of macro-inclusions, and the limited size range that can be analysed by LiMCA, orifice diameters had to be fine-tuned for a given application. It was necessary to select an orifice diameter and sample volume such that, for the sampling accuracy of inclusion populations to be at least better than ±20%, the number of inclusions counted ($d>0.06\,D$) in a typical LiMCA sample would have to be greater than 100 (from Poisson's distribution, the standard deviation $s \approx \sqrt{N}$, and the sampling error for a count of 100 is $\pm\varepsilon_{0.95} \approx (1.96\cdot\sqrt{100}) / 100 \approx \pm 20\%$) At the same time, the population of larger inclusions ($d > 0.4\,D$) needed to be small so as to not impair the LiMCA's operation. The rapid decline in inclusion populations with increasing size was therefore beneficial to fulfilling this criteria For the transformer steel melt, for instance, the optimum orifice diameter was in the range of 150-200 µm.

From the aforementioned, then, it follows that LiMCA's key application is in the characterization of the macro-inclusion content, (i.e the tail end (right hand side) of the inclusion size distribution), of molten metals.

6.2 Stability of Silica Glass in Steelmaking Environments

Since silica glass provided a sensing zone that was superior to boron nitride (the other high temperature material tested for steel melts), its chemical and mechanical stability were also important considerations.

6.2.1 Chemical Stability

Silica glass was attacked by boron in a eutectic boron steel. Since boron was a stronger deoxidizer than silicon, this would be expected, thermodynamically. However, no attack was observed by the transformer steel melt containing 5% B, 3% Si. Inclusions in this steel were spherical, indicating that they were molten borosilicates rather than solid silica Analysis of the top slag gave 34% B_2O_3, 44% SiO_2 by weight, the balance being iron. The equilibrium diagram between SiO_2 and B_2O_3 in Fig. 29, on the other hand, indicates that molten borosilicate compounds would need to contain 80-90% SiO_2 to be in thermodynamic equilibrium with solid silica. Equilibrium between $\underline{B}_{Fe}$, $\underline{Si}_{Fe}$ and the borosilicate inclusions could be expressed by the reaction:

$$2\,\underline{B}_{Fe} + 3/2\,\{SiO_2\} = \{B_2O_3\} + 3/2\,\underline{Si}_{Fe}$$

Using the thermodynamic data in Table 11, currently available interaction coefficients for dilute solutions of iron at 1600°C in Table 12, and the known composition of the transformer steel melt, the compositional relationship between B_2O_3 and SiO_2, in borosilicate inclusions can be calculated:

Table 11. Data used to compute the equilibrium constant between $\underline{B}_{Fe}$, $\underline{Si}_{Fe}$ and borosilicate inclusions [11]

i	Reaction	ΔG°_i, J mol^{-1}	ΔG°_i (1600°C)
1	$2\langle B\rangle + 3/2\,(O_2) = \{B_2O_3\}$	$-1\,228\,840 + 210\,T$	-835 510
2	$\langle B\rangle = \{B\}$	$+50\,210 - 21\ 8\,T$	+9 380
3	$\{B\} = \underline{B}_{Fe}$	$[-55\,780 - 24.6\,T$ or $-101\,940 - 0\,T]^{\ddagger}$	-101 940†
4	$1/2\,(O_2) = \underline{O}_{Fe}$	$-117\,050 - 2\ 89\,T$	-122 560
5	$2\,\underline{B}_{Fe} + 3\,\underline{O}_{Fe} = \{B_2O_3\}$	N A.	-282 710
6	$\underline{Si}_{Fe} + 2\,\underline{O}_{Fe} = \{SiO_2\}$	$-582\,150 + 222\,T$	-166 240
7	$2\,\underline{B}_{Fe} + 3/2\,\{SiO_2\} = \{B_2O_3\} + 3/2\,\underline{Si}_{Fe}$	$[+6\,825 - 21\ 5\,T$ or $+99\,145 - 70\ 7\,T]$	-33 350†

$\langle solid\rangle$, $\{liquid\}$, (gas at 1 atm) $\equiv$ pure component st state, $\underline{X} \equiv 1$ wt% st state

† Calculated from the data given in [11], pp 5, 81, 381

‡ First expression is estimated by assuming Fe-B solution to be regular Then partial molar enthalpy of mixing of boron may be taken to be $\bar{h}_B = \Delta H^\circ_3 = RT\ln(\gamma^\circ)$, and constant over a temperature range, hence $\Delta G^\circ_3 = RT_0\ln(\gamma^\circ) + RT\ln(M_{Fe}/100\ M_B)$ where $T_0 = 1873$°K, γ° is the activity coefficient of B at infinite dilution, w r t pure component standard state This gives a limiting (maximum) value for the entropy term (ideal mixing) Taking partial molar entropy of mixing of boron equal to zero gives the other limiting expression below In general, temperature dependance of ΔG°_3 will vary between these two extremes
Bracketed expressions are estimates

$$\ln K_7 = -\frac{\Delta G_7^0}{RT}, \quad at\ 1600°C\quad Log\,K_7 = 0\ 92$$

$$Log\,\frac{h_{Si}^{3/2}\cdot a_{B_2O_3}}{h_B^2\cdot a_{SiO_2}^{3/2}} = 0\ 92 \qquad and \qquad a_{B_2O_3} = 0\ 3\ a_{SiO_2}^{3/2} \qquad at\ 1600°C$$

Assuming ideal solution behaviour, the mole fractions of silicates and borates would be $x_{SiO_2} = 0.8$, and $x_{B_2O_3} = 0.2$, or 78% SiO_2 and 22% B_2O_3 by weight, closer to the

Table 12 Composition of the transformer steel alloy and associated interaction coefficients, for calculating the activities of dissolved boron and silicon

	B	Si	C	Mn	S	P
%	5	3	0.01	0.2	0.012	0.035
e_B	0 02 [1] **0.06** [2] 0 11 [3]	**0.08** [2] 0.13 [3]	**0.22** [2] 0.24 [9]	N.A.	**0.05** [14]	
e_{Si}	**0.20** [2] 0 35 [3]	0 06 [3] 0 09 [4,5] 0 11 [6,7] 0.12 [8] **0.1**	0 20 [4] **0.24** [10,11] 0.29 [12]	**0.28** [13]	**0.06** [14]	0.16 [15] **0.11** [16]

h_i is the activity, and f_i is the activity coefficient of i, w r t 1 wt% st state Interaction coeficients in bold are used in the calculations

References

[1] H Schenk and E Steinmetz, *Arch. Eisenhuttenw* , **39**,1968, pp 225, cited in [12]
[2] D L Ball, *TMS-AIME*, **239**, 1967, pp 31, cited in [12]
[3] C Ji, R Yu, and S Liu, "Thermodynamic activity of silicon and boron in Fe-Si-B ternary melts at 1450°C", *Can Metall Q* **27**, (1), 1988, pp 41-47
[4] J Taylor, *JISI*, **204**, 1964, pp 420, cited in [12]
[5] A Kuba and H Sakao, *Tetsu to Hagane*, **54**, 1968, pp 314, cited in [12].
[6] F Wooley and J F Elliot, *TMS-AIME*, **239**, 1967, pp 1872, cited in [12]
[7] J Chipman and R Baschwitz, *TMS-AIME*, **227**, 1963, pp 473, cited in [12]
[8] E T Turkdogan et al , *TMS-AIME*, **227**, 1963, pp 1258, cited in [12]
[9] R Yu, S Liu, and C Ji, "Activities of carbon and boron in Fe-C-B melt and coefficients of reactions of activities at 1500°C", *Iron Steel (China)*, **22**, (11), 1987, pp 8-10
[10] I S Kulikov, "Activity of components in Fe-Si-C melts", *Russ. Metall.*, (1), 1977, pp 78-80
[11] H Schenk et al , *Arch Eisenhüttenw* , **39**,1968, pp 803, cited in [12]
[12] D Schroder and J Chipman, *TMS-AIME*, **230**, 1964, pp 1492, cited in [12]
[13] Y Kojima and K Sano, *Tetsu to Hagane*, **51**, 1965, pp 1122, cited in [12]
[14] S Ban-ya and J Chipman, *TMS-AIME*, **245**, 1969, cited in [12]
[15] V Cirilli et al , *Chim et L'Ind* , **50**,1968, pp 33, cited in [12]
[16] H Schenk, E Steinmetz and R Gohlke, *Arcl Eisenhüttenw* , **39**,1968, pp 109, cited in [12]

liquidus curve The equilibrium constant used in this calculation was reliable for 1600°C. However, from the estimated expression for K_7 in Table 11, the temperature dependence of the equilibrium constant is expected to be small.

The stability of silica glass towards manganese additions, however, was not the same. Manganese was added to cast iron and to eutectic silicon steel, in an attempt to form steel systems containing molten inclusions. Figure 36 shows critical manganese contents for a given silicon level and temperature, needed to form molten manganese silicates. In cast iron, manganese contents above a critical level, liquefied surface slag and presumably silica inclusions, but also lead to the dissolution of silica glass. With increasing manganese in silicon eutectic steel, the silica glass was not dissolved, but was attacked in a different way that led to the formation of white-opaque (and probably devitrified), layers.

6.2.2 Thermomechanical Stability

Although crystabollite, the crystalline form of silica, melts at 1725°C, silica glass softens at a lower temperature, the commercial grade used had a softening point of 1650°C. The Littleton softening point would be defined as the temperature at which 24 cm long, 0.7 mm diameter silica glass rod would elongate at a rate of 1 mm/min, and this corresponds to a calculated viscosity value of 6.6 Pa s. One area that would be particularly affected by softening would be the orifice, because of its highly curved surface. Small orifices would tend to close, and large ones, expand However, orifice stability, for diameters greater than 400 µm, was observed to be good up to 1550°C Indeed, silica glass tubing was able to support 8 kPa positive pressure just below the molten metal surface, without visible plastic deformation The circumferential tensile stress this would cause on a 1 5 mm thick, 40 mm dia silica glass tubing would be:

$$\sigma_{\theta,\theta} = \Delta P \frac{D}{2t} = 107\ kPa \tag{4}$$

or the equivalent stress at the top end of a 5 m long, freely hanging rod ($\rho = 2200$ kg m^{-3}). In contrast, the tensile strength of the silica glass at 900°C was given as 81 MPa and at room temperature, 50 MPa [23]

Resistance to deformation (viscosity) of silica glass at high temperatures is most affected by impurities, particularly alkali and hydroxyl ions, which help break Si-O bonds and lower viscosity. The alkali content of the commercial grade was 2 ppm, and the hydroxyl content, 180 ppm, by weight. Optical (Infra-Red) grades of silica glass having minimal hydroxyl contents (<5 ppm OH^- by weight) are available, and

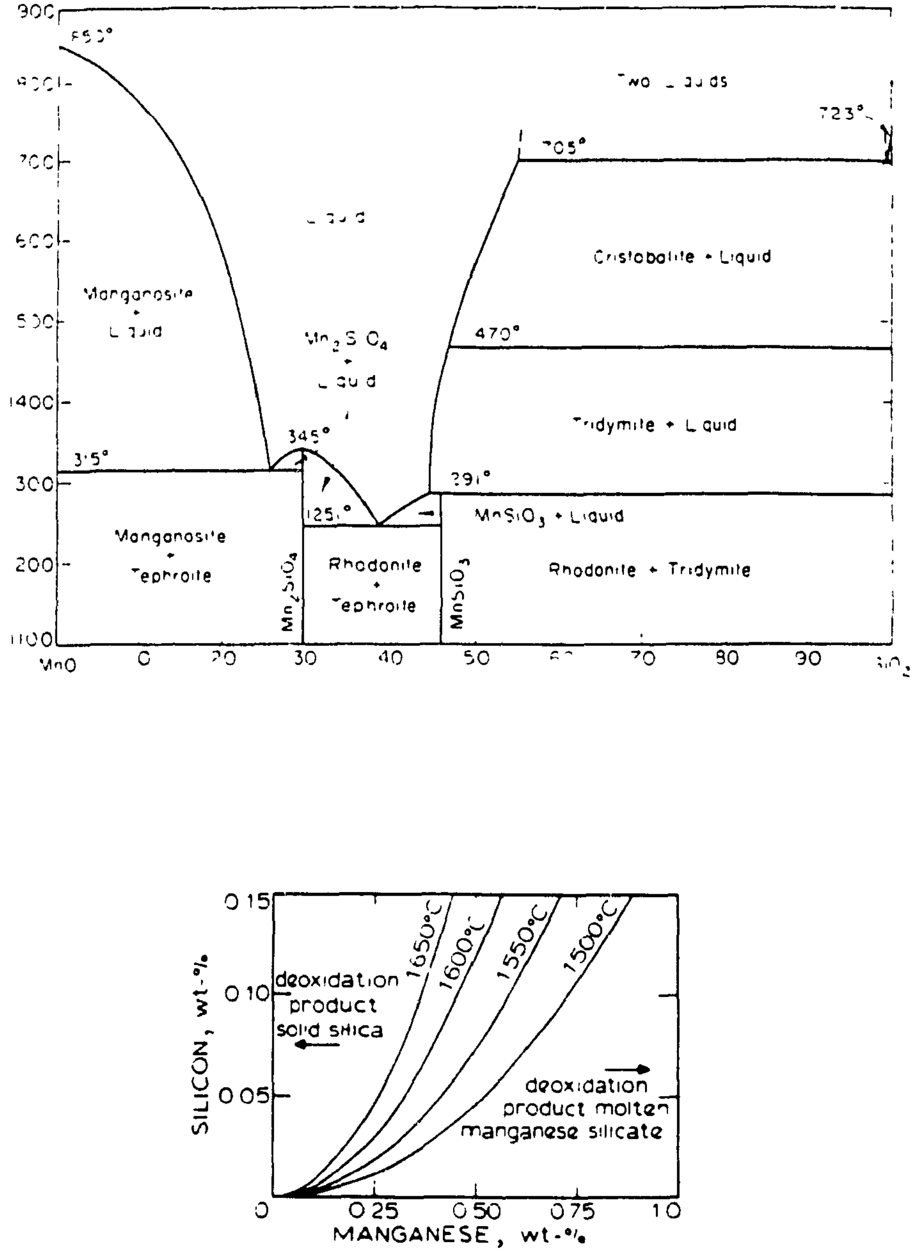

Fig 36. Top: SiO_2-MnO phase diagram [21]. Below: critical silicon and manganese contents of steel forming solid / liquid oxide inclusions for various temperatures [22]

these have significantly higher softening temperatures. as high as 1740°C, above the melting point of crystabollite [24] Although these grades are expensive, they can be used for small inserts for orifices, to be fixed on the side of a sampling tube made of a suitable refractory, such as Masrock™

6 3 Stability of Reference Baseline vs Melt Chemistry

Ultimately, LiMCA's successful operation as a measuring instrument rests on establishing a stable reference baseline across the feeder electrodes placed on either side of the sensing zone (orifice) where, ideally, electrical disturbances in the form of resistive pulses would only be caused by the passage of suspended particles This was almost perfectly achieved for the boron - silicon steel, demonstrating that LiMCA can work for steel melts However, LiMCA's operation in iron alloys was found to be strongly influenced by melt chemistry. Under identical conditions for instance, other low melting point iron alloys, namely cast irons and eutectic silicon steels, presented problems in attaining a stable reference baseline In all instances, baseline instabilities were shown to derive from physical deterioration of the orifice (see Part 1, Section 3 5.3) In the following, various hypotheses are tested to understand the cause for the loss of baseline stability with changing melt chemistry

6.3.1 Role Played by the Physical State of Inclusions

Boron additions were found to be beneficial for LiMCA's operation in steel melts Even when boron attacked the silica glass (i.e the boron eutectic steel), it was possible to resume a stable reference baseline across the sensing zone for inclusion measurements

One result of a boron addition is the creation of indigeneous, liquid, borosilicate inclusions To see if the physical state of the inclusions in steels had an important bearing on LiMCA's operation, iron alloys were tested following additions of ferro-silicon and ferro-manganese to the melt These were added in order to promote the formation of indigeneous, fluid, manganese silicates Although LiMCA's operation using a silica glass orifice gradually improved with increasing manganese levels, it was still not comparable to its performance in boron, silicon steels If liquid inclusions were important, a rapid change in LiMCA's operation above a critical manganese content would have been expected

However, the issue remains clouded, as high levels of manganese also attacked the silica glass In earlier work [5], a BN orifice was tested at increasing manganese levels in cast iron, but again, improved operation, similar to that in boron - silicon steels, was not observed On the other hand, it was possible to obtain a stable baseline in the boron - silicon steels, after an aluminum addition, and to take LiMCA measurements of solid aluminum borosilicate inclusions, and also, of solid BeO inclusions in a copper beryllium alloy at 1100°C, which represented another high temperature metallic melt system (see Part 3) Evidently, the above observations suggest that the physical state of the inclusions is not the most significant factor for LiMCA's smooth operation in steel melts.

6 3.2 Role Played by the Interfacial Properties of Sensing Zone Refractory, Molten Metal and the Inclusions

During experiments with the boron silicon steel melts, a high contact angle had been observed for metal drops landing on nearby refractory surfaces. It was decided to investigate the wettability of molten steel and silica glass, in order to see if it was significantly different for boron containing steels, versus steels of other compositions Thus, it may be argued that if sensing zone deterioration is caused by the interaction of inclusions with the orifice wall, then:

i inclusions will be more likely to stick and cause deterioration if they wet the orifice material more then they wet molten steel,

ii when the above condition is true, the driving force for deterioration will be greater, the greater the surface tension of inclusions.

Table 13 gives contact angles between relevant metallic melts and refractory materials used in forming the sensing zone (silica glass, boron nitride) or between the melt and possible inclusions Similarly, Table 14 provides data on the surface tensions of these materials Since interfacial data were not available for steels containing boron and silicon, these were estimated from the solidified sessile drops on a silica glass substrate, using the profiles in Fig. 37. The sessile drops were prepared in a high frequency induction furnace, under an argon atmosphere.

Table 13 Contact angles between relevant metallic melts (M) and sensing zone refractories (R) or inclusions (I)

M	R or $I_{(state)}$	Temp (°C)	$\theta_M{}^{\circ}$	Comments
Fe, pure	$SiO_{2(gl)}$	1600	115	(a)
Fe, pure	$SiO_{2(gl)}$	1550	110	(a)
Armco Iron	$SiO_{2(gl)}$	1535	113	Ar atm (b)
Fe, 0.04% Al	$SiO_{2(gl)}$	1535	117	Ar atm (b)
Fe, 5% B, 3% Si	$SiO_{2(gl)}$	1200	146	Ar atm (b)
Fe, 4% B	$SiO_{2(gl)}$	1200	154	Ar atm (b)
Fe, 18% Si, 6% B	$SiO_{2(gl)}$	1200	126	Ar atm (b)
Fe, 18% Si	$SiO_{2(gl)}$	1200	140	Ar atm (b)
Fe, pure	$Al_2O_{3(s)}$	1600	135, 144	(a)
Fe, 3 4% C	$Al_2O_{3(s)}$	1600	112	(a)
Fe, 8% Si	$Al_2O_{3(s)}$	1550	114	(c)
Fe, 0.4% C	$Al_2O_{3(s)}$	1520	105	(a)
Fe, 0 4% C	$Al_2O_{3(s)}$	1570	106	(c)
Fe, pure	$BN_{(s)}$	1550	112	Ar atm (d)
Cu	$SiO_{2(gl)}$	1100	148-134	vac -He (d)
Cu	$BN_{(s)}$	1100	146	vac (d)
Cu	$BeO_{(s)}$	1100-1300	140-122	Ar atm (d)
Cu	$Al_2O_{3(s)}$	1200	140	Ar atm. (d)
Al	$TiB_{2(s)}$	900-1100	98	(d)
Al	$BN_{(s)}$	850-1000	142	(d)

(a) cited in [25], (b) calculated from profiles in Fig 37, (c) from [26], (d) from [27]

To compute interfacial properties from sessile profiles, the Laplace equation of capillarity, a relation derived from thermodynamic considerations in 1805 to give the pressure difference across a curved surface, may be used.

$$\Delta P = \gamma\left(\frac{1}{R_1} + \frac{1}{R_2}\right) \tag{11}$$

where γ is the surface tension, and R_1 and R_2 are the principle radii of curvature of the surface at the point considered. For a sessile drop then:

$$\gamma\left(\frac{1}{R_1} + \frac{1}{R_2}\right) = \frac{2\gamma}{R_0} + \rho g z \tag{12}$$

Table 14. Surface tensions and interfacial tensions of selected materials.

Material	Temp. (°C)	γ, J/m^2	Comments
$Fe_{(l)}$	1600	1.890, 1.842	(a), (b)
$Fe_{(l)}$	1536	1.872	(b)
$Fe_{(s)}$	1400	2.150	(a)
$Al_2O_{3(l)}$	2050	0.690	(c)
$Al_2O_{3(s)}$	1600		
$Al_2O_{3(s)}$	1475	0.930	(a)
$SiO_{2(l)}$	1800	0.307	(d)
$SiO_{2(gl)}$	1600	0.301	(c)
$SiO_{2(gl)}$	1500	0.298	(c)
$SiO_{2(gl)}$	1470	0.296	(c)
$B_2O_{3(l)}$	1400	0.097	(c)
$B_2O_{3(l)}$	1300	0.094	(c)
$B_2O_{3(l)}$	1200	0.090	(c)
$Fe_{(l)}$ / $SiO_{2(gl)}$	1550	0.94	(†)
$Fe_{(l)}$ / $Al_2O_{3(s)}$	1550	2.38	
$Cu_{(l)}$ / $SiO_{2(gl)}$	1100	1.4-1.2	
$Cu_{(l)}$ / $Al_2O_{3(s)}$	1100	1.93	

(^{a}) cited in [25], (^{b}) in [3], (^{c}) in [26], (^{d}) in [28]

(†) Interfacial tensions are calculated by Young-Dupré equation at a three phase boundry: $\tilde{\gamma}_{1,2} + \tilde{\gamma}_{1,3} + \tilde{\gamma}_{2,3} = 0$ On a flat refractory substrate, neglecting the effect of gas phase, the equation becomes. $\gamma_{M,R} = \gamma_R - \gamma_M \cos \theta_{M\text{-}R,G}$

where z is the vertical height, measured from the top of the drop, R_0 is the principal radius of curvature at the top, and R_1 and R_2 are both functions of z. Numerical solutions of Eqn. 12 have been developed to obtain surface tension and contact angle data from measured coordinates of points P(x,z) on the sessile profile. In one such method, developed at the University of Toronto, coordinates could be entered from an arbitrary origin, and for optimum results, properties were obtained from a least square fit profile [29,30]. This procedure was used to obtain the related values in Table 13. A sample of the fitted profile for Fig. 37C (Fe, 5%B, 3%Si steel), with measured data points super-imposed, is shown in Fig. 38. Since the photographs of the profiles were taken at room temperature, the measurements did not account for the 10% volume change from the molten state, some of which presumably remained as porosity within the metal.

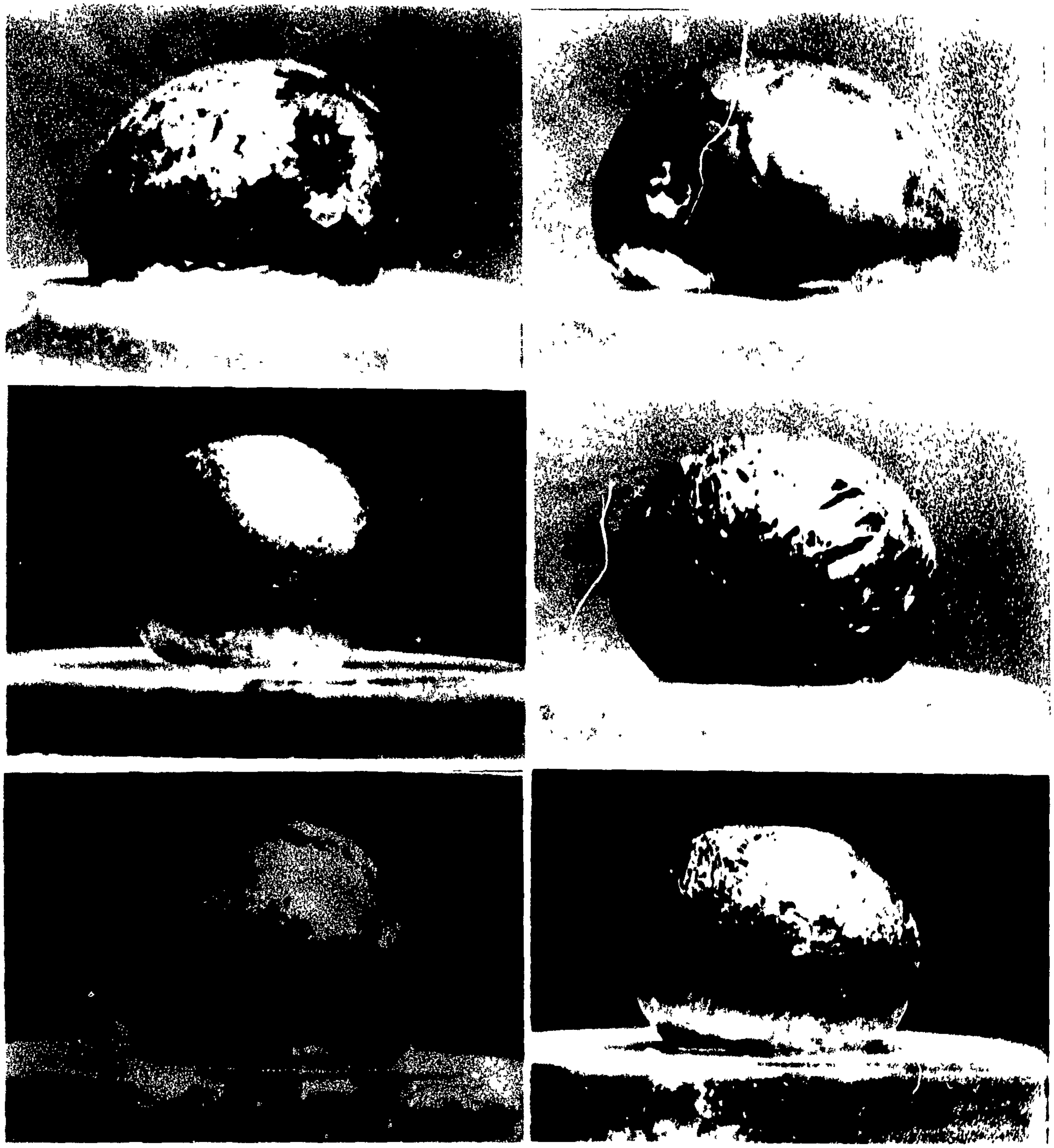

Fig. 37: Profiles of sessile steel drops on a silica glass substrate From left to right, and in descending order: (A) Armco Iron, (B) Armco Iron with 400 ppm Al, (C) Fe, 5%B, 3% Si, (D) Fe, 4% B, (E) Fe, 18% Si, 6% B (F) Fe, 18% Si

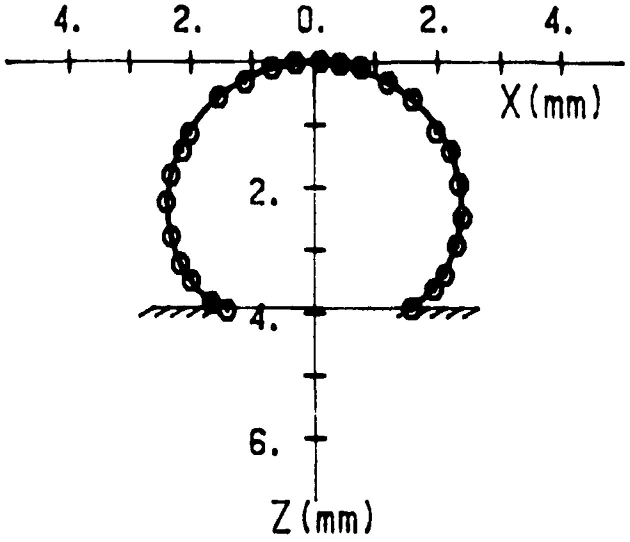

Fig. 38: Calculated profile and the measured data points for Fe, 5% B, 3% Si steel (Fig. 37C).

From the tables, it is clear that boron additions made the steels less wetting with respect to silica. However, this is not unique, silicon additions also made the steel less wetting towards silica, and baseline deterioration was observed in the eutectic silicon steels. At this point, it was felt that more interfacial data between metal (M), orifice wall refractory (R), and inclusions (I) were necessary to make a critical assessment of the effect of interface properties on the baseline stability of LiMCA and to test the hypothesis that inclusion / orifice wall interaction was the cause of baseline instability. An observation supporting the mechanism of orifice deterioration to be an inclusion / orifice wall interaction, is the fact that the boron-silicon transformer steel can be directly cast through thin (50 µm) slits into strips without any clogging, while the presence of aluminum in this steel impairs LiMCA's operation, owing to the formation, no doubt, of solid inclusions, non-wetting to the steel.

Interfacial data of this nature must also be important in explaining inclusion removal mechanisms in steel filtration, ladle nozzle / tundish metering valve

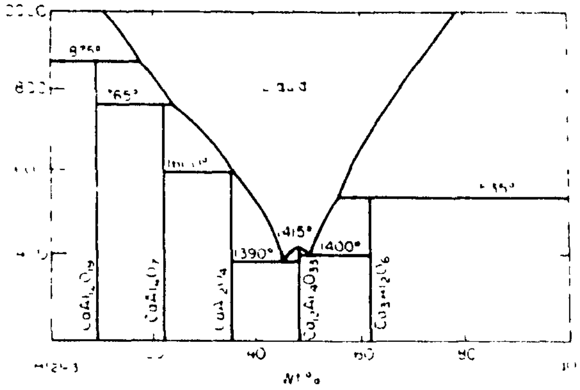

Fig. 39: CaO-Al_2O_3 phase diagram [31].

blockages, the physical removal of inclusions by refractories, top slag, tundish weirs and dams, and the growth of inclusions by coagulation leading to macro-inclusions.

6.4 Conclusions and Suggestions for Future Work

It has been possible to operate LiMCA at high temperatures, and to monitor macro-inclusion levels in boron containing steel melts For other chemistries, the present work did not succeed in reducing the "noise" in the observed baseline stabilities in order to allow meaningful measurements. This baseline instability has been shown to derive from physical deterioration of the orifice (see Part 1, Section 3.5.3). It is therefore hypothesized that interface properties between inclusions, steel melt and the orifice wall must be largely responsible in bringing this about, but it has not been possible to support this because of insufficient interfacial data

As an addendum to this work, it is noted that the steel melts were prepared in an induction furnace where, while taking LiMCA measurements, the power had to be turned off, causing the melt to undergo cooling at a rate of 10-15 °C/min. With decreasing temperature, the solubility products of oxides in steels also decrease, and this results in the nucleation and growth of new oxides. If oxides are non-wetting to the metal, then some of this growth would take place at refractory surfaces, including the surfaces close to the sensing zone. Therefore, taking measurements in a large reservoir of metal, such as a tundish, where temperatures remain steady, would be expected to help LiMCA's operation.

An interesting case for future work would be to test the LiMCA probe, in calcium treated steels When calcium silicide is successfully injected into steels, inclusion morphology changes, and alumina inclusions become molten calcium aluminates (Fig. 39), and nozzle / metering valve blockages are greatly reduced. This, therefore, would be expected to favour LiMCA's operation.

REFERENCES

1. S. Kuyucak, "On-line detection of non-metallic inclusions in molten iron", M.Eng. Thesis, McGill University, Montreal, 1985.

2. F. Dallaire, "Electric sensing zone signal behaviour in liquid aluminum", M.Eng. Thesis, McGill University, Montreal, to be submitted.

3. J.C. Smitthells, ed., in *Metals Reference Book*, 5th edn., Butterworths, Boston, 1976.

4. R. Hultgren et al., in *Selected Values of the Thermodynamic Properties of the Elements*, ASTM, 1973.

5. S. Kuyucak, in ref. 1, pp. 55, 1985.

6. Perry's Chemical Engineers Handbook, 6th ed , pp. 5.15, 5.34, McGraw-Hill, 1976.

7. S. Dowdy and S. Weardon, in *Statistics for Research*, pp. 225, Wiley, 1983

8. D.A. Flinchbaugh "Determining size distribution of oxides in plain carbon steels by halogen-in-organic solvent extraction and Coulter Counter measurement", *Analytical Chemistry*, **43**, (2), 1971, pp 178-182.

9. H. Bader, J.R. Gordon, and O.B. Brown, "Theory of coincidence count correction for optical and resistive pulse particle counters", *Review of Scientific Instruments*, 43, (10), 1972, pp. 1407-1412.

10. G.F. Ruff, personal communication, General Motors Corp , Central Foundry Div., Saginaw, Michigan, 1988.

11. E.T. Turkdogan, in *Physical Chemistry of High Temperature Technology*, Academic Press, New York, 1980.

12. C. Bodsworth and H.B. Bell, in *Physical Chemistry of Iron and Steel Manufacture*, 2nd edn., Longman, London, 1972.

13. O.W. Devereux, in *Topics in Metallurgical Thermodynamics*, pp 122, Wiley, New York, 1983.

14. J. Wulff, H.F. Taylor, and A.J. Shaler, in Me*tallurgy for Engineers*, pp 130, Wiley, New York, 1960.

15. Phase Diagrams for Ceramists, Vol. 2, 1975 Supplement, M.K. Reser, Ed., The American Ceramic Soc., Colombus, Ohio, 1975.

16. F. Mucciardi, PhD. Thesis, McGill University, Montreal, Quebec, 1980

17. Product Catalogue, Harbison-Walker Refractories, Division of Dresser Ind., Inc., One Gateway Center, Pittsburgh, Pennsylvania, 1986.

18. H. Nakajima, "On the detection and behaviour of second phase particles in steel melts", Ph. D Thesis, McGill University, Montreal, 1987, pp. 376-381.

19. R.T. DeHoff and F.N. Rhines, in *Quantitative Microscopy*, pp. 131, McGrow-Hill, New York, 1968.

20. R.H. Berg, "Sensing zone methods in fine particle size analysis", *Mats. Research and Standards*, **5**, (3), 1965, pp. 119-125.

21. Phase Diagrams for Ceramists, M.K. Reser, Ed., The American Ceramic Soc., Colombus, Ohio, 1964.

22. E.T. Turkdogan, "Causes and effects of de-oxidation occuring during cooling and solidification of steel", *TMS-AIME*, **233**, 1965, pp. 2100.

23. *Optical Fused Quartz and Fused Silica Catalogue*, Heraus-Amersil, Inc., Sayreville, N.J., 1981.

24. E.T. Turkdogan, in Physicochemical Properties of Molten Slags and Glasses, pp. 13, The Metals Society, London, 1983.

25. A.W., Cramb and I. Jimbo, "Interfacial considerations in continuous casting", *Iron and Steelmaker*, **16**, (6), 1989, pp. 43-55

26. *The Oxide Handbook*, Ed. G.V. Samsonov, 2nd Edn., IFI / Plenum Data Co. N.Y. 1982.

27. *Handbook of Refractory Compounds*, Eds. G.V. Samsonov, and I.M. Vinitskii, IFI / Plenum Data Co., New York 1980.

28. *Molten Salts Handbook*, Ed. G.J. Janz, Academic Press, New York 1976.

29. Y. Rotenberg, L. Boruvka, and A.W. Neumann, "Determination of surface tension and contact angle from the shapes of axisymmetric fluid interfaces", *J. of Colloid and Interface Science*, **93**, (1), May 1983, pp. 169-183.

30. T. Utigard and J.M. Toguri, "Interfacial tension of aluminum in cryolite melts", *Met. Trans. B*, **16B**, June 1985, pp. 333-338.

31. Phase Diagrams for Ceramists, Vol. 4, G. Smith, Ed., The American Ceramic Soc., Colombus, Ohio, 1981.

18. H. Nakajima, Ph. D. Thesis, "On the detection and behaviour of second phase particles in steel melts", 1987, pp. 376-381.

19. R.T. DeHoff and F.N Rhines, in *Quantitative Microscopy*, pp 131, McGrow-Hill, New York, 1968

20. R.H Berg, "Sensing zone methods in fine particle size analysis", *Mats Research and Standards*, **5**, (3), 1965, pp 119-125

21. Phase Diagrams for Ceramists, M.K. Reser, Ed , The American Ceramic Soc , Colombus, Ohio, 1964.

22 E.T. Turkdogan, "Causes and effects of de-oxidation occuring during cooling and solidification of steel", *TMS-AIME*, **233**, 1965, pp 2100

23. *Optical Fused Quartz and Fused Silica Catalogue*, Heraus-Amersil, Inc , Sayreville, N.J , 1981.

24. E.T. Turkdogan, in Physicochemical Properties of Molten Slags and Glasses, pp 13, The Metals Society, London, 1983.

25. A.W., Cramb and I. Jimbo, "Interfacial considerations in continuous casting", *Iron and Steelmaker*, **16**, (6), 1989, pp 43-55

26. *The Oxide Handbook*, Ed. G.V Samsonov, 2nd Edn., IFI / Plenum Data Co N Y 1982.

27. *Handbook of Refractory Compounds*, Eds. G.V. Samsonov, and I M Vinitskii, IFI / Plenum Data Co., New York 1980.

28. *Molten Salts Handbook*, Ed. G.J. Janz, Academic Press, New York 1976

29. Y. Rotenberg, L. Boruvka, and A W. Neumann, "Determination of surface tension and contact angle from the shapes of axisymmetric fluid interfaces", *J. of Colloid and Interface Science*, **93**, (1), May 1983, pp. 169-183

30. T. Utigard and J.M. Toguri, "Interfacial tension of aluminum in cryolite melts", *Met. Trans. B*, **16B**, June 1985, pp 333-338

31. Phase Diagrams for Ceramists, Vol. 4, G. Smith, Ed , The American Ceramic Soc., Colombus, Ohio, 1981.

List of Figures

List of Tables

PART 3: APPLICATION OF LiMCA TO LIQUID COPPER AND ITS ALLOYS

1. INTRODUCTION

Copper and its alloys form another high temperature metallic melt system of industrial importance where application of LiMCA would be useful. Although information on the effects of inclusions are much less documented in copper alloys, their presence would be expected to cause problems in forming operations and structural applications, as in steels.

In the unalloyed state, the presence of oxygen in molten copper causes copper oxide (Cu_2O) inclusions to form after solidification. With regards to inclusions in copper, it is this phenomenon that has received the greatest attention in ASTM specifications for copper metal. One way to remove oxygen from copper is via reduction by hydrocarbons. Subsequent electrolysis to produce oxygen free copper provides a metal that has low dissolved, and insoluble particulate, residuals. Another way to remove oxygen is to use deoxidants such as phosphorous, where the deoxidized copper invariably contains the balance of the dissolved deoxidizer. In both cases, if the oxygen is not reduced sufficiently (theoretically to below 10 ppm) cuprous oxide forms, and its susceptibility to further reduction within the structure, during annealing or welding, causes internal voids. This is the major cause for hydrogen embrittlement. In both types of copper, standard procedures have been established to check for the presence of Cu_2O particles [1]. Since this oxygen will be dissolved in molten copper, an oxygen probe would be suitable to check liquid metal quality prior to solidification.

When the more reactive metals are used, for the purposes of alloying or deoxidation, naturally some metal oxide particles remain as indigeneous inclusions in the melt because of incomplete physical separation. LiMCA would then be useful in detecting their number density. However, the presence of these particles would seem to be of a lesser concern since only one ASTM specification (for very thin foils) describes a procedure to check for inclusions other than Cu_2O [2].

In general, the deleterious effects of inclusions on mechanical properties is magnified when the base metal becomes stronger, since at higher loads, decohesion of inclusions from the metal matrix, leading to void formation become the major cause for weakness. This is probably why the effects of inclusions are much less documented in copper alloys than in steels Nevertheless, the presence of inclusions do cause a reduction in the mechanical properties of higher strength copper alloys, such as those that are heat treatable via solution treatment and precipitation hardening. Although ASTM specifications do not call directly for non-metallic inclusion determination, it is necessary to control the macro-inclusion contents in order to be able to attain the specified levels of ductility (determined by twist and bend tests), and fatigue strengths Copper alloy manufacturers, aware of the problem, have devised methods to quantify macro-inclusion levels in their alloys One such method for copper - beryllium alloys has been referred to in Chapter 3

2. PRELIMINARY WORK

To design a LiMCA probe for copper melts, it was decided to use electrolytic copper in the preliminary work· Owing to its low oxygen and low particulate content, it was expected that this would cause minimum interference with the electrodes and orifice. To find a suitable electrode system, copper in the form of suitably cut cathode plates was melted in silicon carbide crucibles, in an electric resistance furnace under a charcoal atmosphere, and deoxidized further with copper phosphorous (Cu, 15% P) shots for independent electrode tests (see Part 1, Section 3.5.1). Since molten copper can dissolve a large amount of oxygen, and this oxygen is highly active,(see Fig. 1), the control of dissolved oxygen was important for the successful operation of the electrodes. Among the various electrode materials tried, graphite, steel, and molybdenum gave erratic performances with regards to "baseline stability", because of oxidation at points of electrical contact This oxidation resulted from changes in the oxygen potential of the melt with time The more noble metal, nickel was found to operate reliably over an indefinite period of time. Although nickel is fully miscible with copper, forming complete solid and liquid solutions (see Fig. 2), rapid dissolution of the nickel rod electrode was avoided by placing a refractory shield around its side While molten copper and nickel have similar densities, molten copper in equilibrium with solid nickel is probably slightly lighter than pure copper. Table 1 gives their estimated respective densities at 1150°C

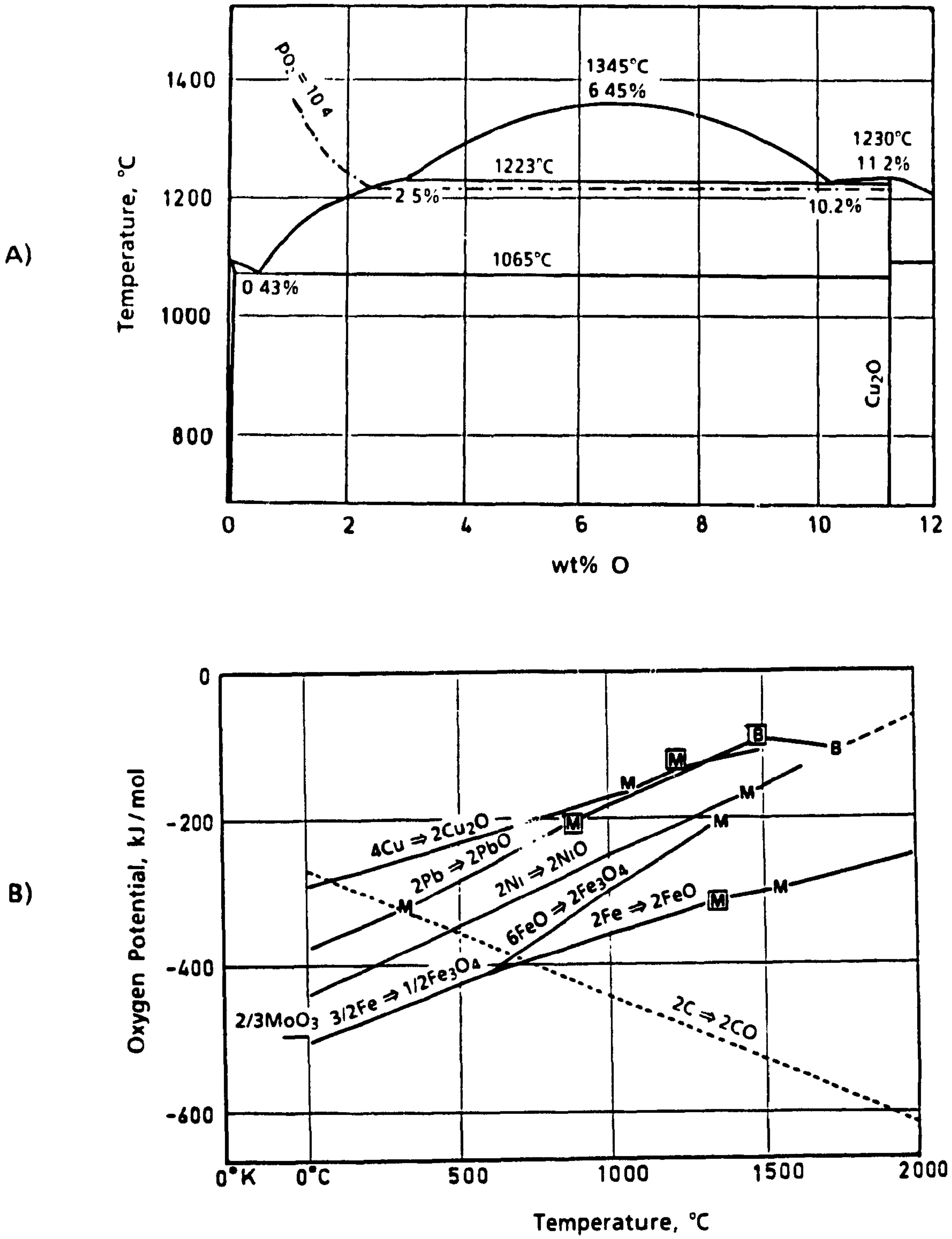

Fig. 1: (A) Cu-O phase diagram [3], (B) temperature vs. oxygen potential for copper and other metals of interest.

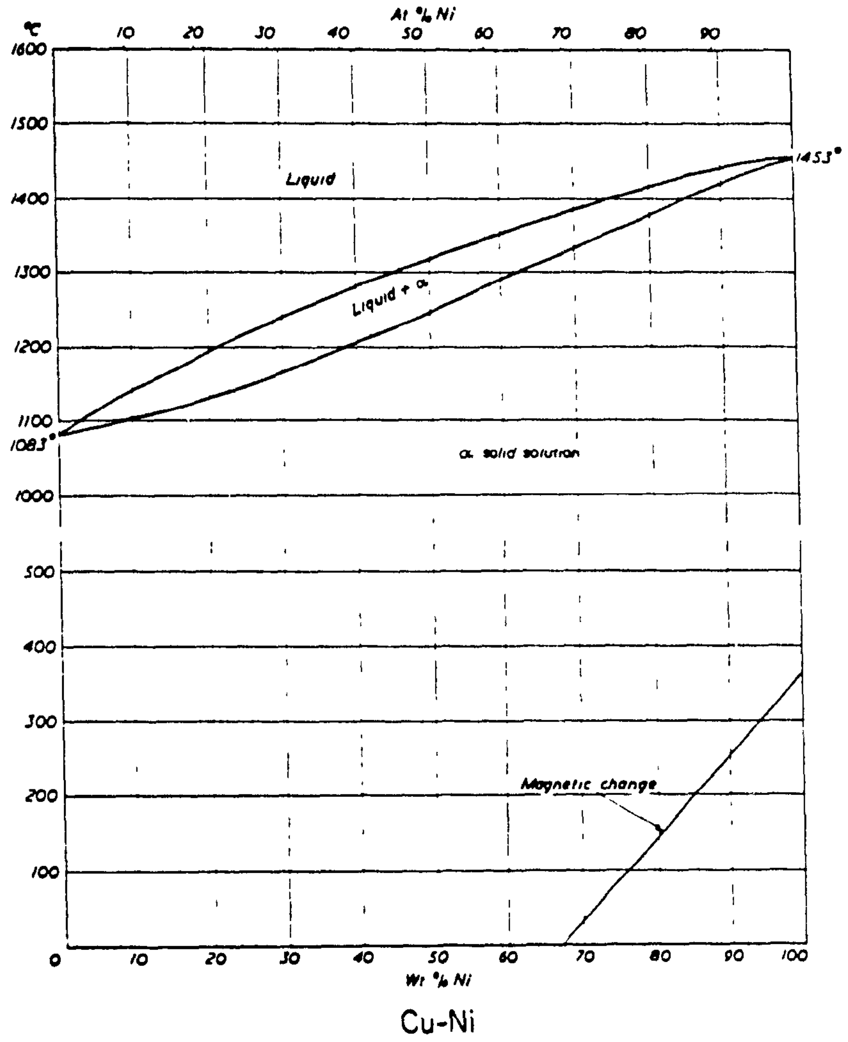

Fig. 2: Cu-Ni phase diagram [6].

and 1200°C, assuming the excess volumes of mixing to be zero. Hence, natural convection inside the protective refractory shield was limited, and the kinetics of

Table 1. Densities (kg m^{-3}) of pure copper and molten copper nickel alloy in contact with pure nickel (1).

Temperature, °C	Cu	Ni	Molten Cu-Ni Alloy in Contact with Ni (2)
α, kg m^{-3} °C^{-1}	-0 803	-1 103	
β, kg m^{-3} °C^{-2}	0 67 × 10^{-3}	0 81 × 10^{-3}	
1083	8030		
1150	7980	8160(3)	8000, $x_{Ni} = 0.11$
1200	7940	8080(3)	7970, $x_{Ni} = 0\ 24$
1423		7770	

(1) Densities of pure Cu and Ni at their m p , and the temp coeff of density, α, are from [4] β is estimated from $1/V(\partial V/\partial T)_P \simeq \text{Const.}/T$ [4] $d\delta/dT = \alpha + \beta(T - T_m)$

(2) $v_{alloy} = x_{Cu}\, v_{Cu} + x_{Ni}\, v_{Ni} + v^E$ where v^E is taken to be zero v^E is expected to be positive since $v^E = (\partial g^E/\partial P)_{T,x_i}$ and $g^E > 0$ ($\gamma^0_{Ni(l)} = 2\ 22$ [5]), and $(\partial g^E/\partial P)_{T,x_i} > 0$, since condensed phases become less ideal with increasing pressure.

(3) Supercooled liquid

nickel transfer from the dissolving electrode tip was governed by diffusion through a stagnant liquid layer of underlying copper melt. Protected in this way, extended electrode tips, at the end of an experiment at 1100-1200°C, were found to have dissolved only slightly into their respective shields. Curiously, molten lead, whose dissolved oxygen is nearly as active as that of copper, did not present a special materials problem with regards to electrodes, and the use of steel electrodes in lead was satisfactory. This is most likely because the solubility of oxygen in molten lead at its melting point is only 5 ppm [6]. Therefore, oxidation is limited because of a depleted oxygen layer, and a slow supply of oxygen to the electrode.

Silica glass sampling tubes, similar to those used in low melting point iron alloys, were used for copper melts. Molten copper samples were aspirated using a gauge vacuum of 20-30 kPa, through LiMCA orifices measuring 250-300 µm. Under a sampling current of 60 amperes, a moderate concentration of resistive voltage pulses above a threshold value of 20 µV could be detected and counted. Signal to noise ratio in these experiments was particularly good, background noise was measured to be 3-5 µV within a 0.5-5 kHz frequency band.

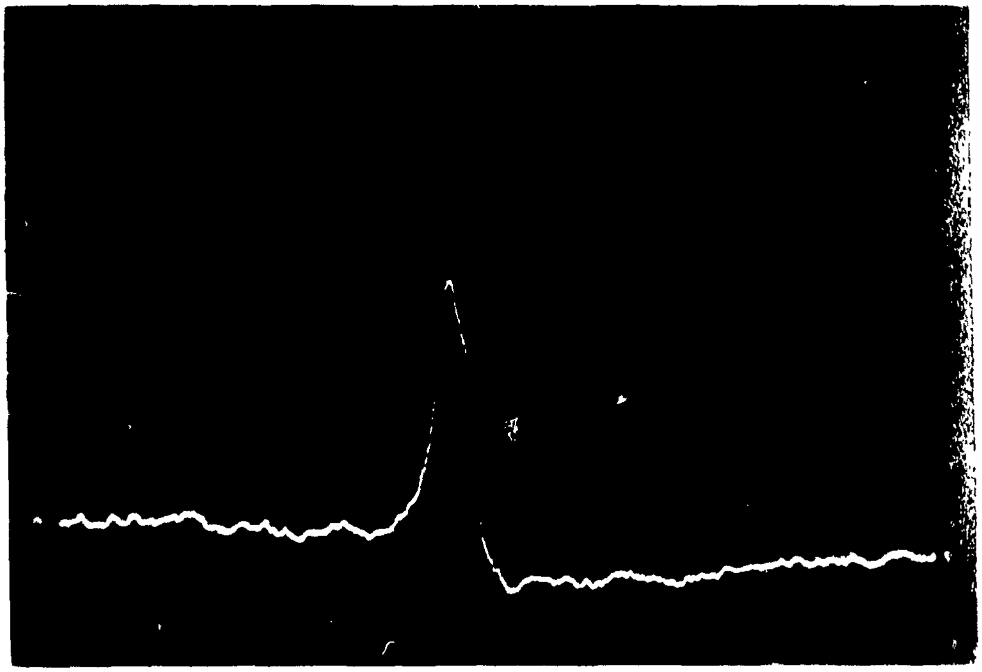

Fig. 3: Trace of a voltage pulse during the passage of a 42 µm particle entrained in copper, and passing through a 280 µm orifice set in silica tube
Vertical displacement: 50 µV/div, time scale: 1 ms/div.

Dimensional stability of the orifice was found to be very good. As the SEM micrograph in Fig 13A shows, there was no evidence of chemical attack on the sensing zone.

Figure 3 shows a typical oscilloscope trace of a resistive voltage pulse, while the bar charts in Fig. 4 show measured inclusion populations already existing in the copper melt. A convenient way of rating metal quality by Limca, is to quote the total number of inclusions greater than a certain size. In this regard, N_{20} and N_{25} in the bar charts correspond to the total number of particles greater than 20 and 25 microns respectively, per kg metal. In a typical measurement, data were acquired in steps of 30 second periods of sampling, the sample volumes being estimated from measured discharge coefficients of such orifices in molten zinc (see PART 2, Section 2.2.1). Fig. 4 indicates a sharp decline in the population density of inclusions with increasing size. This was typical in copper melts, inclusion population densities,

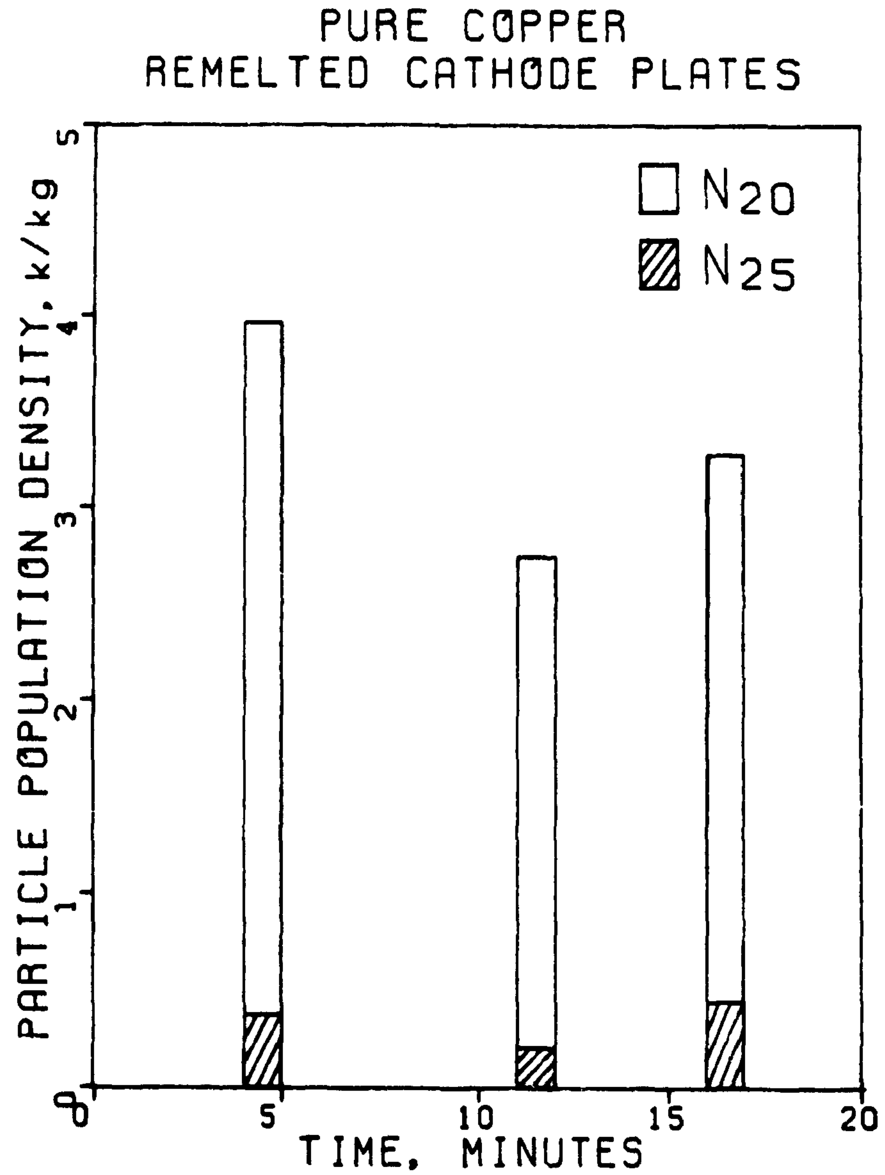

Fig. 4 Inclusion population densities in molten copper measured by Limca (thousands per kg) vs. melt holding time (minutes). N_{20} and N_{25} refer to the number of inclusions greater than 20 and 25 µm respectively. Therefore, the white area in the bars are the population density of inclusions in the size range 20-25 µm.

monitored above a threshold detection level of 20 µV, were quite sensitive to the size of orifice used.

3. EXPERIMENTS IN COPPER - BERYLLIUM ALLOYS

3.1 Introduction

Copper rich beryllium alloys are heat treatable, and have important industrial applications. In the precipitation hardened condition, they are the highest strength copper alloys. Figure 5 shows the copper - beryllium phase diagram, where up to 2.7% Be is soluble in copper. Referring to Table 2, the strength of Alloy 3 is comparable to high strength stainless, and maraging nickel steels. The combination of good mechanical properties (high tensile and fatigue strengths, retained at moderately elevated temperatures (85% at 300°C)), together with good corrosion and wear resistance and high thermal and electrical conductivity, make these alloys particularly useful in those field applications where high demands are placed on the materials of construction. These include drill collars used in oil and geological drilling, aircraft bearings, electrical current carrying springs and a number of other electrical fixtures [7].

In most applications of these alloys, fatigue strength is an important component of their combined set of properties. The inevitable presence of beryllia particles within the alloy matrix can reduce fatigue life. It can also give rise to surface defects in thin sheet and strip products. A reduction in the number density and size of oxide inclusions should therefore improve fatigue performance as in other alloy systems. While no published information of a quantitative nature is available, the copper industry, aware of the issues, has devised quality assessment procedures similar to those performed by the steel industry. These procedures are based on a metallographic examination of standard samples, to characterize the inclusion content of a given batch of melt produced.

3.2 LiMCA vs. Metallographic Measurements and Discussion

Table 2 provides information in regard to the chemical compositions and relevant physical properties of the copper alloys used in these LiMCA experiments. In view of

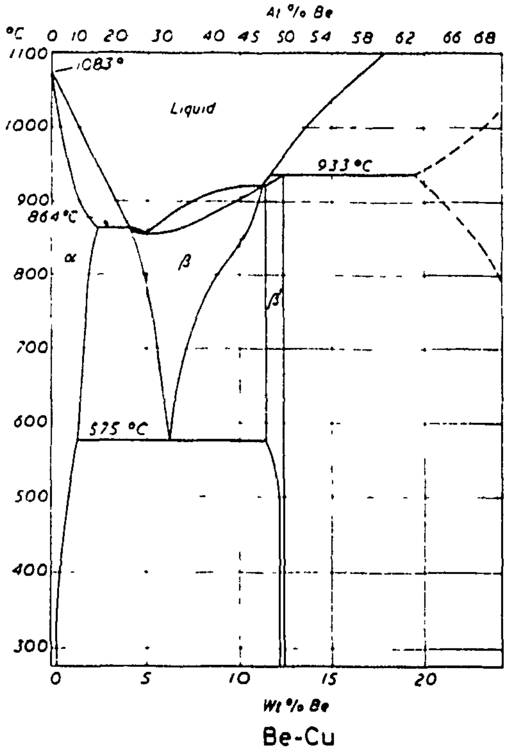

Fig. 5: Cu - Be phase diagram [6].

the higher resistivities of these alloys versus pure copper, the applied current was reduced to 40 Amperes, in order to avoid excessive heat generation within the sensing zone.

Initial experiments with Alloy 25 showed that orifices smaller than 300 µm tended to block, while those greater than 400 µm did not register a significant number of peaks for the volumes sampled. The decision was made to use orifices measuring 300-320 µm in diameter for these alloy melts.

At the start of sampling, an unduly high electronic noise would be noticed in these melts. Its source was traced to sensing zone deterioration, possibly caused by particle entrainment around the orifice entry. Passing a high current pulse (~200 Amps) by shorting the ballast resistance was found to be beneficial in recovering the reference baseline trace to the required, and expected, low levels of electronic noise.

Table 2. Chemical composition and the physical properties of the Cu-Be alloys used in LiMCA experiments(1)

Properties		Pure Copper	Alloy 3	Alloy 25	Master Alloy	Pure Beryllium
Chemical Composition, wt%	Be		0.35	1.8	3.6	100
	Co		-	0.22	0.01	
	Ni		1.6	0.08	0.03	
	Fe		N/A	0.11	0.08	
	Si		N/A	0.10	0.12	
	Al		N/A	0.06	0.03	
Mechanical Properties, MPa	Y.S.	50	550	1070		240
	U.T.S	210	700	1200		310
	F.S.†	110††	210	250		
	% el.	50	10	7		10
Melting Point or Range, °C		1083	1000-1070	870-980	(864-900)	1283
Density, kg/m^3	20°C	8960	(8830)	8360	(7830)	1848
	Liquid	8030	(8020)	8024	(7750)	1690
Resistivity, µΩm	20°C	0.017	0.069	0.101	0.140	0.033
	1100°C	0.212	0.43	0.45	(0.45)	(0.45)‡

(1) Data for pure metals are from [6], for Cu-Be alloys, from [7]. Figures in parantheses refer to estimated quantities

† Fatigue strength, 10^8 cycles †† 30% cold worked condition

‡ At its melting point

Figure 6 shows the measured number densities of BeO particles versus time. Each measurement corresponds to a data acquisition period of sixty seconds and contains an estimated sample mass of 68 grams. The figure gives a clear indication of the increase in the number density of particles caused by disturbing the metal surface with a graphite rod. Inclusion population densities dropped after prolonged periods of rest, confirming the importance of melt hydrodynamics and the avoidance of surface disturbances.

To obtain corollary information to LiMCA measurements, samples for metallographic analysis were obtained at the points indicated in Figure 6 The microstructures in Fig. 7, taken from the stirred and settled melts, respectively, consist of primary grains, a light grey interdendritic area, and darker, angular or scriptlike particles. These particles are the complex cobalt-copper-nickel beryllide

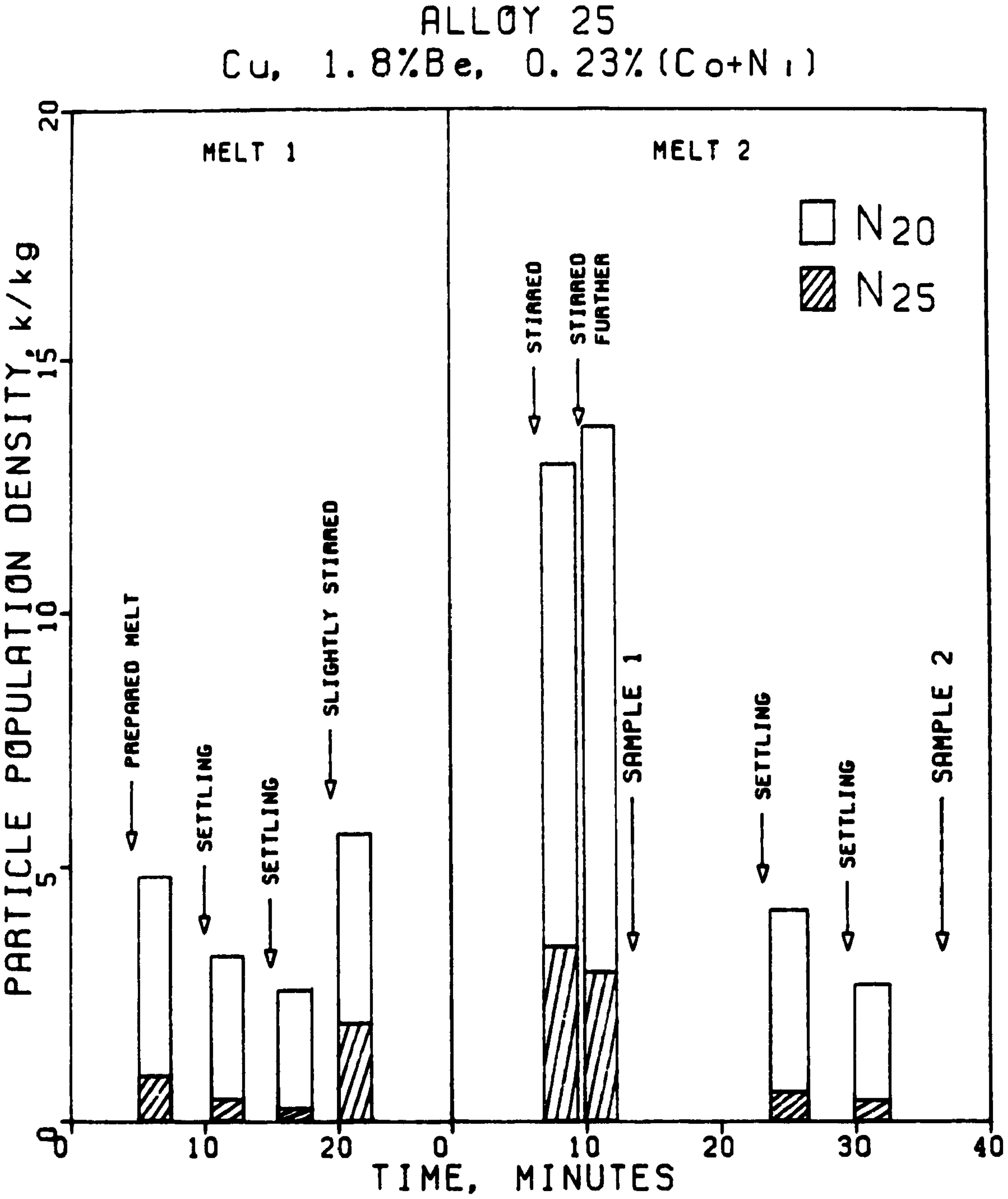

Fig. 6: Variation of inclusion population densities in Cu-Be Alloy 25 versus time, before and after stirring. N_{20} and N_{25} refer to the number of inclusions greater than 20 and 25 μm respectively.

intermetallic constituent. In color, the intermetallics appear bluish-grey and are therefore easy to distinguish from oxide particles (see Fig 8). Both sets of microstructures exhibited the same essential features, but the stirred melt had many small beryllides, whereas the settled melt had fewer but larger, intermetallic particles. This observation would point to a reduction in their rate of nucleation. At higher magnification, the stirred sample, seen in Fig. 9, contains a particle believed to be an oxide, measuring approximately 4 µm across. As seen, this particle is near a triangular intermetallic beryllide. Figures 10 and 11 show scanning electron micrographs of typical beryllide intermetallic particles and beryllium oxide inclusions, together with their energy dispersive chemical analysis. Since EDAX can estimate concentrations of those elements whose atomic numbers are greater than 10, the absence of major constituents (Be and O), make the reactive elements the only noticeble elements in the composition of oxide inclusions.

To obtain an oxide cleanness rating, prepared surfaces of 730 mm^2 were scanned at 100x magnification for oxide particles or clusters which measured greater than 10 µm across. When found, they were accurately sized and examined at 400x magnification, and were accumulated in three size intervals: 10-25 µm, 25-40 µm and greater than 40 µm. Both samples, taken from the stirred and rested melts were rated as class 1, which meant that they contained less than 3 particles in the size range 10-25 µm. In order to compare the LiMCA counts with the metallographic results, the volume size distribution was converted into an area distribution using the following relationship (see Part 2, Section 5.3):

$$N_{A_i} = N_{V_i} \cdot \frac{2}{3} d_i \qquad (4)$$

d was taken to be the larger diameter in each size interval, hence giving an overestimate in LiMCA counts per 730 mm^2. Even then, the results agreed with the metallographic counts, as shown in Table 3. Furthermore, LiMCA, owing to its large sample volume size, was able to discriminate between the two samples, whereas metallography gave the same rating. Also, Table 4 shows the relative frequencies of beryllide vs. oxide particles in Alloy 25. The counts for beryllides were taken in McGill, initially considering them to be the sought after inclusions. As seen, 3-4

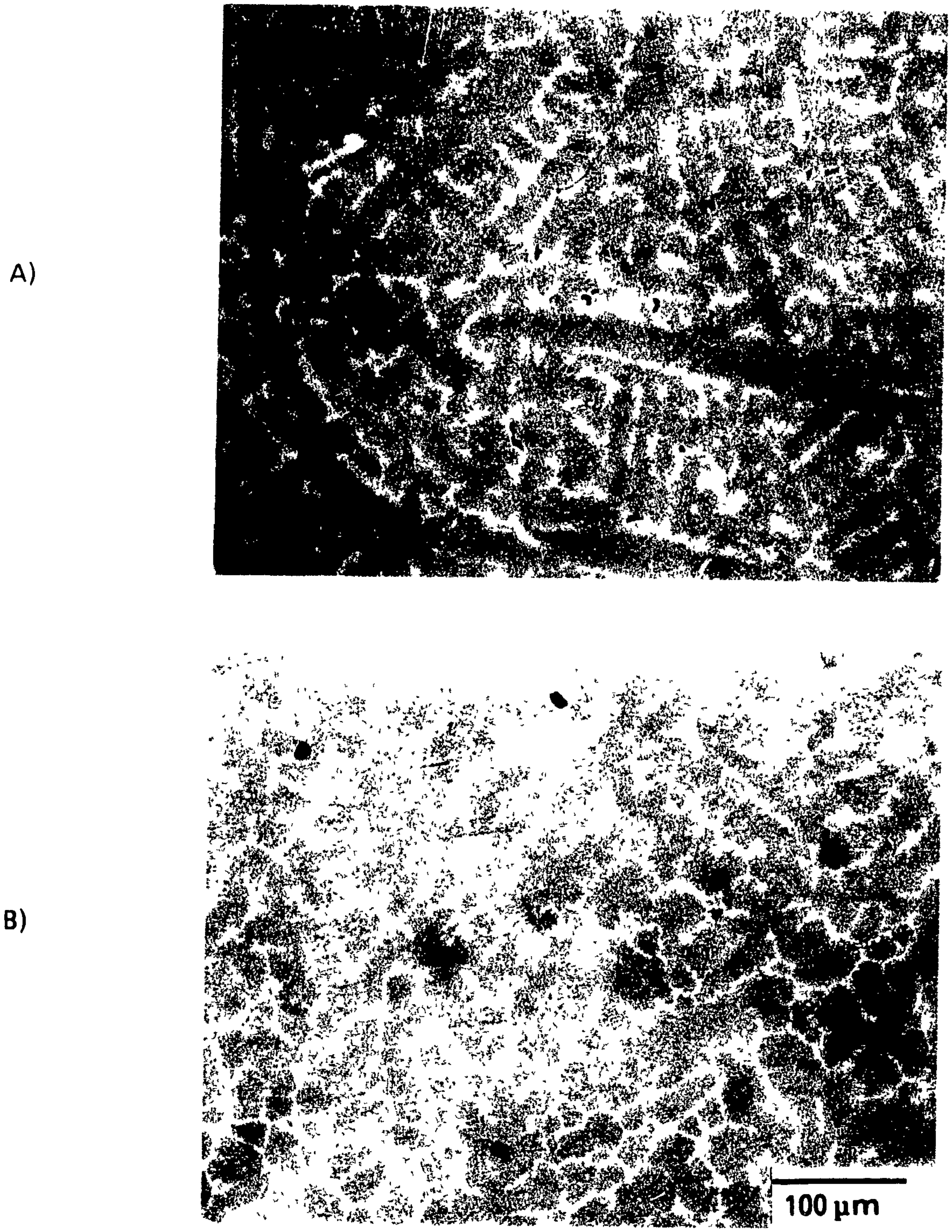

Fig. 7: Microstructures of samples taken from (A) stirred and (B) settled melts of Cu-Be Alloy 25, showing the primary grains (dominant grey area), an interdendritic phase (light grey area) and the complex intermetallic constituent (dark, angular particles).

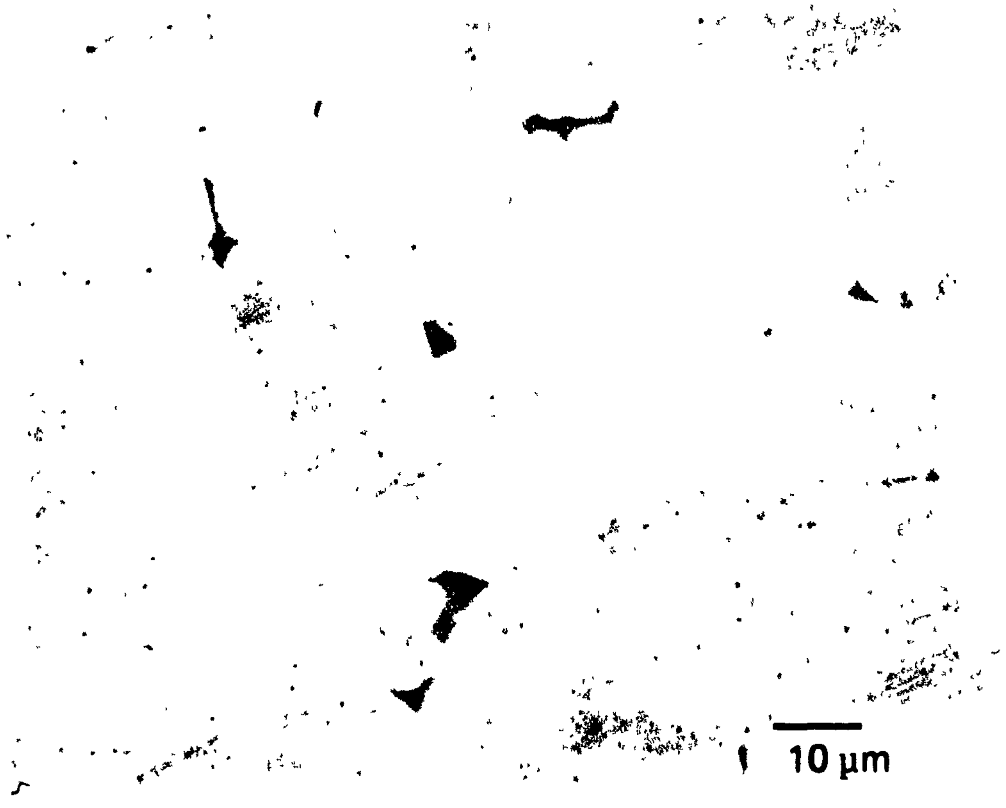

Fig. 8: Microstructure of the stirred sample in colour, at a higher magnification

orders of magnitude difference exists between the relative frequencies of beryllide vs. oxide particles. Although the large beryllides (termed the degenarate phase) are not particularly harmful to properties, it would be preferable to have them as fine precipitates within the matrix, contributing to the strengthening mechanism The content of the much fewer oxides, on the other hand, is the subject of a quality control procedure. In the auther's opinion, interfacial properties between a given phase and the metal matrix play the major role in determining why one phase is particularly more harmful to mechanical properties than another In our example, for instance, the fewer oxides, crystallographically being much less coherent than beryllides, will be the preferential sites for crack nucleation and decohesion

Fig. 9: Scanning electron micrograph of a sample drawn from Alloy 25 showing one inclusion particle (irregularly shaped dark particle in the upper portion) and one beryllide intermetallic (triangular particle below, appears bluish-grey in color).

LiMCA measurements similar to those in Alloy 25, were also made in master alloy, and Fig. 12 compares the two size distributions obtained within a four minute interval.

3.3 Stability of Silica Glass in Cu-Be Alloys

Beryllium has a strong affinity for oxygen, the oxygen potential of its oxide ranking near to that of calcium. Although no thermodynamic data for dissolved beryllium in molten copper is available in the literature, a strong negative deviation occurs in its solid solutions; an activity coefficient less than 5×10^{-4} has been suggested for dilute solutions at 800°C [8] Accepting even this low value, a few ppm Be dissolved in copper should be thermodynamically sufficient to reduce the silica glass to silicon, dissolved in the melt. The chemical stability of the silica in Alloy 25

Table 3. Comparison of Limca counts vs. metallographic examination for oxide inclusions(1).

Size Ranges	Stirred			Rested		
	Limca Counts		Metallography 730 mm^2	Limca Counts		Metallography 730 mm^2
	per 68 grams	per 730 mm^2		per 68 grams	per 730 mm^2	
20-25 µm	646	1.00	< 3	155	0.23	< 3
25-40 µm	227	0.55	-	21	0.05	-
> 40 µm	6	0.01	-	-	-	-

(1) Metallographic examination is by the courtesy of Brush Wellman Inc The first size range for the metallographic counts is 10-25 µm

Table 4. Relative frequencies of beryllide vs oxide particles.

Size Ranges	Stirred			Rested		
	Beryllides		Oxides, per 730 mm^2	Beryllides		Oxides, per 730 mm^2
	per 24 mm^2	per 730 mm^2		per 24 mm^2	per 730 mm^2	
10-25 µm	176	5353	< 3	25	760	< 3
25-40 µm	15	456	-	57	1734	-
> 40 µm	11	335	-	48	1460	-

was, however, found to be excellent. Figure 13B shows an orifice with an initial diameter of 310 µm, after an experiment. Its dimensional stability was not affected, although the surface appeared slightly etched On withdrawing the tube from molten metal, one could peel a metal-like foil from the silica surface quite readily, while underneath, the silica did not appear to have been affected by its contact.

Results with master alloy were similar, but Alloy 3, containing *less* beryllium, attacked the silica quite severely, and measurements were not possible. It is probable that a protective layer of BeO forms on silica above a critical Be concentration, while below this concentration, the next stable compound, beryllium orthosilicate, $2BeO{\cdot}SiO_2$, may form and not provide the same level protection. The data in Table 5 can be used to estimate the stability of BeO, $2BeO{\cdot}SiO_2$ and SiO_2 in Cu-Be alloys. Fig. 14 gives the BeO-SiO_2 phase diagram, which shows the three components to be mutually insoluble at the temperatures of LiMCA measurements, 1050-1150°C. Accordingly, when two adjacent oxides are in equlibrium, their activities will be unity. From the estimated equlibrium constants, K_8 and K_9, critical Be activities at 1100°C can be calculated to be:

$$h_{Be} < 0.3\times10^{-3}\sqrt{h_{Si}} \qquad SiO_2 \text{ is stable}$$

$$0.3\times10^{-3}\sqrt{h_{Si}} < h_{Be} < 0.34\times10^{-3}\sqrt{h_{Si}} \qquad 2BeO\cdot SiO_2 \text{ is stable}$$

$$h_{Be} > 0.34\times10^{-3}\sqrt{h_{Si}} \qquad BeO \text{ is stable}$$

Since equilibrium constant K_2 is a gross extrapolation at 1100°C, the above constants may be regarded as a matter of guidance for an order of magnitude analysis. Nevertheless, the analysis shows that:

i. A little Be should be sufficient to reduce SiO_2 to Si (Be activity in contact with pure Si/SiO_2 can be calculated using $\gamma^\circ_{Si} = 0.01$ [5], $h_{Si} = 100/\gamma^\circ_{Si} = 10\,000$, hence $h_{Be} = 0.03$).

ii. Beryllium orthosilicate is stable over a limited $h_{Be}\cdot h_{Si}^{-1/2}$ product range.

Beryllium and silicon activities are not necessarily the bulk activities, but rather activities at the reaction site, which may be quite different. Referring to Fig. 15,

Table 5. Data used to compare stability of beryllium oxide, beryllium orthosilicate, and silica, on silica glass surface, in contact with Cu-Be alloys(1)

i	Reaction	Log K_i
1	$\langle Be \rangle + 1/2\,(O_2) = \langle BeO \rangle$	+ 31 790 / T - 5 1
2	$\langle Be \rangle = \underline{Be}\{Cu\}$	[3 540 / T + 1 15]†
3	$\underline{Be}\{Cu\} + 1/2\,(O_2) = \langle BeO \rangle$	28 250 / T - 6 25
4	$\langle Si \rangle + (O_2) = \langle SiO_2 \rangle$	+ 47 413 / T - 9 2
5	$\langle Si \rangle = \underline{Si}\{Cu\}$	+ 634 / T - 3 21
6	$\underline{Si}\{Cu\} + 1/2\,(O_2) = \langle SiO_2 \rangle$	+ 46 780 / T - 12 4
7	$2\,\langle BeO \rangle + \langle SiO_2 \rangle = \langle 2\,BeO{\cdot}SiO_2 \rangle$	+ 570 / T - 9 2
8	$2\,\underline{Be}\{Cu\} + 2\,\langle SiO_2 \rangle = \underline{Si}\{Cu\} + \langle 2\,BeO{\cdot}SiO_2 \rangle$	10 290 / T - 0 47
9	$2\,\underline{Be}\{Cu\} + \langle 2\,BeO{\cdot}SiO_2 \rangle = \underline{Si}\{Cu\} + 4\langle BeO \rangle$	+ 9 150 / T - 0 27

(1) <solid>, {liquid}, (gas at 1 atm) ≡ pure component st states, $\underline{X} \equiv 1$ wt% st state K_1 to K_7, except K_2, are from [4].

† From $\gamma^{\circ}_{Be} = 5 \times 10^{-4}$ at 800°C Using regular solution approximation, $\bar{h}_{Be} = RT \ln(\gamma'_{Be})$ may be taken as constant Then, $\text{Log}\,K_2 = -T_0\,\text{Log}(\gamma^{\circ}_{Be})/T - \text{Log}(M_{Cu}/100\,M_{Be})$ where $T_0 = 1073$°K

once the product layer forms on the surface of the silica, copper metal must physically penetrate or the solutes Be and Si must diffuse through the layer, to bring Be to, and to remove Si from, the reaction site If a thin, coherent film that is impermeable to either Be or Si forms, the reaction will cease If the oxide film is permeable, the reaction will continue, and the film will break up periodically, to accomodate volume changes, thereby allowing Cu alloy to penetrate further to the reaction site.

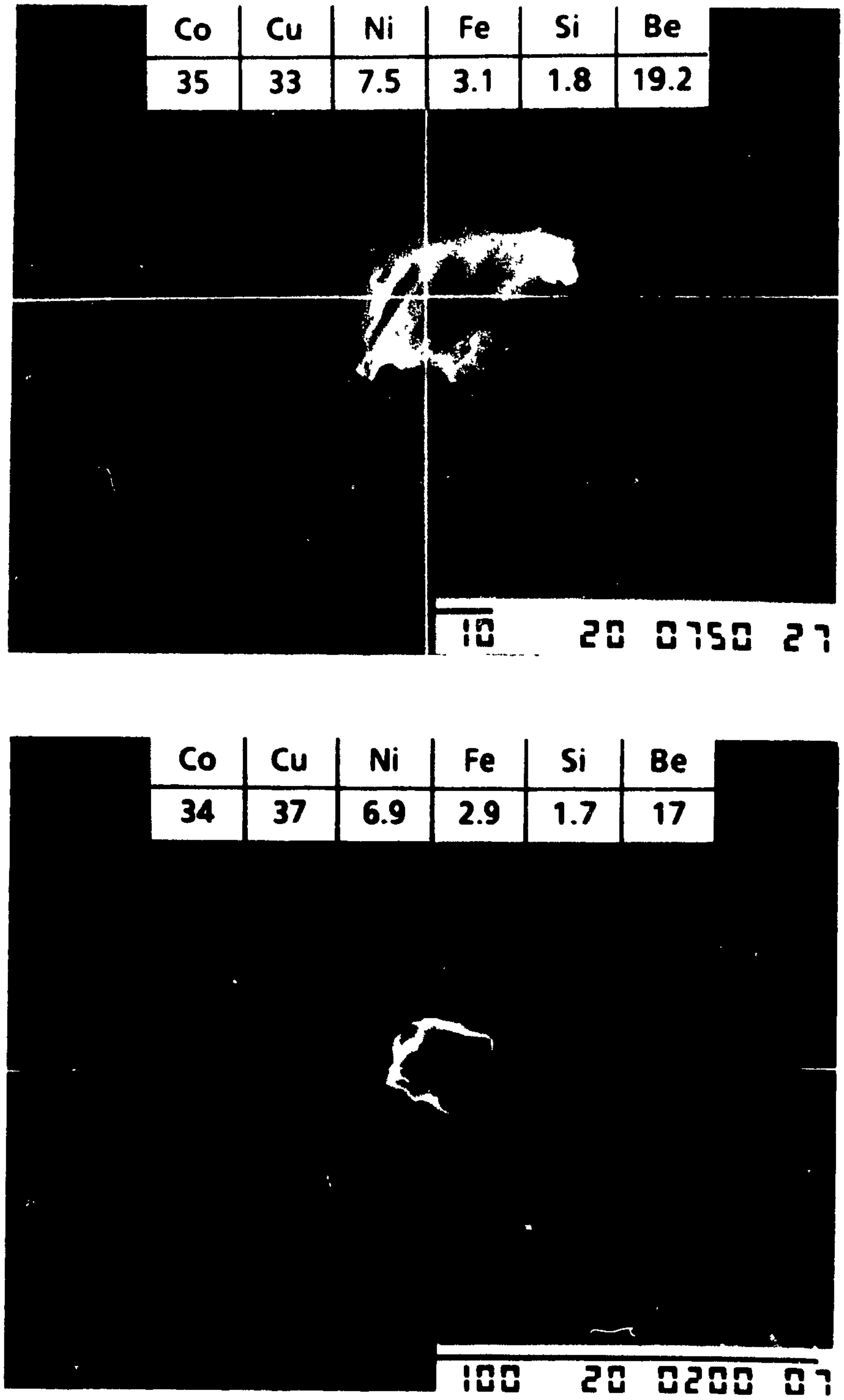

Co	Cu	Ni	Fe	Si	Be
35	33	7.5	3.1	1.8	19.2

Co	Cu	Ni	Fe	Si	Be
34	37	6.9	2.9	1.7	17

Fig. 10: Scanning electron micrograph and chemical compositions of beryllide intermetallic particles, as determined by EDAX. The figures in the box represent wt.%, the composition of Be was deduced by balance.

```
                 K
ELEMENT  I.X./I.STD.  K.RATIO       CONCFN.

  FE :        0.1147      0.0348      0.03133
  CR :        0.0006      0.0004      0.00034
  CO :        0.3801      0.3801      0.35165
  SI :        0.0920      0.0108      0.01811
  AL :        0.0001      0.0000      0.00010
  MG :        0.0000      0.0000      0.00003
  AS :        0.0005      0.0002      0.00043
  S  :        0.0017      0.0005      0.00065
  P  :        0.0006      0.0001      0.00014
  TI :        0.0000      0.0000      0.00000
  SN :        0.0000      0.0000      0.00000
  CU :        0.9921      0.3147      0.32995
  NI :        0.1038      0.0780      0.07486
  ZN :        0.0000      0.0000      0.00000

 TOTAL :                  0.81969     0.80759
 ITERATION :  3
```

```
                 K
ELEMENT  I.X./I.STD.  K.RATIO       CONCEN.

  FE :        0.1160      0.0352      0.03167
  CR :        0.0004      0.0002      0.00020
  CO :        0.3736      0.3736      0.34483
  SI :        0.0926      0.0109      0.01823
  AL :        0.0001      0.0000      0.00005
  MG :        0.0000      0.0000      0.00000
  AS :        0.0000      0.0000      0.00000
  S  :        0.0022      0.0007      0.00084
  P  :        0.0007      0.0001      0.00017
  TI :        0.0000      0.0000      0.00000
  SN :        0.0000      0.0000      0.00000
  CU :        1.0173      0.3277      0.33820
  NI :        0.1018      0.0765      0.07339
  ZN :        0.0000      0.0000      0.00000

 TOTAL :                  0.81998     0.80759
 ITERATION :  3
```

Micrograph 1

```
                 K
ELEMENT  I.X./I.STD.  K.RATIO       CONCFN.

  FE :        0.1150      0.0349      0.03137
  CR :        0.0005      0.0003      0.00029
  CO :        0.3598      0.3598      0.32942
  SI :        0.0837      0.0099      0.01653
  AL :        0.0000      0.0000      0.00000
  MG :        0.0000      0.0000      0.00000
  AS :        0.0000      0.0000      0.00000
  S  :        0.0018      0.0005      0.00068
  P  :        0.0016      0.0003      0.00037
  TI :        0.0000      0.0000      0.00000
  SN :        0.0000      0.0000      0.00000
  CU :        1.0640      0.3375      0.35326
  NI :        0.1010      0.0759      0.07266
  ZN :        0.0004      0.0002      0.00025

 TOTAL :                  0.81943     0.80482
 ITERATION :  0
```

```
                 K
ELEMENT  I.X./I.STD.  K.RATIO       CONCEN.

  FE :        0.1064      0.0323      0.02900
  CR :        0.0001      0.0001      0.00004
  CO :        0.3746      0.3746      0.34362
  SI :        0.0845      0.0100      0.01669
  AL :        0.0002      0.0001      0.00021
  MG :        0.0000      0.0000      0.00000
  AS :        0.0000      0.0000      0.00000
  S  :        0.0019      0.0006      0.00072
  P  :        0.0003      0.0001      0.00008
  TI :        0.0000      0.0000      0.00000
  SN :        0.0000      0.0000      0.00000
  CU :        1.1157      0.3539      0.37003
  NI :        0.0954      0.0718      0.06867
  ZN :        0.0000      0.0000      0.00000

 TOTAL :                  0.84329     0.82906
 ITERATION :  3
```

Micrograph 2

Fig. 10, continued: Energy dispersive X-Ray analysis of four intermetallic particles, including the two shown in the micrographs of the previous page

	Particle No.	Co	Cu	Ni	Fe	Si	Be
wt %	1	35	33	7.5	3.1	1.8	19.2
	2	34	34	7.3	3.2	1.8	19.2
	3	33	35	7.3	3.1	1.7	19.5
	4	34	37	6.9	2.9	1.7	17
mol %	1	17	15	3.6	1.6	1.8	61
	2	16.5	15.3	3.5	1.6	1.8	61
	3	15.9	15.7	3.5	1.6	1.7	61.6
	4	17.6	17.8	3.6	1.6	1.7	57.6
$Co_5Cu_5NiBe_{17}$		17.9	17.9	3.6			60.7

Fig. 10, continued: Summary of the chemical compositions of the four analysed particles, showing them to be complex cobalt-copper-nickel-beryllides of the composition $Co_5Cu_5NiBe_{17}$.

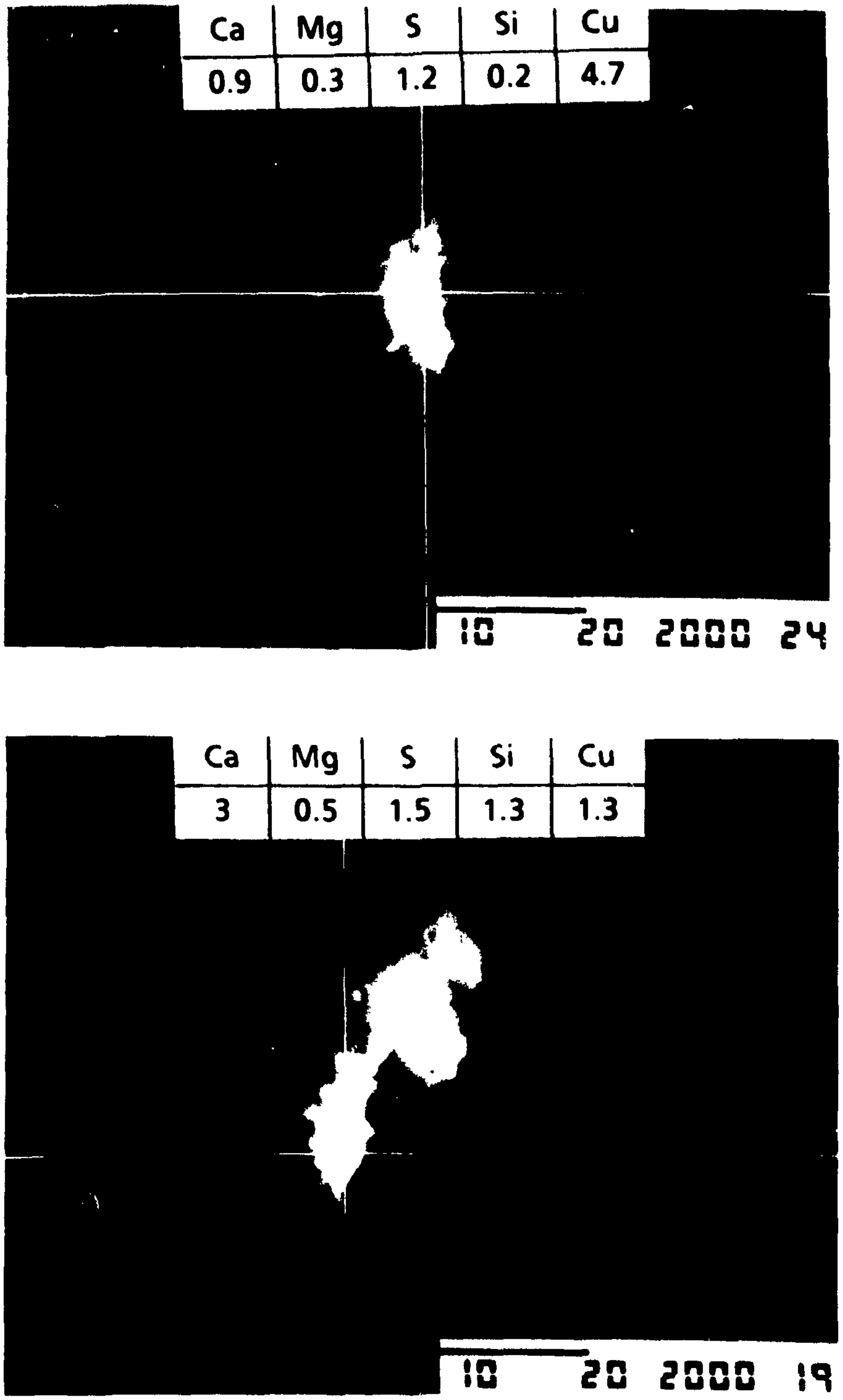

Ca	Mg	S	Si	Cu
0.9	0.3	1.2	0.2	4.7

Ca	Mg	S	Si	Cu
3	0.5	1.5	1.3	1.3

Fig. 11: Scanning electron micrograph and chemical compositions of beryllium oxide particles, as determined by EDAX. The figures in the box represent wt.%.

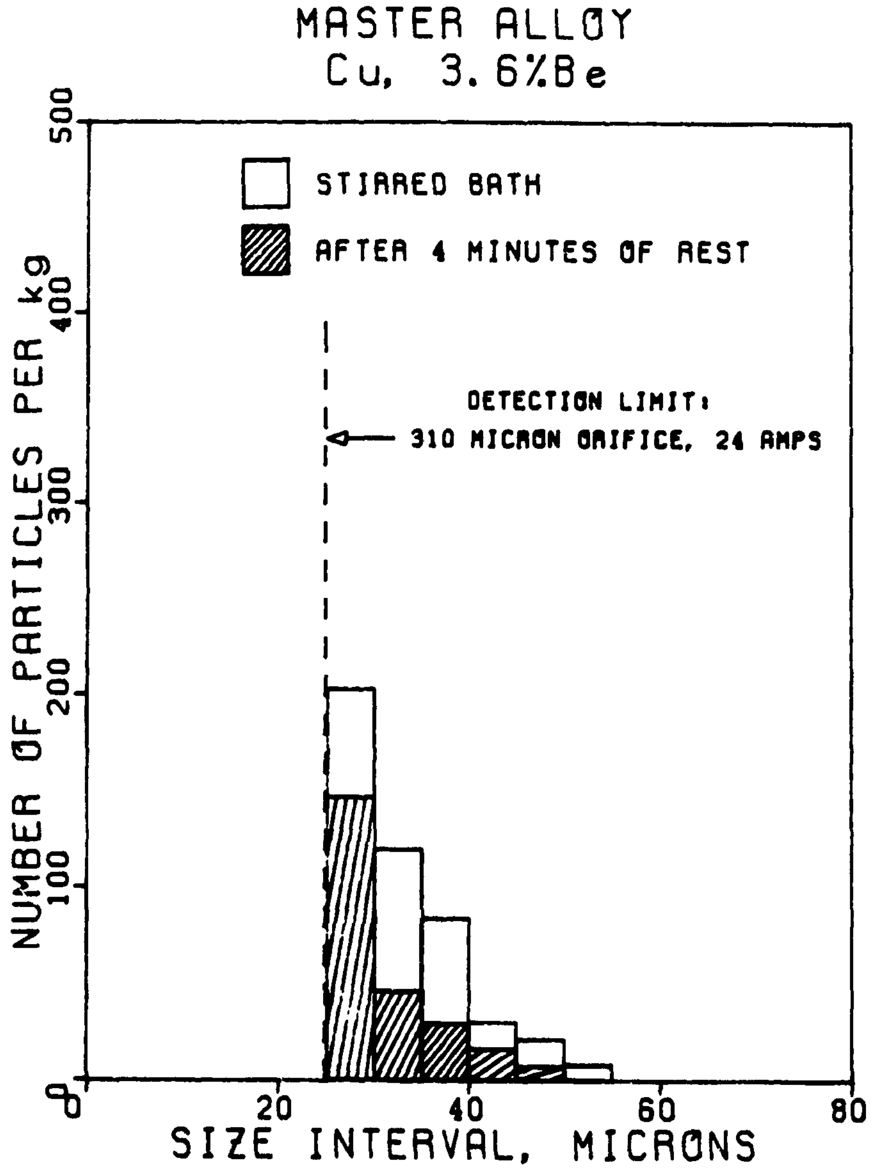

Fig. 12: Inclusion size distributions measured in Cu-Be master alloy.

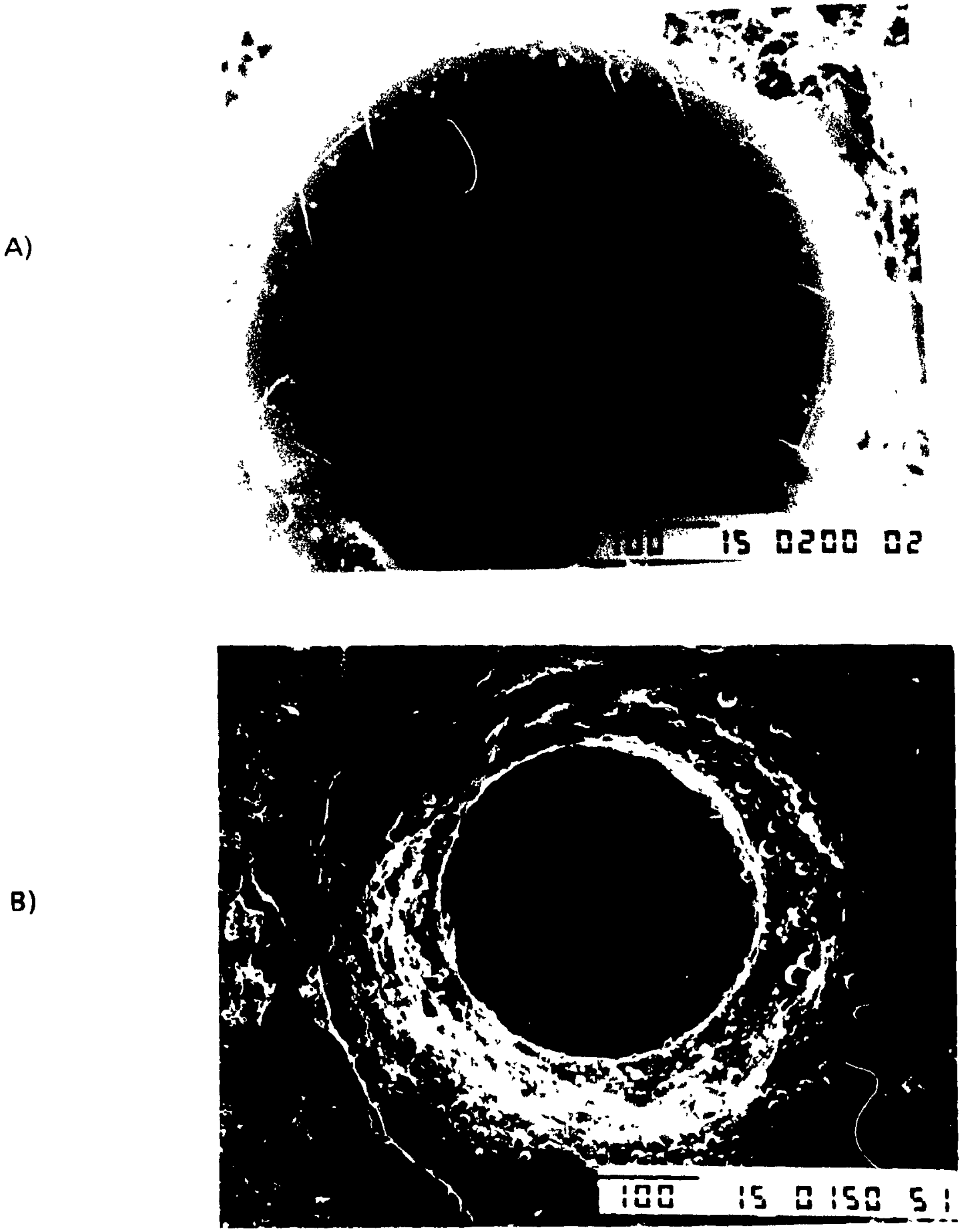

Fig. 13: Scanning electron micrograph of silica orifices after Limca experiments and after any adhering metal had been dissolved in acid, (A) 260 µm orifice in copper, (B) 310 µm orifice in Cu-Be Alloy 25

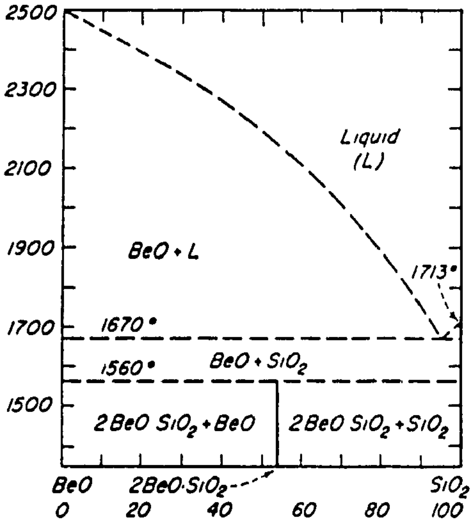

Fig. 14: SiO_2 - BeO phase diagram.

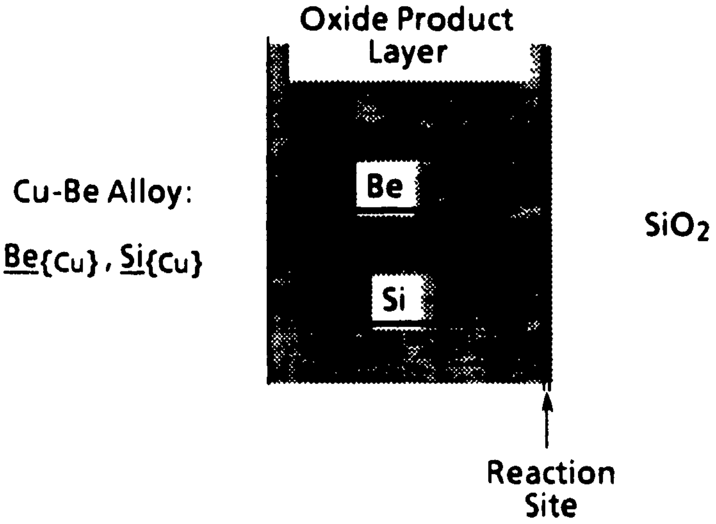

Fig. 15: Reduction of SiO_2 by $\underline{Be}\{Cu\}$.

4. CONCLUSIONS

Non-metallic inclusions in high strength copper alloys have been known to be detrimental to mechanical properties. A LiMCA probe was developed and used in Cu-Be alloys to measure the frequency distribution of beryllia particles, and the results compared favourably with the industry's standard metallographic count. In determining primary inclusions for quality control and process control applications, LiMCA would offer the advantages of increased precision (larger volume sample) and speed over the conventional metallographic methods.

The stability of the silica glass sampling tube and the orifice was found to be good in alloys containing 1.8% or more Be. This was attributed to the formation of a protective oxide layer on the surface of silica glass.

REFERENCES

1. "Standard test method for hydrogen embrittlement of copper", ASTM Designation B577-87, Copper and Copper Alloys, **02.01**, 1987.

2. "Standard specification for copper foil, strip, and sheet for printed circuits and carrier tapes", ASTM Designation B451-81, Copper and Copper Alloys, **02.01**, 1987.

3. T. B. Massalski, ed., in *Binary alloy Phase Diagrams,* ASM, Metals Park, Ohio, 1986.

4. E.T. Turkdogan, in *Physical Chemistry of High Temperature Technology,* Academic Press, New York, 1980.

5 G.K. Sigworth and J.F. Elliott, "The thermodynamics of dilute liquid copper alloys", *Can. Met. Quart.*, **13**, (3), 1974.

6 J.C. Smitthells, ed., in *Metals Reference Book,* 5th edn., Butterworths, Boston, 1976.

7. Brush Wellman Engineered Materials Data Sheets. Brush Wellman Inc., Alloy Div., 17876 St. Clair Ave., Cleveland, OH 44110.

8. R. Hultgren and P. D. Desai, In *Selected Thermodynamic Values and Phase Diagrams for Copper and Some of its Binary Alloys,* INCRA Series on the Metallurgy of Copper, No.1, Int. Copper Research Assoc., New York 1971.

List of Figures

List of Tables

PART 4: APPLICATION OF LiMCA TO LIQUID MAGNESIUM AND ITS ALLOYS

1. INTRODUCTION

In structural applications, magnesium alloys are used in moving structures where its strength to weight ratio is important. This accounts for some 16% of the total magnesium consumption (1987). Of the manufactured alloys, 70% is used in the form of pressure die castings, and presently this field has been growing at a rapid rate of 24% per year in North America (4 800 to 11 300 tpy during 1983-87) Advances that brought about hot-chamber die casting, fluxless melting, and extra corrosion resistant alloys have made magnesium die castings more attractive, and in some applications, such as parts for computer hardware, made them even competitive to plastics. Table 1 shows the trend in the structural uses of magnesium in recent years. In spite of its greater present potential (greater product integrity with reasonable cost as a result of the new developments), the predicted breakthrough in the use of die-casting alloys has been tempered by the slower growth in Europe, particularly in Germany, where the car manufacturer Volkswagen removed the Beetle, the greatest user of magnesium die cast parts, from the assembly lines early in the decade [1]

Table 1: Structural uses of magnesium in recent years, in 1000 tons [1].

	1984	1985	1986	1987	1988	1992
Die Casting	30.4	29.7	28.8	26.6	27	34
Gravity Cast	1.3	1.2	1.6	1.8	2	2
Wrought	6.6	4.8	5.4	8.4	10	8
Total Structural:	38.3	35.7	35.8	36.8	39	44
World Mg Metal Consumption	216	224.8	226.4	236	242	263

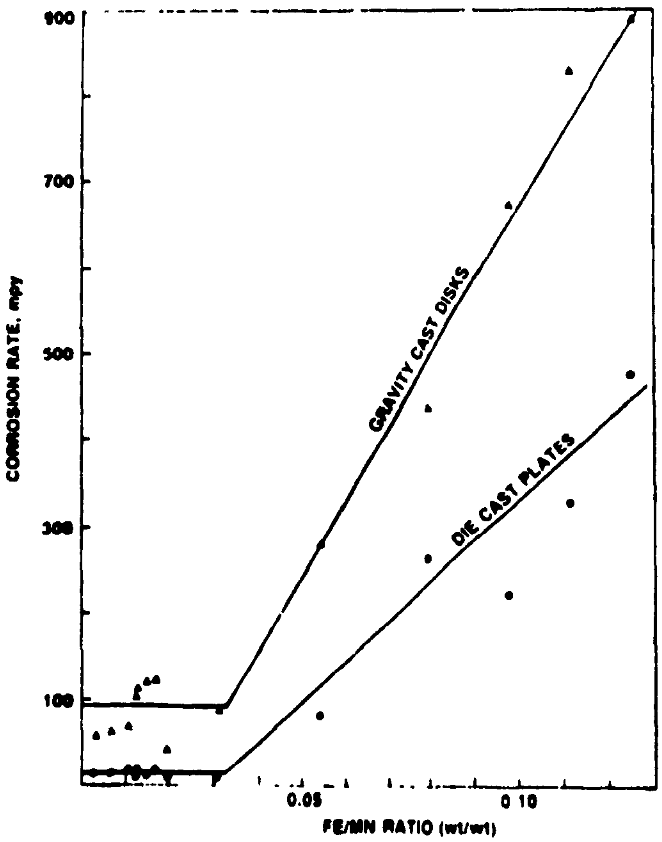

Fig. 1: Corrosion rate vs. iron content in magnesium alloy AZ91 [6].

Inclusions typically encountered in magnesium alloys are either non-metallic in character, such as those originating from salt fluxes [2], or are metallic, and originate through the precipitation of dissolved iron, nickel, or copper impurities [3-5]. The most documented effect of inclusions in magnesium alloys is a reduction in corrosion resistance. Well defined "tolerance limits" exist for the above metal impurity levels in magnesium alloys. When these limits are exceeded, corrosion in chloride containing test solutions greatly accelerates to unacceptable levels. Tolerance limits were first shown by Hanawalt and co-workers in 1942 [4], but for a long time were not incorporated critically into alloy specifications. The results were re-evaluated and confirmed in 1980's, which subsequently led to the development of corrosion resistant sand casting and die casting alloys [7,8]. From these latter evaluations, Fig. 1 shows corrosion rate vs. iron / manganese ratio in both gravity cast and die cast samples, indicating a tolerance limit for iron. Table 2 provides recommended

Table 2. Tolerance limits for iron, nickel, and copper (ppm), to prevent corrosion in different magnesium metals [4, 6, 7]

	Pure Mg	AZ91 Die Cast	AZ91 Sand Cast
Fe, max	170	50 or 0.032 x Mn	50 or 0.032 x Mn
Ni, max	5	50	10
Cu, max	1300	700	400
Mn, min., %		0.15	0.15

tolerance limits for iron, nickel, and copper in different magnesium metals The reason for this behaviour is not well understood, but at least for iron, it suggests that those metal precipitates forming in liquid magnesium can become quite harmful if trapped within the solid alloy. Aluminum, for instance, reduces the solubility of iron by forming intermetallic precipitates, and also reduces the observed tolerance limit for iron. Manganese, too, reduces the solubility of iron, but because of its beneficial effect on the iron containing intermetallic particles, higher iron contents can be tolerated with higher manganese. Therefore, the phenomenon is rather more complex than can be explained by a simple theory. It has been shown that the degree of dispersion of iron particles (i.e. their number density) is important in controlling corrosion rate [9]. Indeed, the scatter observed in the corrosion performance of magnesium alloys having similar impurity levels, could well be due to the variations in the number density of impurity particles In this regard, LiMCA could provide valuable information by measuring the number density of suspended particles in molten magnesium. In the next chapter, development of a working probe for magnesium is outlined, and in the following, LiMCA measurements made in industrial alloys and their correlation to alloy properties are presented

2. PRELIMINARY WORK

As iron has a very limited solubility in molten magnesium (180 ppm at its melting point), it is common practice to use equipment made of steel to contain and manipulate magnesium melts. Expectedly, steel would also be a good candidate as electrode material. However, owing to magnesium's very low oxygen potential (see Fig.2), the second task of finding a chemically stable, electrically insulating, refractory material for the sampling tube proved difficult.

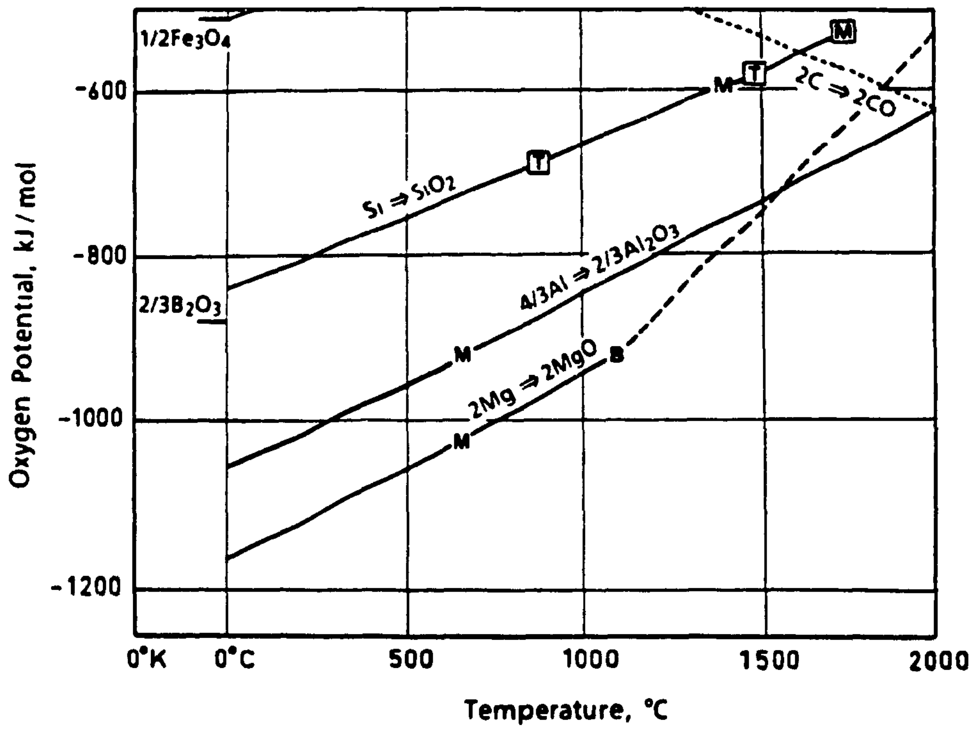

Fig. 2: Oxygen potential vs. temperature, of MgO and other oxides of interest.

Approximately 6 kg of unalloyed magnesium was remelted in a steel crucible, under a cover, with a protective gas atmosphere (CO_2, 0.6% SF_6). During these LiMCA experiments, the melt temperature was maintained at 700 ± 10°C. Once the cover was removed for probe insertion, a protective atmosphere could not be maintained, surface ignition of the melt was then controlled by using a propriety flux, M4™, consisting of a mixture of halides.

2.1 Construction of the First LiMCA Probe for Magnesium

Independent electrode tests (see Part 1, Section 3.5.1) showed that bare steel rods could be used as electrodes without any problem. For sampling tube construction, since molten magnesium dissolved all borosilicate, aluminum silicate, and silica glass tubes, boron nitride, a very stable material under reducing atmosphere conditions, was chosen. The orifice was contained in an 8 mm BN insert, suitably countersunk on both sides. This insert was screwed into the side of a sampling tube and cemented in place. Orifices as small as 220 µm diameter were used. They exhibited good dimensional stability, as measured under a microscope before and after an experiment (± 10 µm). It was possible to aspirate molten metal samples in pure magnesium using a partial vacuum of only 4-6 cm Hg, and under an electric current of 40 Amperes. Fig. 3A shows the stability of the baseline typically achieved, together with an example of a resistive pulse obtained in this metal.

2.2 Effect of Electrically Conducting Particles

As intermetallic particles contained in magnesium alloys have finite electrical conductances, it would be anticipated that their resistive voltage pulses would be lower than those predicted by eqn. 12, in Part 1, which strictly applies for an insulating particle. According to DeBlois and Bean [10], the following equation is appropriate for conducting particles:

$$\Delta V = \Delta V^{ins.\,particle}.\ \left(\frac{2-2k}{2+k}\right) \tag{1}$$

where k is the ratio of the molten metal's resistivity to the particle's resistivity. As an example, for iron particles at 650°C ($\rho_{Fe} = 0.7\ \mu\Omega$ m), in molten magnesium ($\rho_{Mg} = 0.28\ \mu\Omega$ m), $k = 0.4$, and pulse heights would be reduced by half However, the effect on calculating particle size from pulse height information would be less, owing to the cube root relationship between the particle diameter and the signal voltage. In the above example, for instance, if iron particles were considered as electrically insulating, their size would be underestimated by only 20% of their actual size.

In the following chapter, in converting pulse height information to particle diameters for the two different magnesium alloys, particles were treated as being electrically insulating. This was necessary, not only because of a lack of information on the type of particles being counted, but also because of the uncertainty of whether the electric field penetrates the intermetallic particles themselves. In LiMCA's first application to aluminum, for instance, TiB_2's, indigeneous particles formed in molten aluminum, were observed to behave in the manner of insulated particles, although they were electrically more conducting than aluminum [11]. This is not true for all solid particles, however, aluminum crystals solidifying in molten aluminum for example, give negative peaks.

2.3 Use of a Silica Sampling Tube in Magnesium

Since sampling tubes made of BN were expensive, to reduce their cost, 40 mm dia., 300 mm long, 5 mm thick wall, Masrock™ tubes were tried in their place. Table 3 gives the properties of Masrock™ tubing. These were available in $\frac{1}{2}$" thick walls.

Table 3. Properties of Masrock™ tubing [17].

	R.T.	100	400	800°C
Chemical Analysis, % SiO_2	99.63			
Al_2O_3	0.25			
Porosity	11-25			
Density, kg/m^3	1840			
Coeff of linear thermal expansion, °C^{-1}		0.4×10^{-6}		
Thermal conductivity, W/m °C		0.8	0.87	1.0
Heat capacity, J/kg °C	1044			
Thermal diffusivity, m^2/s		0.4×10^{-6}		0.5×10^{-6}

To reduce the wall thickness to $\frac{1}{4}$", a water-cooled diamond core drill was rigged to a lathe and the tubes were drilled to 30 mm ID. This was necessary, not only to have a larger chamber volume, but also to keep the preheating time of the tubes in the melt reasonably short. To prevent metal freezing in the tube, the first aspiration was made after the inside wall temperature of the tube reached the melting point of magnesium. Required preheat times between insertion of the probe and the start of sampling, were estimated as follows. since the Biot number for molten magnesium and a Masrock tube system is large ($Bi = hL/k$, $h > 4000$ W/m^2 °C for molten magnesium under natural convection, $L \cong 0.005$ m, $k = 1$ W/m °C for Masrock™, hence, $Bi > 20$), the outside wall may be considered to have a constant wall temperature. Considering inside wall to be insulated, and solving for a slab, for the typical superheats, with the aid of Heisler charts (θ vs. Fo):

$$\theta = \frac{T_{mp} - T_{\infty}}{T_{melt} - T_{\infty}} = \frac{650 - 700 \pm 10}{25 - 700 \pm 10} = 0.07 \pm 0.01$$

$$Fo = \frac{\alpha t}{L^2} = 1.2 \pm 0.1$$

Hence, the preheat times for different wall thicknesses were calculated to be:

Wall thickness	Time
5 mm	1 min.
12 mm	>5 min.

During the preheating period, argon gas was bubbled through the orifice in order to prevent its blockage, similarly, prior to probe insertion into molten metal, the tube's atmosphere was displaced with argon. For argon delivered at 5 psi (35 kPa), a 6 min. purge period was sufficient to reduce the oxygen partial pressure to very low values. For a 200 μm orifice, for instance, and assuming the worst possible case of complete backmixing, partial pressure of oxygen remaining in the tube could be calculated to be of the order of 10^{-6} atmospheres.

Although Masrock™ is a glassy silica like fused silica glass, it has an opaque, porous structure, and was not consumed by magnesium to any great extent owing to its thick wall, and the build up of MgO scale around it. The cost of a Masrock™

sampling tube fitted with a BN insert for orifice was about CD$ 20 vs. $ 500 for BN sampling tube fitted with a silica glass extension

3. EXPERIMENTS IN INDUSTRIAL ALLOYS

The two casting alloys studied were ZE41 and AZ91, supplied by Haley Industries, Ontario. Their nominal compositions and melting (liquidus) points are given in Table 4. LiMCA readings and parallel solid samples were taken after puddling, degassing and settling operations, in order to correlate alloy properties to their population densities of suspended particles.

Table 4. Chemical compositions of the ZE41 and AZ91 ingots used, and the aimed composition in the castings of these alloys(1).

Element, %	ZE41		AZ91	
	Ingot	Casting	Ingot	Casting
Al	-	-	8.8	8.1-9.3
Zn	4.3	3.5-5.0	0.7	0.4-1.0
Zr	0.5	0.4-1.0	-	-
R.E.	1.2	0.8-1.8	-	-
Mn	<0.03	<0.15	0.24	>0.10
Fe	<0.003	<0.01	<0.005	
Ni	Ni + Cu:		<0.001	<0.01
Cu	<0.01		<0.001	<0.1
Si	<0.01		<0.005	<0.3
Ca			<0.001	Ca + Pb + Sn:
Pb + Sn			<0.001	<0.1
m.p., °C	640		600	

(1) Data supplied, courtesy of Haley Industries, Ontario

3.1 Alloy ZE41

Nominally, this is a Mg, 4% Zn, 1% R.E., 0.6% Zr alloy that has good creep resistance up to 250°C. It is widely used for castings exposed to elevated temperatures, such as aircraft engine components. The grain refining action of zirconium makes it possible to use zinc as a precipitation hardening agent, zinc having a high solid solubility (> 8% near eutectic temperature) in magnesium. Rare earth additions precipitate at grain boundaries as intermetallic compounds This prevents grain boundary sliding as a creep mechanism, thereby imparting ZE41's high temperature strength. Zirconium also scavenges H, Fe, and Si impurities from molten magnesium by forming intermetallic compounds Removal of hydrogen from solution results in sounder castings as a result of reduced microporosity The removal of iron and silicon from solution, and their eventual physical separation, also results in improved corrosion resistance.

Suspended particles in molten ZE41 alloy, therefore, consist of intermetallic compounds of zirconium, and if solid flux is used, also flux particles of halide compounds. The number density of these particles remaining in ZE41 would be expected to have a controlling effect on the corrosion resistance of this alloy, and also possibly to have some effect on its mechanical properties.

For LiMCA measurements, ZE41 alloy was remelted following a similar procedure to that given for pure magnesium melts. After melt-down, the recommended proprietary flux HE™, containing 36% $CaCl_2$, 14% KCl, 22% NaCl and 28% MgF_2, was used.

During the first two experiments, the orifices, drilled into BN inserts, which were then set in sampling tubes made of a machinable silica ceramic (Masrock™, consistantly blocked. It was presumed that this was caused by insufficient preheating of the sampling tube, in view of its thick wall. This was overcome and LiMCA measurements were eventually made with a 220 µm diameter orifice, the alloy having been remelted for a third time. LiMCA samples were taken 50 mm below the molten metal surface, while maintaining a current of 40 Amperes. Data acquisitions were carried out for periods of 60 seconds, each of which corresponded to calculated 10 g metal samples. Fig. 3 shows oscilloscope traces of voltage pulses recorded in this alloy, while the bar chart in Fig. 5 gives the number density of particles detected versus time. When the metal was at rest, within the first 20 minutes, consistently low readings were taken during the 60 s measurements However, once when the metal was stirred, the particle population density increased by more than two orders of magnitude. This reading then settled to lower values over the next 45 minutes Fig. 4 shows the multichannel analyser histograms of the particle populations during the settling period, corresponding to the bars after stirring, in Fig. 5. The settling rate observed suggested an exponential decay of the form:

$$\frac{N_t - N_f}{N_i - N_f} = exp\,(-\frac{t}{t_0}) \tag{2}$$

where N_t population density of particles at time t, kg^{-1}, N_i and N_f initial and final population densities, t_0 time constant, min. From the bar chart, the time constant for particles greater than 15 µm, and also for particles greater than 20 µm were about the same, and in the region of 10 min.

The next step was to take solid samples for mechanical testing, corrosion testing and metallographic analysis, in conjunction with Limca measurements. For this purpose, an attempt was made to draw test bar samples by aspirating the alloy into a steel pipe. Because of the difficulty of removing a solid sample from the sampling pipe, later in another experiment, pyrex tubing was used. However, sample bars obtained by aspiration, contained excessive porosity and did not give useful mechanical test results.

Figure 6 shows the Limca measurements, and attempts for taking test bar samples in these experiments. Each time ZE41 was poured into an ingot at the end of an experiment, a thick sludge was formed at the bottom of the crucible containing the settled particles Because of this loss, approximately 20-25% fresh alloy would be added to the remelted ingots. A chemical analysis was made on the solid samples acquired during the 5th remelt, this and the initial composition of the alloy are shown in Table 5.

A significant loss of zirconium and rare earths indicates that precipitation of zirconium by iron and hydrogen, and oxidation of rare earth metals must have

A)

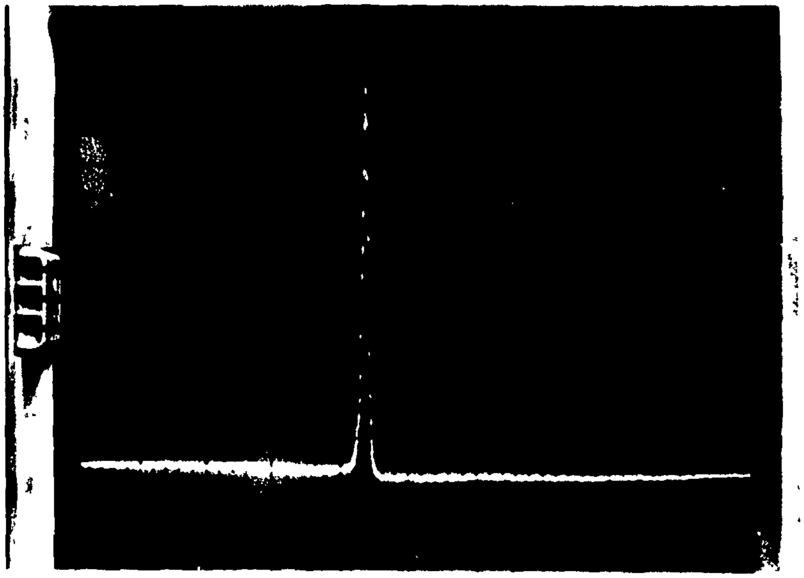

B)

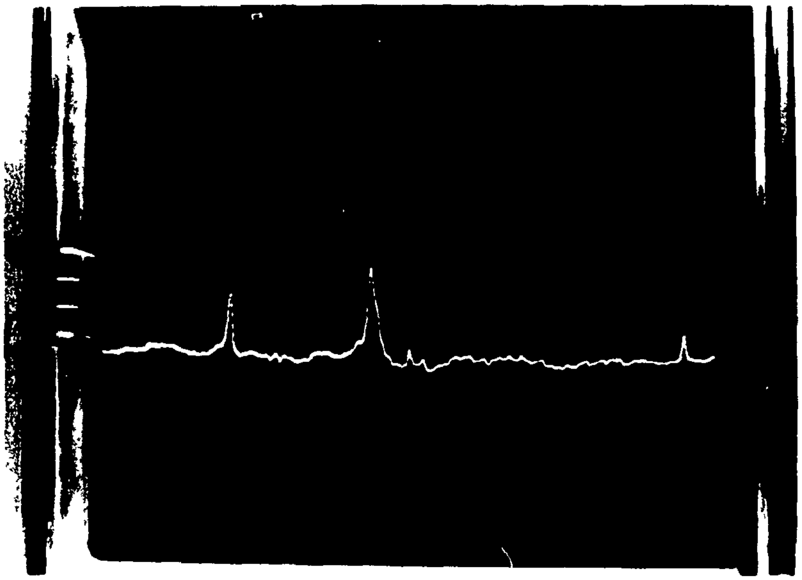

Fig. 3 : Oscilloscope traces of the peaks recorded in pure magnesium (A) and in ZE41 (B).

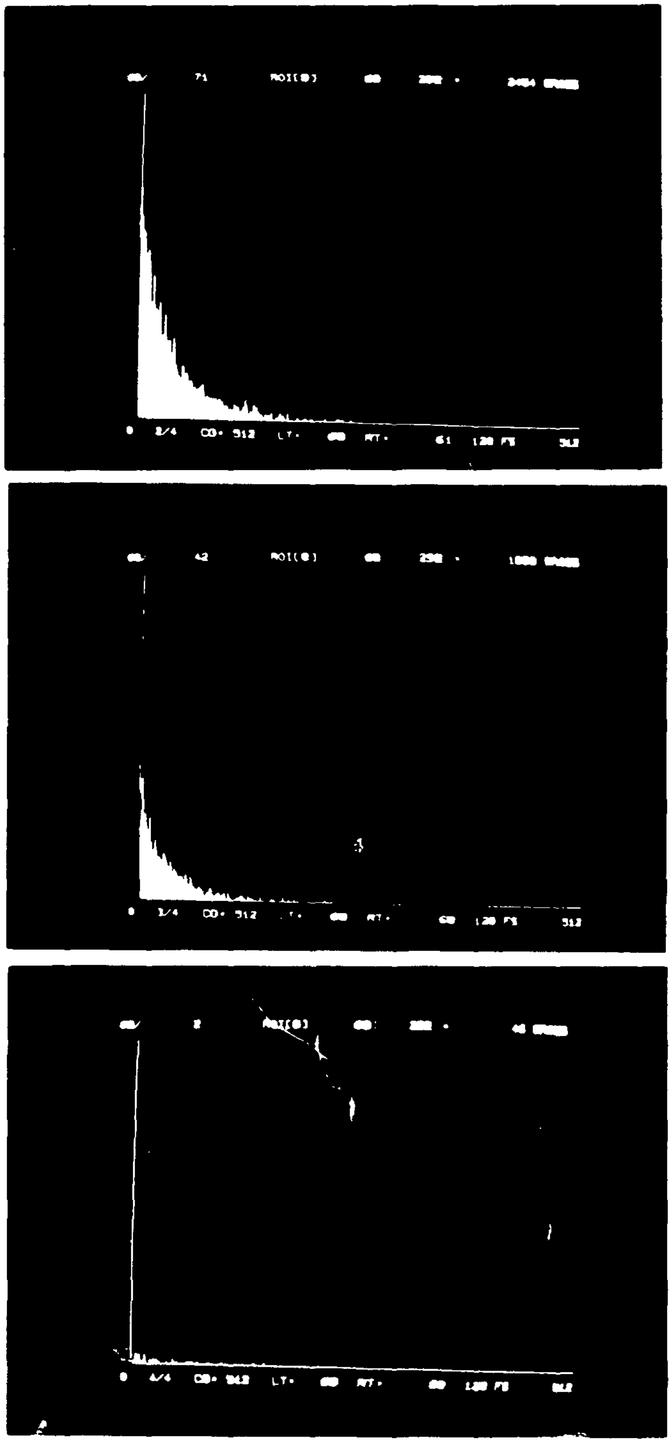

Fig. 4 : Pulse height distributions recorded by the M.C.A. after stirring (top), and during settling of ZE41.

Table 5. Initial and final compositions of the ZE41 alloy during lab melts

	Zn	Zr	R E	Mn	Fe	Ni + Cu	Si
Initial	4.3	0.5	1.2	<0.03	<0.003	<0.01	<0.01
Final	4.4	0.2	0.6		nil		

occurred during the course of these experiments. With the loss of zirconium, the total number of inclusions in the stirred melts decreased, as shown in Fig 7 Most Limca counts, therefore, must have belonged to these undesirable zirconium containing intermetallic particles.

It was, therefore, necessary to adjust the composition of remelted alloys for Zr and rare earth metals in order to bring the alloy to specification, or to start with a fresh charge each time It was also necesary to take gravity cast sample bars for mechanical testing with sufficiently long risers and gates Taking these samples each time, however, would require approximately 4 kg of metal, and was impractical in a laboratory where small amounts were being remelted

Experiments were then scheduled in a plant environment, using a gas fired furnace, equipped with a steel crucible to hold 200 kg of magnesium alloy However, in these experiments, both after puddling and after a 40 minute period of settling, LiMCA orifices measuring 250 and 300 µm blocked rapidly and measurements were not possible. It was concluded that this was due to the high particle population density in a freshly prepared alloy. These results were consistant with the earlier blockages that had occurred in the lab remelts. Although the individual particles themselves were much smaller than 300 µm, their high rate of coincidence at the orifice leads to accumulation at the orifice walls, and to blocked orifices Gravity cast test bars, nevertheless, were taken: the effect that settling has on the physical properties of ZE41 alloy will be described in Section 3.3

Fig. 9A shows the stirred alloy's microstructure, which consists of small equiaxed grains and Mg, R.E., Zn eutectic at the grain boundaries Fig. 9B shows a particle subjected to EDAX and was found to be rich in Zr and Fe It is highly likely that this particle was a solid intermetallic in molten magnesium, as ZE41 exhibits a highly cored structure for the distribution of zirconium. During solidification, a zirconium rich core first precipitates peritectically to provide numerous, crystallographically coherent nucleation sites for magnesium, giving rise to the alloy's fine grain size. As the particle in Fig 9B was lodged between the grains, it was not part of this coring.

The microstructure of the settled melt was essentially the same. This is because the expected number density of particles in the molten magnesium was too low to make a difference on a single frame of a magnified section. At 250x magnification, for instance, the area of a single frame is 0.16 mm^2. If all the iron in this alloy were present as $FeZr_2$ particles ($\rho_{FeZr_2} = 8\ 000$ vs. $\rho_{Mg} = 1\ 600$ kg/m^3), having an average diameter of 4 µm, then there would be, on average, 1 particle per 2.5 frames in the stirred alloy (50 ppm Fe), and 1 particle per 4 frames in the settled alloy (30 ppm Fe). Particles greater than 15 µm were measured by LiMCA to be 300 and 3.5 g^{-1}, and their corresponding frequencies of occurence in the microphotographs would be 1 particle per 1 000 and 8 500 frames in the stirred and settled alloys, respectively!

3.2 Alloy AZ91

The first class of structural magnesium alloys having reasonably fine grain size and the possibility for precipitation hardening were made up with aluminum, zinc and a small amount of manganese. Their economy of manufacture still makes them the workhorse alloy for most mass produced components, such as those used in the automotive industry. Their corrosion resistance depends strongly on their metallic (Fe, Ni, Cu), and halide flux impurity level. Nominally, AZ91 contains 9% Al, 1% Zn and 0.1-0.3% Mn. The primary function of Mn is to remove iron or to make its cathodic action less effective when trapped in the alloy, by forming Mn-Al intermetallic particles that also incorporate iron in solid solution. Therefore, similar to ZE41, suspended particles in AZ91 would also consist of intermetallic compounds and possibly flux particles, whose number density should be important in controlling its corrosion resistance.

Because of the need to take gravity cast samples, this alloy was tested with LiMCA in a plant environment only Figure 8 shows Limca measurements after grain refiner addition and degassing, and during a 40 minute settling period. In comparison to ZE41, particle concentrations in the stirred alloy in this melt was much less. Referring

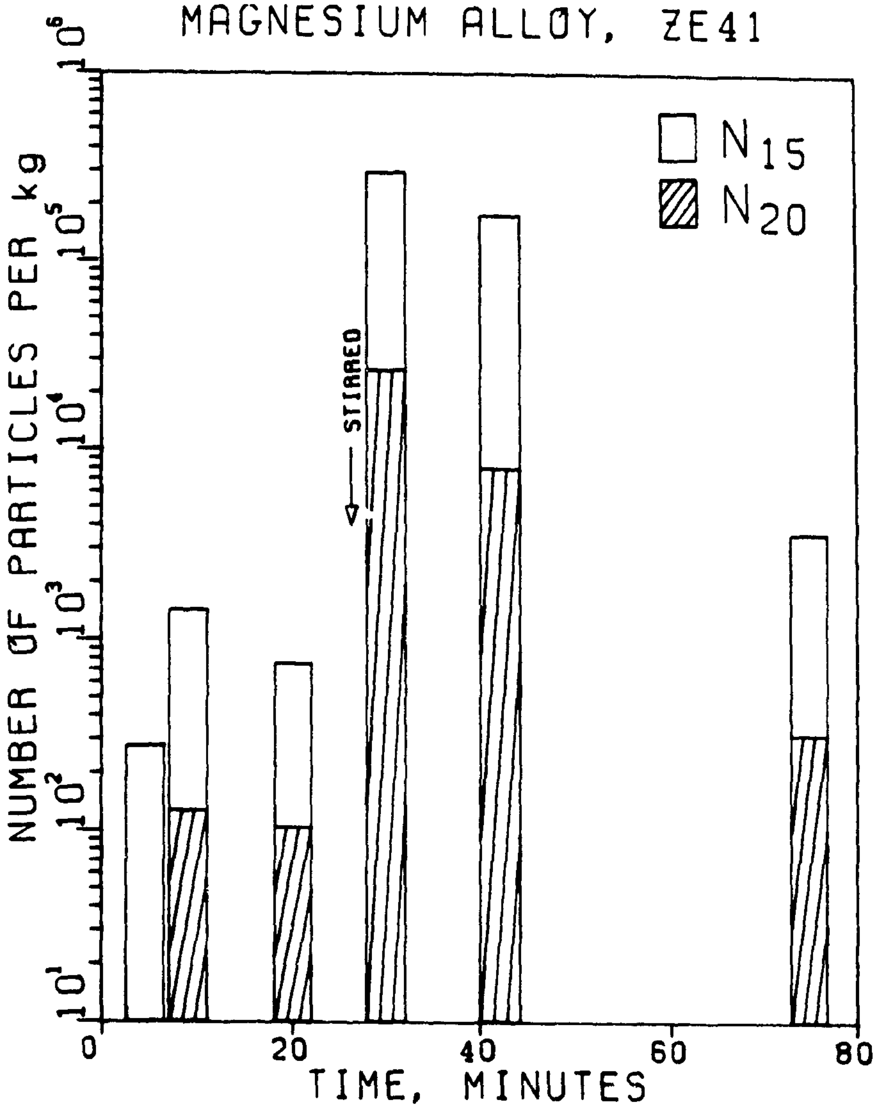

Fig. 5: Variations of the particle population densities measured by LiMCA, in a 6 kg batch of ZE41 alloy, versus melt holding time, before and after stirring N_{20} and N_{25} refer to the number of particles greater than 20 and 25 μm respectively. Hence, the white area in the bars are the population density of particles in the size range 20-25 μm.

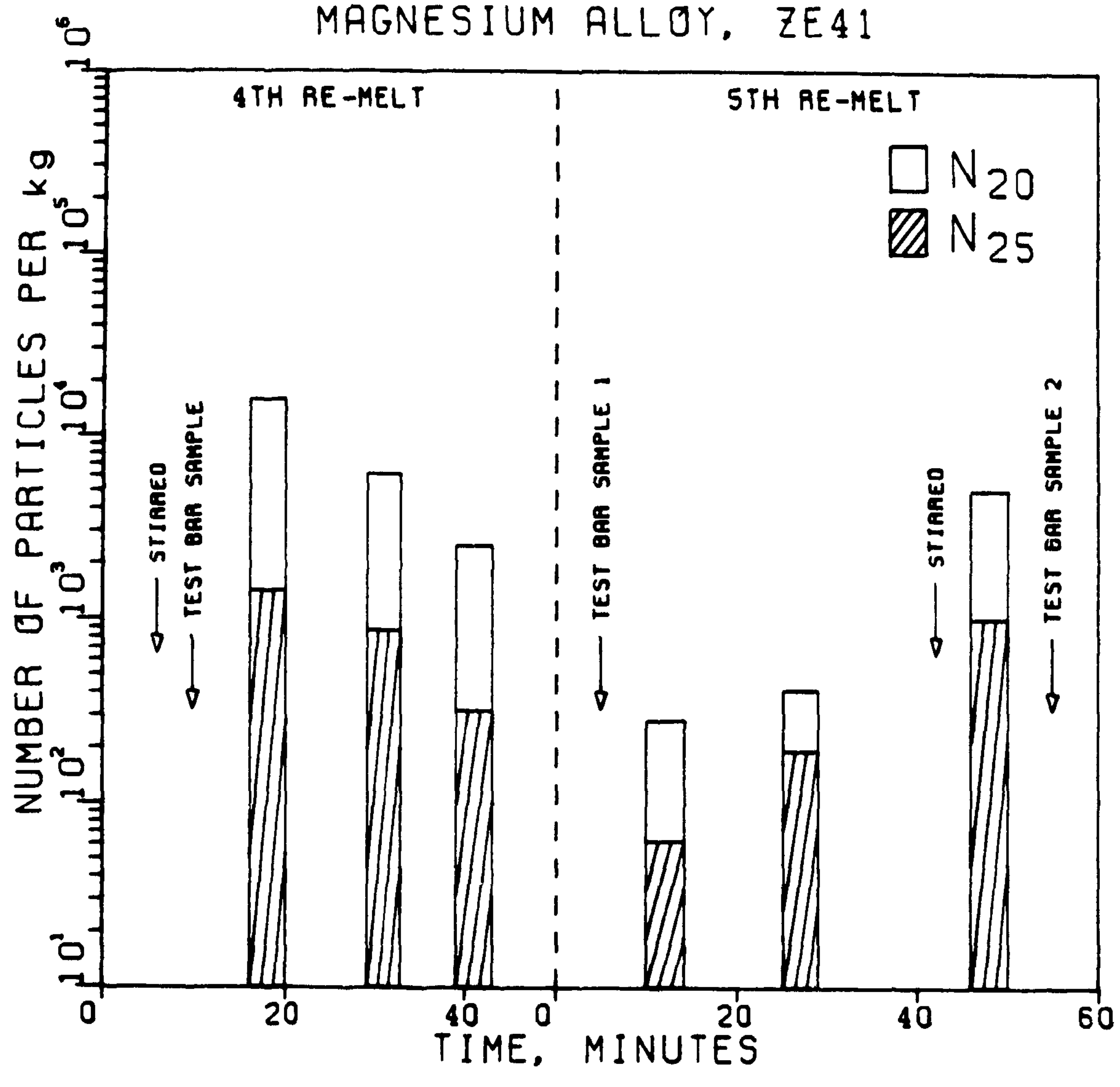

Fig. 6. Subsequent re-melts of ZE41 alloy. Graph shows attempts for test bar samples, condition of melt and LiMCA measurements

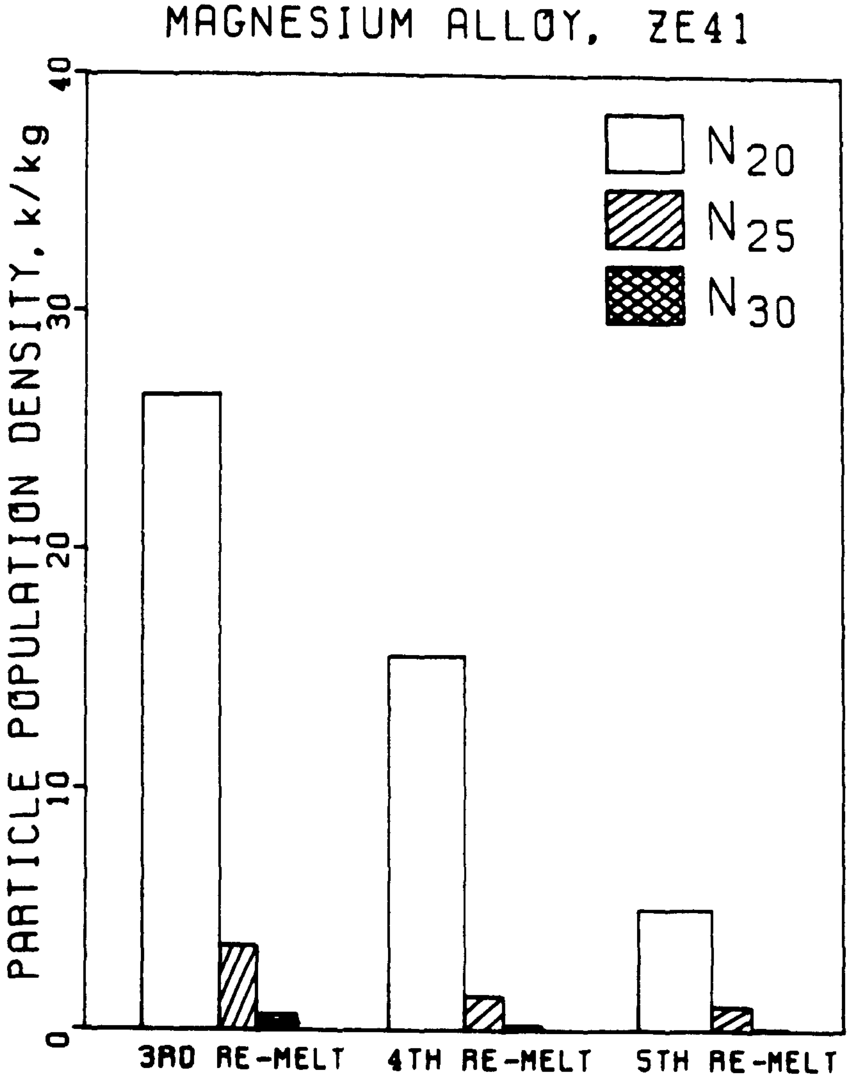

Fig. 7: Particle population densities in the stirred melts of ZE41, showing the decline in the total number of suspended particles, as the same ingot was remelted for lab experiments

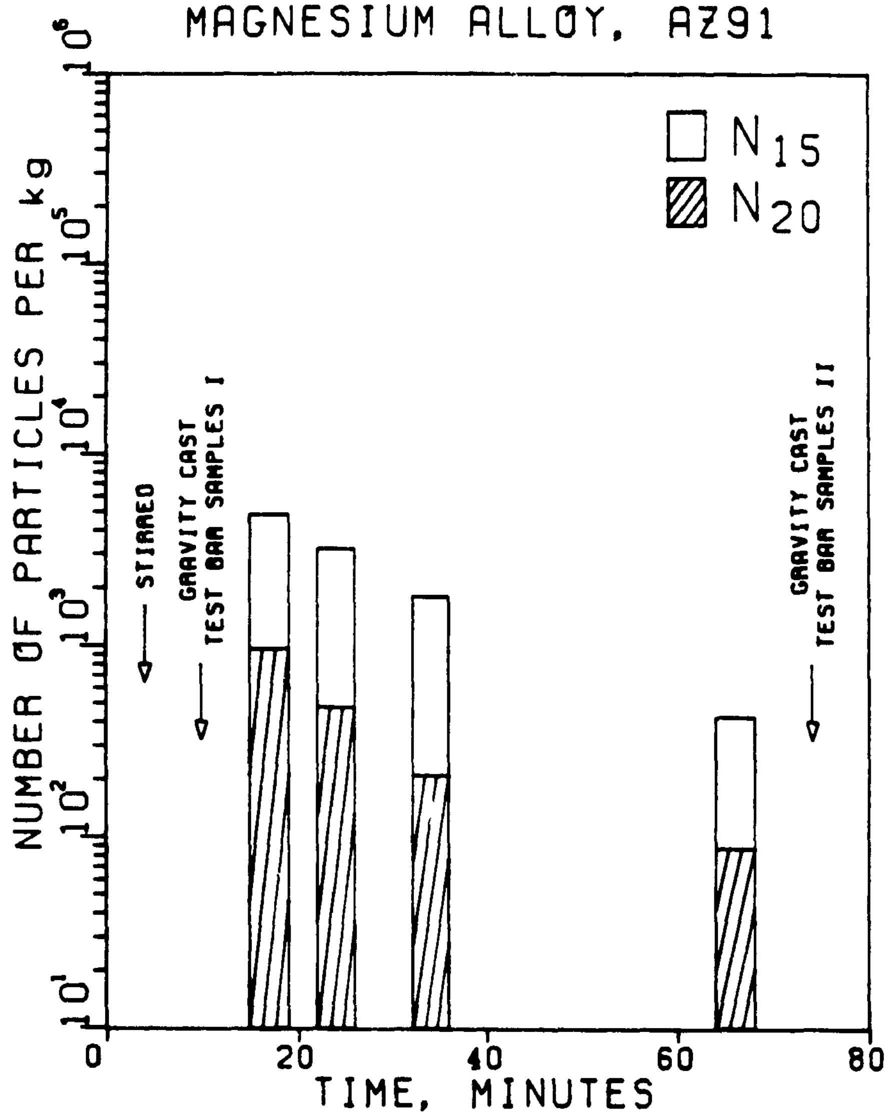

Fig. 8: Limca measurements in a plant environment and acquisition of test bar samples, I and II, versus melt holding time, in a 200 kg AZ91 alloy. 'Stirred' arrow refers to the time when grain refiner addition and degassing was made

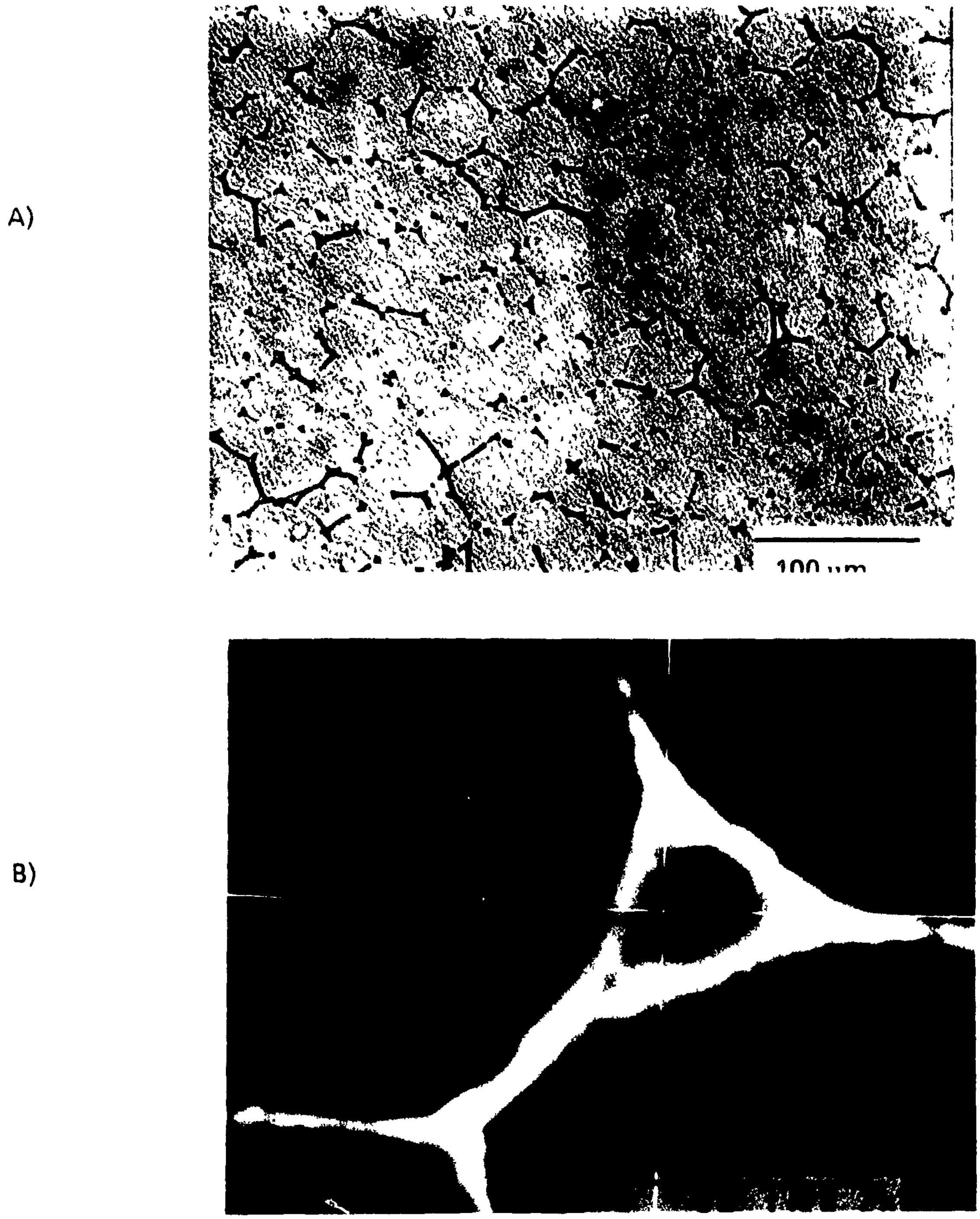

Fig 9: Microstructure of ZE41 (A) General structure fine equiaxed primary grains and Mg, R E., Zn rich eutectic at the grain boundaries (B) Impurity (Fe, Si) rich zirconium intermetalic particle

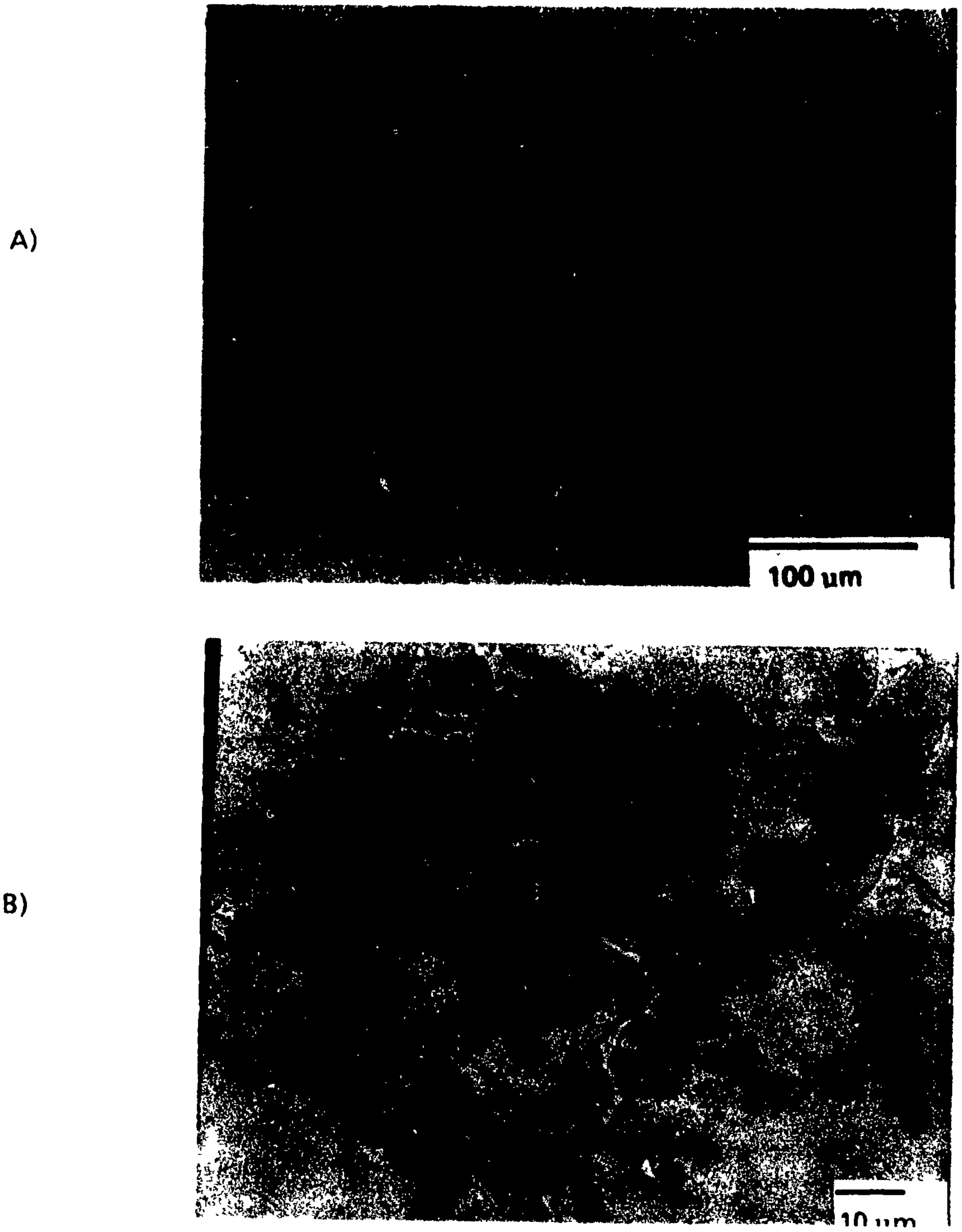

Fig. 10: Microstructure of AZ91 at two different magnifications, showing the primary Mg, Al rich eutectic and the round Mn-Al compounds that also incorporate much of the iron in the alloy. At higher magnification, the grey compound phase within the eutectic is $Mg_{17}Al_{12}$.

to Fig. 11, to the large drop in Fe impurity content in the settled alloy, most of these particles could be the Iron - manganese containing intermetallics.

Figures 10A and B show the microstructure of this alloy at 250 and 1000x magnification. It consists of primary magnesium, an aluminum rich eutectic, and an either fibrous or spherical phase enriched in Al, Zn, Fe and Mn This intermetallic phase forms during solidification and contains most of the remaining iron in molten magnesium

3.3 Effect of Particle Settling from the Melt on the Physical Properties of Magnesium Alloys

Table 6 shows the mechanical and corrosion test results, and the impurity levels in alloys ZE41 and AZ91 after stirring, and after settling for a period of 40 minutes Mechanical tests were made according to ASTM B557, using standard round test bars (0.5" dia., 2" gauge length). Corrosion (salt spray) tests were made according to ASTM B117, on the as cast and heat treated, $1\frac{1}{2}$" dia , disc samples Figure 11 displays the test results $\bar{x}$, and a 95% confidence interval for the actual (population) mean value μ in the form of bars for visual comparison As seen, no significant difference can be observed in the mechanical properties of either alloy after a settling treatment. A reduction in corrosion rate was noticable only in ZE41 alloy samples, a group comparison test in Table 7 shows that a significant improvement (>95% confidence) was observed in the tempered ZE41 samples only in view of the limited amount of data obtained, these findings must be regarded preliminary.

After settling, both alloys show reductions in those impurities contents that are known to be harmful for corrosion, indicating that the settled particles must have been richer in these elements than the melt itself In spite of a significant drop in nickel content, and a reduced particle population in the melt, curiously, no improvement was observed in the corrosion rating of AZ91 alloy The large drop in iron content, however, was not expected to reduce corrosion rate significantly, because the Fe/Mn ratio was already below the critical 0 032 in this alloy [6]

Table 6 Changes in physical properties of the magnesium alloys after stirring and settling

Physical Property(1)		ZE41		AZ91	
		I(2)	II(2)	I(2)	II(2)
Ultimate Tensile Strength, MPa		214.2 8.42 (4)	213.7 18.77 (4)	278.6 10.2 (4)	269.0 15.2 (4)
Yield Strength, MPa		162.9 2.05 (4)	156.1 8.02 (4)	141.5 3.99 (4)	141.8 10.2 (4)
Elongation, %		2.83 1.21 (4)	3.35 1.05 (4)	4.91 0.63 (4)	4.44 1.21 (4)
Corrosion Rate, as cast(3), mm/year		6.58 2.36 (3)	4.52 0.33 (3)	2.01 0.51 (3)	1.35 0.61 (3)
Corrosion Rate, heat-treated(4), mm/year		17.07 2.90 (3)	11.58 1.14 (3)	2.21 1.52 (3)	2.26 0.76 (3)
Chemical Composition	% Al	-	-	8.5	8.5
	Mn	-	-	0.25	0.26
	Zn	3.9	4.1	0.76	0.76
	R.E.	1.4	1.4	-	-
	Zr	0.5	0.4	-	-
	ppm Fe	30	21	54	23
	Ni	25	22	27	20
	Cu	33	30	17	14

(1) Data in boxes refer to the mean value $\bar{x}$, standard deviation s, and the number of tests (*n*).

(2) Condition I is after puddling for ZE41, and after grain refiner additions and degassing for AZ91, condition II is after settling for a period of 40 minutes for both alloys

(3) 1½" dia discs cut from chill cast cylindrical blocks

(4) Samples were heat treated (tempered) as follows:
ZE41, T5: 2 hours at 330°C followed by 16 hours at 175°C,
AZ91, T6. 18 hours at 410°C followed by 16 hours at 170°C

Table 7. Comparison of corrosion rates of samples taken from stirred and settled melts(1).

Alloy	$\bar{x}_I$ $\bar{x}_{II}$	s_I s_{II}	n_I n_{II}	t or t' value(3)	v v'	$t_{0\,05,v}$ $t_{0\,05,v'}$	% conf (4)
ZE41(2)	6.58	2.36	3	1.50	4	2.132	
	4.52	0.33	3		2.08	2.846	
	17.07	2.90	3	3.05	4	2 132	
	11.58	1.14	3		2 60	2.509	96 7
AZ91(2)	2.01	0.51	3	1.44	4	2 132	
	1.35	0.61	3		3.88	2.151	
	2.21	1.52	3	-0.05	4	2 132	
	2.26	0.76	3		2.94		

(1) H_0: $\mu_I \le \mu_{II}$ is tested against H_a: $\mu_I > \mu_{II}$ Alternative hypothesis is accepted with a greater confidence than 95%, if computed value of $t > t_{0\,05,v}$

(2) In each alloy, the first two rows of data refer to as cast, and the last two rows of data refer to heat treated, samples Subscripts I and II, refer to stirred and settled melts

(3) t values for group comparison t-test If $\sigma_1 = \sigma_2$ may be assumed, t and v values, if not, for a more conservative test, Behrens-Fisher t' and v' values are used [13]

(4) Actual % confidence in accepting H_a, computed if confidence level >95%

4 DISCUSSION OF RESULTS AND CONCLUSIONS

No improvement was observed in the mechanical properties of either alloy studied that would be attributed to the settling out of particles In the plant, the alloys were prepared by a fluxless procedure, using a CO_2, 0.6% SF_6 protective atmosphere. Consequently, the settling particles were mostly intermetallics, and because of their better interfacial properties, intermetallic particles would be expected to provide greater resistance to void formation than, say, flux inclusions Of all mechanical properties, fatigue strength is particularly sensitive to the nature, size, and population of particles, but this test was not available for the present work Therefore, for alloys produced under halide flux protection, LiMCA measurements may provide a significant correlation with mechanical properties, especially with regards to fatigue strength, but this requires further research.

Corrosion ratings for both alloys were within the expected ranges. A figure of 12 mm/year was reported for ZE41 by Clark [7]. For AZ91C alloy, ratings vary between

15-30 mm/year: this has been reduced to less than 0.4 mm/year for the recently developed extra-pure alloy, AZ91E-T6 [6,7] Normally, an improvement would have been expected in the heat-treated alloys, but this was not observed in our samples The relationship between Fe, Ni, and Cu impurities and the magnesium alloys, especially for alloy AZ91, is well established [4-6] LiMCA, being a discriminating device, only measures the particle populations greater than a critical size Therefore, such measurements would be useful provided larger particles have a much greater affect on corrosion rate than smaller particles This appears to be the case for the ZE41 alloy, where small reductions in impurities in the same alloy lead to a significantly better corrosion rating. In the AZ91 alloy, settling lead to fewer large particles (>15 μm) in the melt, but no improvement in corrosion rating was observed in this alloy. This suggests that both "small" and larger particles promote corrosion in this alloy However, it is probable that the number of samples tested for corrosion were too few (only 3 per alloy) to draw statistically significant conclusions. More samples for corrosion testing could provide greater certainty in establishing any correlation between LiMCA measurements and the corrosion resistance of magnesium alloys

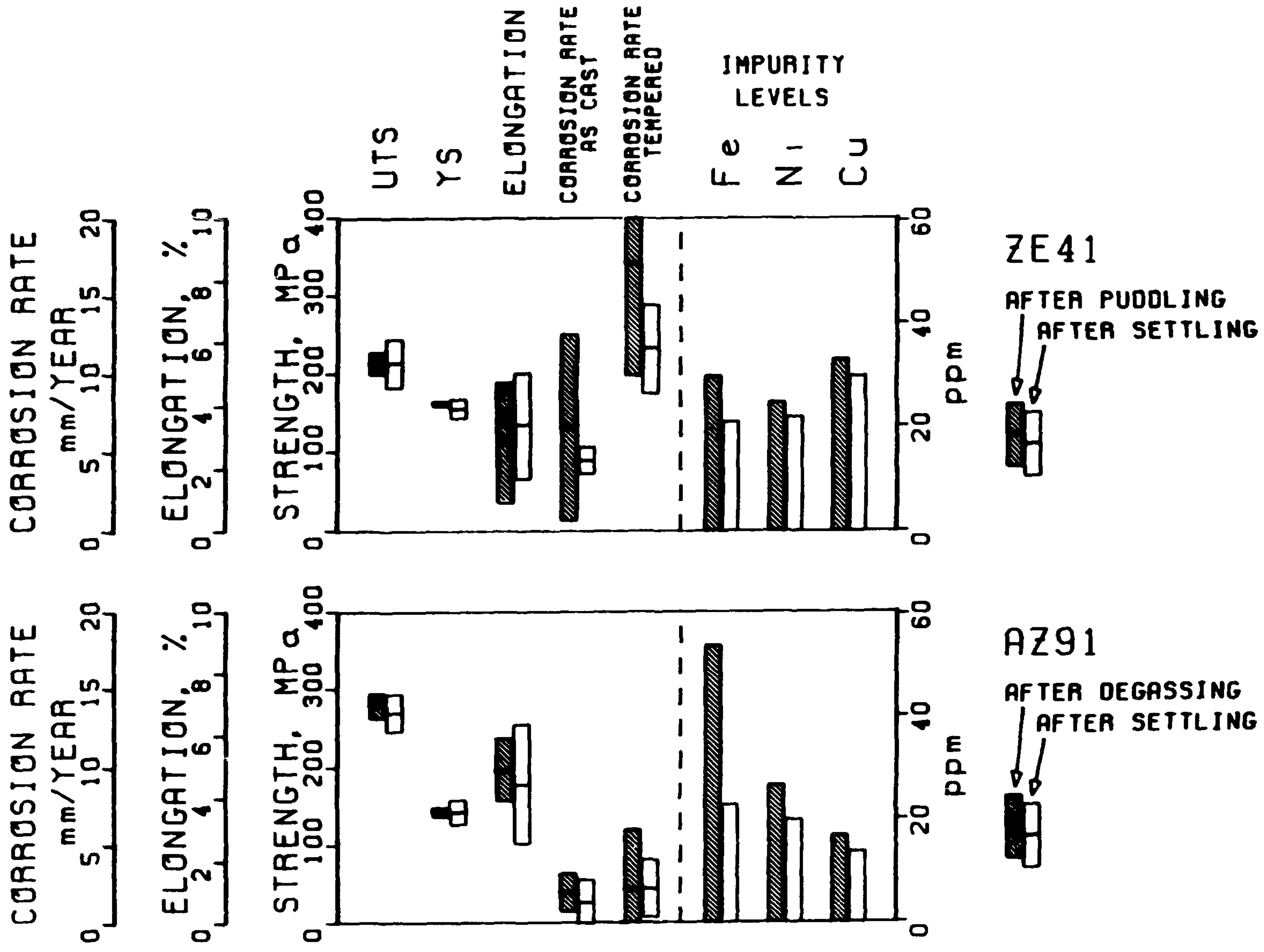

Fig. 11 Changes in the physical properties and impurity levels of ZE41 and AZ91 alloys after stirring and after a 40 minute period of settling Bars show the mean values ($\bar{x}$) and the spread of data (± 2s)

REFERENCES

1. B B Clow, "Magnesium supply and demand", in *Magnesium, a Strategic Material*, Proceedings of the 45th Ann World Magnesium Conf , pp 50-54, Int. Magnesium Assoc , Washington, D.C., 1-4 May 1988

2 E F Emley, in *Principles of Magnesium Technology*, pp 115, 391-396, Pergamon Press, New York, 1986

3 E F. Emley, in *Principles of Magnesium Technology*, pp. 670-685, Pergamon Press, New York, 1986

4. J.D. Hannawalt, C.E Nelson, and J.A. Peloubet, "Corrosion studies of magnesium and its alloys", *Trans. AIME*, **147**, 1942, pp 273 299

5 J E. Hillis, "The effects of heavy metal contamination on magnesium corrosion performance", *SAE*, Paper No.830523, 1983, pp 2 553-2 559

6 J.E Hillis, K.J. Clark, and K.N. Reichek, "Controlling the salt water corrosion performance of magnesium AZ91 alloy", *SAE*, Paper No 850417, 1985, pp. 3 318-3 329

7. K J Clark, "AZ91E magnesium sand casting alloy: the standard for excellent corrosion performance" Proceedings of the 43rd Ann World Magnesium Conf., pp 37-41, Int. Magnesium Assoc.,15-18 June 1986

8. D.M Magers and H.J. Morales, "High purity magnesium die casting alloy", *Die Casting Engineer*, **28**, (1), 1984, pp. 18-20.

9 C.S Roberts, in *Magnesium and its Alloys*, pp. 195, John Wiley, New York, 1960

10 R W, DeBlois and C.P. Bean, "Counting and sizing of submicron particles by the resistive pulse technique", *The Review of Scientific Instruments*, **41**, (7), 1970, pp. 905-915.

11. D.A. Doutre and R.I.L Guthrie, "On line measurement of inclusions in liquid metals", *Int. Symp. on Refining and Alloying of Liquid Aluminum and Feroalloys*, Engh, Lyngh and Oye (Eds), pp. 147-163, Trondheim, Norway, 26-28 August 1985.

12. Product Catalogue, Harbison-Walker Refractories, Division of Dresser Ind., Inc., One Gateway Center, Pittsburgh, Pennsylvania, 1986.

13. P S. Dowdy and S. Weardon, in *Statistics for Research*, Wiley, 1983

List of Figures

List of Tables

PART 5: CONCLUSIONS TO THE THESIS

1. SUMMARY OF FINDINGS

The following sections summarize the experience gained in constructing LiMCA probes, and taking LiMCA measurements in high temperature and reactive metals

1.1 Steel Melts

1. Among a number of refractory conductors, graphite was found to be a reliable material for electrode construction. Freely dissolving electrodes did not interfere with the detection of microvolt signals, but chemical reactions between electrodes and steel melts producing non-conducting products did Examples are molybdenum in sulfur rich, and graphite in oxygen rich steel melts

2. A water cooled steel electrode, for use as outside electrode in high temperature steel melts, was designed. Its design criteria was to keep melt / electrode contact at all times without creating a massive solidified steel shell around the electrode.

3. Sampling tubes: Boron nitride was found to be an acceptable, albeit expensive, sampling tube for steel melts of low oxygen potential (less than 15 ppm $\underline{O}$). Porous refractory silica, such as Masrock™ (Harbison-Walker) could also serve as sampling tubes over a much wider range oxygen levels with acceptable machinability to place inserts. Silica glass sampling tubes can be used up to 1500°C without deformation and was surprisingly found to resist fluxing by boron, silicon steels. Above this temperature they need to be supported by a refractory material against deformation.

4. Orifice geometry: Experiments with boron, silicon steels showed that the most stable operations occurred with circular orifices with fluted inlets and outlets Intuitively, these would be expected to provide the least obstacle to fluid and electric flows. However, as long as sharp corners were avoided, the effect of orifice geometry was found to be of secondary importance.

5 Experiments with other steel melts and cast irons showed orifice - molten metal - inclusion interactions to be very important for the smooth operation of LiMCA.

6 For a given melt and set of conditions, orifice size needs to be adjusted to acquire a significant number of inclusions, but should not be too small to cause its blockage. For boron, silicon steels, the optimum size of orifice was found to be 150 - 200 µm, and 400 - 500 µm following an aluminum addition

1 2 Copper Melts

1. The control of oxygen content in unalloyed copper was found to be of paramount importance to prevent oxidation of electrodes. Among the electrode materials tested, nickel was selected as this was the least susceptible to oxidation, and was available at a reasonable cost.

2 Oxygen pick up from the atmosphere was best prevented by placing a lumpy charcoal layer on the melt surface rather than graphite powder. It was found that graphite powder would creep down the crucible wall, and accumulate at the bottom of the crucible. Some graphite powder was also found to creep down outside the sampling tube wall and interfere with the operation of the sensing zone. Interfacial turbulance, as well as convective currents during heating and cooling cycle of the furnace could be factors causing this downward movement of (light) graphite powder down the crucible / copper interface to the bottom.

3 The same silica glass sampling tube / sensing zone arrangement used for boron, silicon steels was also used for copper melts.

4. LiMCA measurements in copper beryllium alloys with 2% Be produced agreeable results with an independent metallographic count, whereas alloy 3, containing lower beryllium, attacked the silica glass tubes. For measurements of BeO particulate content in the higher Be alloys, a 300 - 400 µm orifice was found to be an optimum size.

1.3 Magnesium Melts

1. Sampling Tubes: Although magnesium would be expected to attack silicates (and this was the case with silica, borosilicate and aluminum silicate glass), penetration into porous, opaque silica (Masrock™) was minimal. Sampling tubes with 5 mm wall thicknesses made from porous silica were used Their immersion into magnesium melts produced a scale around the sampling tube wall, and reduction in wall thickness under the scale was less than 1.5 mm for two hours of immersion

2. Since magnesium attacked most oxides, the orifice was formed in a boron nitride insert to be fixed on a sampling tube Dimensional stability of these orifices was good.

3. LiMCA measurements in magnesium alloys ZE41 and AZ91 gave indications of the particulate content of these metals. However, correlations of LiMCA counts with alloy properties were poor.

2. GENERAL DISCUSSION AND RECOMMENDATIONS FOR FUTURE WORK

LiMCA's operation as a measuring device in high temperature and reactive metals has been shown to be possible. The experimental procedure outlined in Sections 3.5.1 and 3 5 2 of Part 1 helped to identify the sources of electronic noise and baseline instabilities during probe development In all cases, it was possible to rectify electronic noise problems caused by electrode / molten metal contacts, circuit components and environmental induction On the other hand, noise caused by orifice deterioration was found to be of a more fundamental nature.

Highly successful results with boron - silicon transformer steel versus poor results with steels of other composition indicate that it was not the molten iron per se that caused the difficulties, but rather what it contained Suspended particles (inclusions), molten metal and orifice wall interaction were hypothesized to be the cause of orifice deterioration It is believed that orifice deterioration is caused by inclusions accumulating at the sensing zone region by way of physical attachment, and thereby interfering with the electric and fluid flows Ideally, therefore, inclusions should be wet by molten metal, or have low interfacial energy, and not "wet" the orifice wall. Experimental evidence supporting this hypothesis is the ease of LiMCA's operation in aluminum and magnesium melts to count intermetallic particles. Because of their structural similarity, intermetallic particle / metal contact angles would be expected to be low. From Table 13, Part 2, for instance, molten aluminum in contact with TiB_2 has a contact angle of 98°. Similarly, from Table 14, Part 2, additions of boron oxide will reduce the surface tension of silica, and this must have helped the smooth operation of LiMCA in boron, silicon steels, in counting borosilicate inclusions.

In the light of the above discussion, recommendations for further resarch would be to acquire interfacial data that will help in the selection of materials for LiMCA's sensing zone region, and into these selected materials, form fluted, circular orifices with highly polished surfaces, for use as sensing zones in given molten metal / inclusion systems.

2. CLAIMS FOR ORIGINAL CONTRIBUTIONS

1. LiMCA's electric circuit was analysed to show the effect of ballast resistance on the magnitude of voltage pulses. It was shown that voltage pulses could also be detected across the ballast resistance, and their magnitudes were shown to be equal in value, but opposite in sign to those detected across the electrodes The value of ballast resistance was optimized for a given e.m f and LiMCA probe, in order to obtain maximum pulse heights Its value was shown to be equal to the resistance across the electrodes. The effect of a finite electric conductance of a sampling tube on the voltage pulses measured was determined

2. A novel LiMCA probe was developed for low melting point steels and cast irons. This work represents the first time meaningful LiMCA measurements were ever made for molten steels (specifically an electric grade steel containing 5% B, 3% Si, used in the manufacture of transformer cores). A systematic investigation of cast irons and steels showed that reliable operation of LiMCA in iron alloys was highly dependent on their chemical composition, which in turn determines the chemistry and the nature of contained indigeneous inclusions, and the interface properties between inclusion, melt, and the orifice wall It was shown that unstable operation of LiMCA in other iron alloys was caused by the orifice (sensing zone) deterioration

3. A water cooled permanent electrode was designed for use as an outside electrode in steels and higher temperature m p. metals. It was shown to be reliable in keeping a low background electronic noise while conducting a high D C. current into the melt.

4. A novel LiMCA probe was designed for copper melts and was successfully used in the technologically important Cu-Be alloys to monitor the levels of BeO inclusions

5. A novel LiMCA probe of reasonable cost, incorporating a machinable ceramic sampling tube was designed for magnesium melts and was used to monitor the particulate contents of ZE41 and AZ91 alloys